NASA Contractor Report 165497

MICROSTRUCTURAL EFFECTS ON THE ROOM AND ELEVATED TEMPERATURE LOW CYCLE FATIGUE BEHAVIOR OF WASPALOY

Bradley A. Lerch

University of Cincinnati
Cincinnati, Ohio

May 1982

Prepared for

NATIONAL AERONAUTICS AND SPACE ADMINISTRATION
Lewis Research Center
Under Grant NSG 3-263

TABLE OF CONTENTS

LIST OF SYMBOLS

a	Lattice Translation Vector
b	Burger's Vector
β	Coffin-Manson Exponent
d	Distance Between Precipitates
d_0	Grain Diameter
d_p	Average Dislocation Pair Spacing
da/dN	Crack Growth Rate
E	Elastic Modulus
ε	Strain
$\Delta\varepsilon_p$	Plastic Strain Range
$\Delta\varepsilon_p{}^l$	Longitudinal Plastic Strain Range
$\Delta\varepsilon_p{}^d$	Diametral Plastic Strain Range
$\Delta\varepsilon_e$	Elastic Strain Range
$\Delta\varepsilon_t$	Total Strain Range
f	Precipitate Volume Fraction
G	Shear Modulus
ΔG	Change In Free Energy
ΔG_v	Change In Volume Free Energy
ΔG_{r_c}	Change of Free Energy For Formation of a Nucleus of Size r_c
ΔG_{r_0}	Change of Free Energy for Formation of a Nucleus of Size r_o

LIST OF SYMBOLS (Con't)

g	Reflecting Vector
γ	Austenitic Matrix Gamma
γ'	Precipitate Gamma Prime
γ_o	Specific APB Energy
γ_E	Surface Energy
γ_{APB}	APB Energy
i	Slip Band Spacing
ΔK	Stress Intensity
M	Mole
N	Cycles
N_i	Cycles to Initiation
N_f	Cycles to Failure
n'	Cyclic Stress-Strain Exponent
Q	Experimental Activation Energy
R_p^f	Fatigue Plastic Zone Diameter
r	Precipitate Radius
r_c	Critical Nucleus Radius
r_0	Radius of a Cottrell Atmosphere
S.F.	Schmid Factor
σ_c	Compressive Stress
σ_{max}	Maximum Fatigue Tensile Stress
σ_R	Stress Range
σ_T	Tensile Stress

LIST OF SYMBOLS (Con't)

σ_{ys}	Yield Strength
ϕ	Dislocation Line Tension
T	Temperature
t_f	Time to Failure
τ	Shear Stress
τ_m	Flow Stress of Matrix
τ_p	Flow Stress of Precipitate
ΔW	Work Per Cycle
{ }	Indices for a Family of Planes
( )	Indices for a Particular Plane
< >	Indices for a Family of Directions
[ ]	Indices for a Particular Direction

I INTRODUCTION

The field of low cycle fatigue (LCF) has been the subject of numerous research programs in recent years due to the demands of more stringent designs. The aircraft, automotive and power generating industries required going to higher cycle temperature and material stress levels to increase their fuel efficiency. Thermal cycling and natural vibrations create a serious fatigue problem. Increased fatigue resistance of materials is needed without sacrificing other properties.

A family of superalloys was developed for high temperature, high strength applications. Initial developments had the goal of increasing the strength. The effect of microstructure on fatigue behavior was not appreciated and consequently the alloys were not designed or heat treated for maximum fatigue resistance. The effects of microstructure are now understood and improved fatigue resistance is possible and indeed mandatory.

The nickel base alloy, Waspaloy, was selected for this study due to its wide usage in aircraft engines. The primary goal of this research program was to examine various microstructures of Waspaloy and their effects on the fatigue behavior. Drastic differences in the microstructure could be made without changing the tensile strengths. This eliminates any strength effects on the fatigue behavior.

Heat treatments to produce microstructural differences were chosen by Lawless[1] for his study of microstructural

effects on FCP properties as part of a larger overall study on Waspaloy. Varying grain size and precipitate sizes resulted in different slip modes and different rates of fatigue crack propagation (FCP). Since all other microstructural aspects were kept relatively constant, damage mechanisms could be easily studied for both LCF and FCP tests.

It was suggested that the LCF process is related to the FCP process.[2] This relationship can be examined by comparing the damage mechanisms of LCF and FCP specimens at equivalent strain ranges. If they are similar then some mathematical model can be derived to relate the two. Surely this is of great interest since LCF tests are easier and more economical to perform. Providing an experimental base for such modeling was one goal of this project.

Since Waspaloy is normally used at elevated temperatures, temperature effects were also considered. The flow stress of Waspaloy remains relatively independent of temperature up to about 800°C.[3] Once again, this variable of strength can be neglected. With increasing temperature, there is an increased tendency for homogeneous slip, oxidation, phase instabilities, creep, and combinations of these and other mechanisms. Clearly, fatigue damage becomes extremely complex at these temperatures. Oxidation can seriously embrittle the alloy resulting in premature failure. Very little is understood of oxidation under complex load

cycling. A further goal of this study is to provide information in these areas.

As the damage mechanisms become better understood, microstructure can be adjusted to optimize the properties. The ultimate result should be a new generation of fatigue resistant alloys. While alloy development was not a specific goal of this study, the major objective of this project was to provide information upon which meaningful alloy development programs could be based.

II BACKGROUND AND LITERATURE REVIEW

A review of the literature indicates an abundance of information on the fatigue response of various metals and alloys. The main thrust of most experiments is to develop design data and, in some cases, correlation of mechanical properties with fatigue behavior. Microstructure and temperature are considered less frequently. The influence of oxidation is practically neglected. Yet, all of these are important in assessment of damage mechanisms which must be thoroughly examined in order to fully understand fatigue.

To best provide a basis for this study, this survey was divided into four sections: A) Physical metallurgy B) Room temperature low cycle fatigue C) Fatigue crack propagation and D) High temperature low cycle fatigue and oxidation.

A) PHYSICAL METALLURGY

Waspaloy is a heat treatable superalloy. The general structure of Waspaloy consists of a Ni austenitic matrix (γ matrix), solid solutioned strengthened with Co, Cr, and Mo. The high melting points of Ni and Co provide the basis for good mechanical properties at elevated temperatures. Cr and Al form protective, adherent oxides which increase the oxidation resistance.

Like many of the superalloys, Waspaloy is strengthened by a gamma prime (γ') precipitate. This precipitate is an ordered, $L1_2$ phase with a general composition of $Ni_3(Al,Ti)$.[4]

The ordering provides antiphase boundary (APB) strengthening. In addition, other strengthening mechanisms associated with precipitate hardened materials such as precipitate-matrix mismatch, Orowan looping, strength differences between precipitate and the matrix also apply.

The carbides are usually of the MC and $M_{23}C_6$ type where the "M" elements are Cr, Ti and Mo. MC carbides are usually of large blocky morphology and distributed throughout the matrix. The $M_{23}C_6$ carbides are distributed along the grain boundaries. The carbides improve the creep resistance by restricting grain boundary sliding. However, if there is a continuous grain boundary film, the embrittled boundary could also result in early failure. Thus, the carbides have a decidedly double character.

Heat treatments determine the phases present and the corresponding material properties. For example, Rehrer[5] et al. found that solution treating Waspaloy in the temperature range 1950-1975°F (1066-1079°C) results in large grains which have good creep properties. This may be suitable for turbine bolt applications where resistance to relaxation and creep is needed. However, this heat treatment resulted in reduced low temperature tensile strengths. This is not desired for turbine discs. Here, the temperatures are relatively low and creep is less of a problem. However, high hoop or tensile stresses are encountered. The proper heat treatment and resulting microstructure is clearly determined by the intended application.

Precipitation of intermetallic phases sometimes occurs in superalloys. These so-called TCP (Topologically Close-Packed) phases are generally detrimental to properties and therefore are controlled carefully. The three of most interest are Mu, Laves, and Sigma. These phases have complex structures containing as many as 30 atoms per unit cell.[6] They contain high amounts of refractory elements which are depleted from the matrix subsequently weakening it. These phases usually have a plate or needle-like morphology. These structures easily initiate cracking due to their sharp corners and inherent brittleness. The crack can easily propagate along the plate-matrix interface resulting in a loss of ductility. A computerized process called PHACOMP was developed to adjust compositions during alloy development in order to prevent TCP (especially σ) formation.[7]

Waspaloy is generally not subject to the formation of TCP phases. However, it is conceivable that under extreme cases of chemical segregation some might form. No evidence of these phases was observed during this study nor during the review of literature on Waspaloy.

B) ROOM TEMPERATURE LOW CYCLE FATIGUE

As previously mentioned, most superalloys contain precipitates which strengthen the alloy by hindering dislocation motion. In a similar system, Luetjering and Weissmann[8] studies the tensile properties of Ti/Al alloys. The Al composition was varied to provide various sizes and interparticle distances of the coherent ordered precipitate, Ti_3Al. It was observed that the yield strength increased with increasing precipitate size up to a maximum. From this point, the strength decreased with increasing particle diameter. Mitchell[9] found similar results in his stuides on Ni base alloys. He found that the same hardness could be achieved with either small or large diameter precipitates. This behavior is typical for age-hardenable materials. Both Luetjering[8] et al. and Mitchell[9] observed dislocations shearing the small precipitates. As the precipitate size increased, the dislocations met increased resistance to their movement, resulting in a strength increase. Such increases are predicted by the theoretical works of Gleiter and Hornbogen[10], Ham and Brown[11] and Copley and Kear.[12] Gleiter and Hornbogen suggested that:

$$\tau = r^{1/2} S\gamma^{3/2} f^{1/2} / G^{1/2} b^{2} \qquad \text{.....(1)}$$

where τ = shear stress

S = material constant

γ = specific APB energy (ergs/cm^2)

f = precipitate volume fraction

r = precipitate radius

G = shear modulus

b = magnitude of the Burgers vector.

Ham and Brown[11] suggested that:

$$\tau = \tau_o + \frac{\gamma_o}{2b}\left(\frac{4\gamma_{orf}}{\pi\phi}\right)^{1/2} - f \qquad \text{.....(2)}$$

where the symbols have their previous meanings.

Copley and Kear[12] suggested that:

$$\tau = \gamma_o/2b - \phi/br + \frac{K}{2} - (\tau_m + \tau_\rho) \qquad \text{.....(3)}$$

where ϕ = line tension of the dislocation

K = material constant & dependent on the dislocation velocity

τ_m, τ_p = flow stress of the matrix and the precipitate respectively and all other symbols retain their previous meanings. All of these forumlae indicate increasing shear strength with increasing particle radius. However, at some critical size, the dislocations find it favorable to loop precipitates. The strength drops since the precipitates no longer restrict their motion.

Orowan[13] showed that for unpenetrable particles, τ decreased with increasing distance between the precipitates by the equation:

$$\tau = 2Ga/d \qquad \text{.....(4)}$$

where a = lattice translation distance

d = distance between precipitates

and the other symbols have their usual meaning. For a

constant volume fraction, as the radii increase, d increases and thus the shear stress decreases.

Similar results were found by Calabrese and Laird[14] in the fatigue of Al-4%Cu alloys. They related the fatigue response to deformation mechanisms. Alloys containing small precipitates (ie. the ordered, tetragonal θ'' phase c/a $\sim$ 2.0)[15] exhibited hardening to a maximum stress followed by softening to failure. This was represented in the cumulative glide (ie. stress vs. cycles) plot. Increasing the plastic strain range increased the maximum stress and decreased the cycle at which the maximum occurred. Planar slip was shown to be the operative deformation mechanism. The exact dislocation-precipitate interaction could not be examined due to the fineness of the θ'' .

The hardening, up to the maximum, was explained as restricted dislocation motion by the stress fields of other dislocations. In other words, the increase in dislocation density produced stress fields which had to be overcome for further plasticity. Cyclic softening resulted from shearing of the θ'' . The authors suggested that the dislocations pass more freely through this disordered structure. Such a suggestion has also been made by Pineau[16] et al.

No evidence is available to substantiate this theory at least for Al alloys. It is reasonable to assume that the precipitate is less ordered after testing than before due to the to and fro cutting motion of the dislocations. The degree of ordering and it's effect on properties is not well established.

Alloys containing large precipitates (ie. the ordered tetragonal θ' phase, c/a 1.44[15]) exhibited hardening to saturation.[17] Increasing the plastic strain range increased the saturation stress. In contrast to the small precipitate alloy, the number of cycles to saturation increased with increasing strain range. Saturation resulted from the development of a cellular substructure and the formation of interfacial dislocations on the precipitates.

Another variable to consider in the deformation process is grain size. Sanders and Starke[18] studied the effects of grain refinement on the fatigue behavior of Al-Zn-Mg alloys. Zirconium was added in some cases as a grain refiner. Tensile tests revealed increasing ductility with decreasing grain size. This was attributed to the formation of a more homogeneous slip in the fine grains. Slip bands in the coarser grains created stress concentrations at grain boundaries resulting in boundary cracking. The fracture surface was intergranular compared to the fine grained material. These results are similar to those found by Luetjering[7] et al. in their work in Ti/Al alloys.

At high strain amplitudes, the Al-Zn-Mg-Zr alloy had superior fatigue resistance compared to the ternary Al-Zn-MG alloy. This was found to be a result of a more homogeneous slip for the fine grained material. Again, the coarse grained ternary alloy had boundary stress concentrations from planar slip and early crack initiation was suggested. Though apparently reasonable, initiation measurements were performed

only on the fine grained material. The procedure for measuring initiation was not presented and the explanation of early crack initiation is questionable.

Another mode of deformation may be microtwinning. Fournier and Pineau[19] investigated the fatigue behavior of In-718 at room and elevated temperatures. In-718 is a superalloy strengthened primarily by a gamma double-prime (γ'') precipitate. This coherent precipitate is a bct disc-shaped particle of DO_{22} type structure. The cumulative glide response showed hardening and softening characteristics as discussed before for shearable precipitate materials. TEM micrographs indicated precipitate shearing by dislocations. Planar slip was the operating mechanism. However, as the plastic strain amplitude increased, deformation occurred by twinning. Twins and slip bands initiated fatigue cracks by a Stage I mechanism.

The softening of the alloy was explained by the shearing of the γ''. The authors suggested that upon shearing the "mean area for dislocation penetration" is reduced and hence the hardening phenomena is decreased. Eventually, there will be almost no precipitate in an active slip plane to restrict dislocation motion. This is a more reasonable theory than the disordering phenomena suggested by Calabrese and Laird[17] or by the dissolution theory[20] which will be discussed later.

Fournier and Pineau[19] defined fatigue crack initiation as the development of a crack 50-100μ in length. This crack length represents the approximate length of Stage I cracks

which resulted in eventual failure. The fraction of total life spent in initiation was determined to be 70%. The effect of plastic strain range on initiation was not investigated.

Stoltz and Pineau[16] investigated the effects of γ' size on the LCF behavior of Waspaloy. Specimens had equivalent grain sizes (ASTM 5 or 60 μ diameter) but contained varying γ' sizes. The two extreme sizes were 80Å and 900Å diameters. It was found that cumulative glide behaviors were similar to those discussed previously. The 900Å material hardened to saturation, where the 80Å material hardened to a maximum and then softened. The number of cycles to the maximum remained constant (about 20-30 cycles) regardless of the plastic strain imposed. This differs from the response of Calabrese and Laird's[14] Al-4%Cu for which the maximum occurred at earlier cycles with increasing strain amplitude.

It was shown that in the 80Å material, dislocation motion was restricted to discrete bands. The density of these bands increased linearly with increasing plastic strain range. Diederich[21] and Clavel[22] et al. found an exponential type dependence. Stoltz and Pineau's study existed only over a small range of values and appeared as an asymptote on the exponential data. Dislocations in the bands were observed to shear the precipitates resulting in softening. The 900Å material showed dislocation bowing between the precipitates. When the grains were completely filled with dislocations (ie., dislocations were not restricted to bands but produced a

3-dimensional network), saturation occurred.

Merrick[20] studied the fatigue behavior of In-718, In-901, and Waspaloy. The grain sizes were varied to determine their effect on the cracking mode. It was found that a decrease in grain size increased the fatigue life.

Planar slip and precipitate shearing were observed in all cases. TEM darkfield micrographs show dark bands caused by slip. Merrick suggested the "apparent absence of γ' precipitates in these bands indicates dissolution of the γ' precipitates." Dissolution of these particles is highly unlikely from a thermodynamic viewpoint. The γ' is extremely stable up to very high temperatures. It is unreasonable to assume that mere cutting of them by dislocations would supply enough energy for dissolution. Instead, the "absence" was probably due to diffraction effects from local lattice distortions or disordering. This would have to be confirmed by extensive tilting experiments. Cracking was found to initiate by a Stage I mechanism. Cracking proceeded transgranularly with occasional deviations along grain boundaries. No mention was made of any influence of grain size, if any, on the crack path.

It is clear that attempts to explain fatigue behavior are often made without an adequate understanding of the microstructure. Full microstructural examination must be performed to determine what is actually occurring during fatigue.

C) FATIGUE CRACK PROPAGATION

A crack has basically two distanct phases: an initiation stage which was discussed previously, and a propagation stage which is considered at this point. Since materials contain defects, this propagation stage becomes critical to the life of the component. These defects can act as cracks or as crack starters which then propagate to failure. The life can usually be predicted provided that experiments which measure and correlate crack growth rate to a meaningful parameter are performed. Numerous engineering studies have been done in this manner. However, the metallurgical effects on crack propagation have only recently been investigated. Microstructure can play a significant role in the rate of crack growth. Some of the more recent theories will be discussed at this point.

Saxena and Antolovich[2] studied the effects of stacking fault energy (SFE) on fatigue properties of Cu-Al alloys. It was found that by decreasing the SFE, the deformation became more inhomogeneous (ie. promoted planar slip) and increased the fatigue crack growth resistance. No explanation of the reduced growth rates of planar slip materials was given. This should be an area for further investigation.

The authors observed damage similarities between the plastic zone ahead of the fatigue crack and those observed in LCF specimens at equivalent strain ranges. It was suggested therefore that FCP can be viewed as a series of LCF processes ahead of the crack. An equation for estimating FCP rates

based upon monotonic, LCF, and microstructural parameters was tested and found to yield a reasonable correlation. Since LCF and tensile experiments are easier to perform, than are FCP tests, further testing of this formula is greatly desired.

Although limited information is available, it was suggested in the previous section that planar slip promoted early initiation and perhaps failure in LCF specimens. Yet, planar slip was shown by Saxena and Antolovich[2] to be beneficial to crack growth resistance. Similar results were observed by Lawless[1] in his studies of microstructural effects on the FCP properties of Waspaloy. Several heat treatments were employed and FCP behavior was compared using the Paris[23] law:

$$\frac{da}{dN} = R(\Delta K)^m \qquad \text{.....(5)}$$

where $\frac{da}{dN}$ = crack growth rate

R,m = materials constants

ΔK = stress intensity

Lawless[1] observed that for a given grain size, small γ' precipitate materials gave superior crack growth resistance. Also, for a given γ' size, coarse grained materials showed superior crack growth resistance. The difference decreased with increasing growth rates (i.e. increasing ΔK). Although limited metallography was performed, it was believed that conditions causing superior crack growth resistance were associated with planar slip. This seems reasonable considering the earlier discussion of the propensity for planar slip by coarse grained and/or small precipitate materials.

Merrick and Floreen[24] investigated microstructural effects on fatique crack growth of Waspaloy and Astroloy at 650°C (1200°F). Three heat treatments were employed for each material resulting in various grain and/or γ' sizes and distributions. Tests were peformed at very high growth rates (eg. $da/dn = 10^{-4} - 10^{-3}$ cm/cycle). Microstructural effects on Waspaloy were negligible even though the materials had different precipitate sizes. The authors suggested that This may be due to the high growth rates employed in testing. Lawless[1] also indicated that microstructural effects diminished at high growth rates.

Astroloy showed an increase in crack growth resistance with increasing grain size. Again, at high growth rates the difference diminshes and the growth rates become equivalent. The heat treatments produced coarse grain material coupled with large γ' particles. These could have produced a combination of homogeneous and inhomogeneous slip. No TEM work was performed, hence the actual deformation mode is unknown.

This experiment showed little microstructural effects on FCP. However, differences in the microstructures were small. For instance, γ' sizes in Waspaloy were 160Å, 230Å, and a duplex structure of 160Å and 800Å. Limited microstructural differences coupled with high growth rates may have masked any differences in FCP properties.

An explanation for increased microstructural effects at low values of ΔK (low growth rates) was given by Bartos and

Antolovich[25] in their studies of P/M Rene'95. At low values of ΔK, the plastic zone ahead of the crack is small and about on the order of the microstructure. The plastic zone size in fatigue has been suggested by the equation:

$$R_p^f = c(\Delta K/\sigma_{ys})^2 \quad \text{.....(6)}$$

where R_p^f = size of the fatigue plastic zone

C = material constant

ΔK = stress intensity

σ_{ys} = yield strength of the material

Here it is observed that the plastic zone size decreases with decreasing ΔK. Hence, at low values of ΔK the plastic zone is more amenable to microstructural influence within a given grain.

D) HIGH TEMPERATURE FATIGUE AND OXIDATION

As temperature increases, the damage mechanisms become more complex. Phases become unstable,[26] cross-slip is more prominent,[27] oxidation rates increase[28] and at very high temperatures, creep phenomena become important, especially grain boundary sliding and cavitation of the boundaries which severly degrade the fatigue life. Furthermore, there may be interactive effects among the various phenomena. Many review papers have been written on high temperature fatigue mechanism to which the reader is referred.[26-29]

Grain boundary cracking is usually predominant at elevated temperatures. The effects of intergranular cracking are discussed in a study by Coffin.[30] Fatigue tests on A286 at

593°C (1100°F) showed superior lives when tested in a vacuum rather than in air. Metallographic examination showed air-tested specimens to have intergranular cracking with extensive oxidation. Vacuum tested specimens showed extensive slip and transgranular cracking.

Coffin attributed the reduced life in air to the change of crack propagation mode from transgranular (in vacuum) to intergranular (in air). Initiation was not studied, but could have also affected the lives. Another weakness of this study was the absence of substructure analysis. It was shown previously that the slip modes and precipitate-dislocation interactions have a profound influence on the fatigue behavior of a material, yet, this was not considered.

The importance of substructure is illustrated by Bashir[31] et al. in their study of hipped or hipped+forged Rene'95 at 649°C (1200°F). It was found that when planar slip occurred (ie low strain ranges) the life was increased compared to those specimens exhibiting a more homogeneous deformation. This was attributed to higher "average boundary stresses" of the homogeneous slip structure. Though planar slip materials have high stress concentrations at the boundaries and the slip bands, the chances of this band intersecting a brittle particle (i.e. boundary carbide or oxide) is small. Slip was transferred to the next grain and transgranular cracking was observed. The homogeneous structure strains the entire boundary and ruptured the brittle particles resulting in intergranular failure.

Dislocation-precipitate interactions at both 25°C (77°F) and 650°C (1200°F) were studied by Clavel[22] et al. LCF and FCP tests were performed on In-718 and Waspaloy. Waspaloy LCF specimens exhibited planar slip and precipitate shearing at 25°C. At 650°C the dislocations looped precipitates and slip was more homogeneous. Similar results were observed in the plastic zone of the FCP specimens. This indicates a similarity between LCF and FCP processes even at elevated temperatures as suggested by Saxena and Antolovich.[2]

Though it has been suggested that reduction of fatigue life might be due to environmental effects, little consideration has been given to oxidation. Yet, oxidation is probably a primary mechanism of failure in many materials.

Antolovich[32] et al. studied the LCF behavior of Rene'77 at 927°C (1700°F). Test specimens were severly oxidized especially at grain and twin boundaries. Two tests were run at room temperature. One of these was preoxidized, heat treated and then tested. This specimen had half the life of the non-oxidized specimen. This indicates the importance of oxidation on the fatigue life. The effect of oxidation during testing is probably even greater since in these studies the specimens were not oxidized under stress nor was oxidation occurring continually during the test.

The precipitate structure of Rene'77 coarsened significantly even after short test times. However, exposing specimens at 927°C for seven hours to simulate the longest test times had no significant effect on coarsening. It was thus concluded

that plastic deformation plays a significant role in the coarsening process and in fact a mechanism was suggested in this study wherein dislocations were seen linking large and small precipitates.

Similar results were found by Antolovich[33] et al. in their work on Rene'80 at 871°C (1600°F). Specimens were held at 982°C (1800°F) for 100 hours in stressed and unstressed conditions. Coarsening occurred in both cases. However, specimens in the stressed condition transformed cuboidal precipitates into plates. Reduced strength resulted from the coarsening process.

Additional studies[34] on the fatigue behavior of Rene'80 at 871°C (1600°F) showed similar γ' coarsening after testing. Dislocation analysis showed the development of interfacial edge dislocations on the coarsened precipitates. This structure was explained as reducing the strain energy of the matrix. It was not believed to be damaging. Instead, failure was suggested to occur by the development of grain boundary oxide spikes or oxygen penetration of the boundary. Metallographic evidence indicated these boundaries were the source of crack initiation.

A formula was developed which relates the oxide depth to the square root of the time to initiation. The development of this formula is not important at this time and interested readers are referred to this article. The important result here, is that an oxide spike or poisoned region grows to a critical size, at which point it behaves as a crack and

and causes failure. The dislocation structure, though it may assist oxidation, is not the primary damaging factor. Both oxidation and structural coarsening are being assisted by plastic deformation. The dislocations provide a "pipe" for diffusing species. These two mechanisms can therefore occur at temperatures lower than those predicted by a static test.

Prager and Sines[35] studied the oxygen embrittlement of Rene'41. They surmised that materials exhibiting planar slip are severely embrittled by oxygen. Their explanation was that planar slip resulted in dislocatipn pile-ups and stress concentrations at grain boundaries. As the boundaries absorbed oxygen, the surface energy was reduced and brittle fracture occurred. This occurred only if the slip was not transferred to another grain (i.e. this occurred only in high strength materials).

A formula was developed following the manner of Petch[36] - Stroh.[37] The fracture strain in tension was of the form:

$$\varepsilon = K^{1/2} d_o^{-1/2} \qquad \ldots\ldots\ldots (7)$$

where ε = fracture strain

K = group of constants including surface energy

d_o = grain diameter

This formula showed good correlation for planar slip Rene'41 at 800° and 900°C when in tension. Calculation of the surface energy through equation 7 showed it to be much less than that generally observed in nickel alloys. If the Petch-Stroh relation holds at room temperature, then it is reasonable to assume that it applies also at elevated

temperatures and has no relation to oxygen embrittlement. Therefore, this equation may not be valid approach.

Equation 7 is limited because it involves only tensile forces and failure occurs within seconds. Oxygen diffusion into the metal is certainly limited. Also, the cracking of the oxide or a small poisoned region is relatively unimportant. If the specimen was being cycled and if failure occurred hours later as in a fatigue test, this simple approach could no longer be used. In this case, oxidation rates become important.

The oxidation of the metal proceeds by one of two ways: a) direct reaction with fresh metal or, b) penetration of the diffusing specie(s) through an oxide layer to the metal. The second path depends on the properties of the oxide and the ease of transport through the layer. The situation is too complex to consider here. It may be generally unimportant since cycling produces oxide cracks or parent metal cracks which exposes fresh metal for oxidation.

Pilling and Bedworth[38] studied oxidation of various metals at high temperatures and concluded that the oxidation rate is dependent upon the volume difference between the oxide and the metal. If the oxide volume is less, the oxide will contain pores and a cellular layer is formed. This type offers no impedence to further oxidation. If the oxide volume is greater than the metal, a "compact type layer" is formed where expansion is limited by it's ductility. In fact, if the specimen undergoes compression, the oxide may

spall. If spalling does not occur the oxide severely limits the oxidation rate.

Since the oxides are intrinsically brittle, those metals exhibiting compact type layers are subject to cracking upon straining. These cracks then expose fresh metal for oxidation. Such a mechanism deteriorates the metal faster than diffusion of oxygen through an oxide layer. Romanoski[39] found this to be true in his work on Rene'80 fatigued at 1000°C (1832°F). The tests included compressive hold times in the fatigue cycles. These hold times were large compared to the ramp times and oxidation was assumed to occur during the hold period. Specimens showed oxide cracking throughout the gauge length. The crack spacing increased with decreasing total strain range up to a limit. The explanation was that the oxide forms in compression and as the specimen is subject to tension, the oxide cracks. As the total strain increased, the number of cracks increased. At some point, the number of existing cracks were sufficient to accommodate the strain in the oxide and prevent formation of additional cracks, thus a limit.

At low total strains, the crack spacing approached infinity (i.e. no cracks). At this point, the total strain was less than that needed to crack the oxide. The uncracked oxide acted as a protective coating. These specimens showed much greater lives than those of slightly higher strain which exhibited cracking.

In summary, at elevated temperatures the oxidation of metals becomes increasingly important. At intermediate temperatures, the rate of oxidation is low and occurs primarily at boundaries. This frequently causes intergranular failure. At higher temperatures, an oxide layer covers the surface and the resulting life may depend upon oxide properties and cycle character depending on the strain range.

To eliminate the deleterious effects of oxidation, directionally solidified and single crystal materials have been produced. Reduction or elimination of grain boundaries reduces oxidation effects. For instance, Duquette and Gell[40] indicated that at elevated temperatures, single crystals of MARM-200 showed equivalent or greater lives when tested in air then when tested in a vacuum.

It is clear that the effects of oxidation upon fatigue is practically neglected even though it may be the primary cause for failure in some cases. Studies of fatigue initiation which may account for premature failure are practically non-existant. It is hoped that this research program will enlighten these areas resulting in a better understanding of the microstructural effects on fatigue.

III EXPERIMENTAL PROCEDURE

A) MATERIALS AND HEAT TREATMENTS

A Waspaloy billet was supplied by Universal Cyclops Specialty Steel Division. Chemical composition of this billet (as supplied by them) is listed in Table I. The 12" X 12" X 1.25" billet was cross-rolled to minimize anisotropic effects.

Specimens were heat treated in air, in a resistance type furnace. All four heat treatments are given in Table II. Each heat treatment is letter coded for easy reference. These codes correspond to those used by Lawless.[1] Temperature was measured by a Chromel-Alumel thermocouple. Following solutioning and/or aging, specimens were rapidly quenched in a room temperature oil bath.

B) MECHANICAL TESTING

1) SPECIMEN CONFIGURATION

Figure 1 indicates the orientation of the FCP and LCF specimens as machined from the billet. The majority of LCF specimens were of solid longitudinal type as in Fig. 2. Four hour-glass specimens (Fig. 3) were used to study crack initiation. All specimens were low-stress ground to reduce machining effects. Hand polishing parallel to the stress axis followed low-stress grinding. Specimens were then electropolished as described in Appendix B before testing. This was done to eliminate any detrimental surface effects.

2) ROOM TEMPERATURE LCF TESTING

Tests were performed using a closed looped, servo-controlled, hydraulic MTS machine. All tests were strain controlled, the strain being monitored by an extensometer as shown in Fig. 4. Longitudinal displacement was fed into an X-Y recorder. Hysterises loops were then recorded and periodic adjustments were made to maintain a constant longitudinal plastic strain range. Load and displacement were also monitored using a strip chart recorder. All tests were fully reversed (stress and strain, A = ∞ [ie. amplitude/mean]) and performed at a frequency of 0.33Hz. To minimize test times, some testing was performed at 0.50Hz. All of the room temperature LCF data are shown in Table IV.

Four initiation tests were run using hour-glass specimens. The strain was monitored using a diametral extensometer. The diametral plastic strain range was converted to longitudinal plastic strain range by the equation:[41]

$$\Delta\varepsilon_{\rho}^{d} = 0.5\ \Delta\varepsilon_{\rho}^{l} \qquad \text{.....(8)}$$

where $\Delta\varepsilon_{\rho}^{d}$ = diametral plastic strain range

$\Delta\varepsilon_{\rho}^{l}$ = longitudinal plastic strain range

0.5 = plastic Poisson's ratio

A constant diametral strain range was maintained and all other conditions were identical to those of the longitudinal specimens.

Tests were periodically stopped, the specimens removed and examined under a metallograph in an attempt to follow

slip band development and crack formation. The specimens were then replaced and testing continued.

3) HIGH TEMPERATURE LCF TESTING

Tests were performed as at room temperature with the addition of induction heating (Fig. 4b). The water cooled Cu heating coil was first calibrated using a specimen with five thermocouples (Chromel-Alumel) welded to it as shown in Fig. 5. A region of constant temperature ($\pm$ 5°C) was achieved over the gauge length. This was the actual test temperature. The temperature of the thermocouple on the specimen's shoulder was recorded. This thermocouple was then used as the set point for all subsequent tests. In this way, welding thermocouples to the gauge and perhaps influencing the test results was avoided.

Prior to testing, specimens were maintained at temperature ($\sim$ 20 mins) to ensure thermal equilibrium between the specimen, thermocouple, and the extensometer. The test frequency in all cases was 0.33Hz. LCF data are given in Table VIII.

C) METALLOGRAPHY

1) OPTICAL MICROSCOPY

All specimens were examined under a metallograph to determine the mode of crack initiation and propagation. Specimen preparation is given in Appendix A.

2) SCANNING ELECTRON MICROSCOPY (SEM)

Fractured specimens were examined under the SEM to determine the initiation sites and fracture modes. The gauge of the specimens was also examined for secondary cracking, oxidation, and slip band formation.

3) TRANSMISSION ELECTRON MICROSCOPY (TEM)

Selected specimens were sectioned below the fracture surface as shown in Fig. 5 and examined with the TEM. Foil preparation is given in Appendix B. General microstructures as well as the deformation substructures were examined.

IV RESULTS AND DISCUSSION

A) MATERIAL CHARACTERIZATION

1) GRAIN SIZE

Typical microstructures for the four heat treatments are given in Figures 6 and 7 along with the microstructure for the as-received billet. The grain sizes were; for the coarse grained material an ASTM 3 (average grain diameter $\sim$ 125 μ), and for the fine grained material an ASTM 9 (average grain diameter $\sim$16 μm). The grain size for the as-received billet (Fig. 6C) was between a ASTM 9 and 10 and equivalent in all orientations. Grain sizes were determined by the Heyn's intercept method according to ASTM E112[42] procedures. Lawless[1] and Rehrer[5] et al. determined the temperature for discontinuous grain growth to be about 1030°C (1886°F). Heating above 1030°C caused explosive grain growth. Below this temperature the grains remained about the same size. Thus, the two solutioning temperatures chosen for this program resulted in either a coarse or a fine grained material.

The principal objective of employing four heat treatments was to study grain size and precipitate size effects on fatigue properties. Efforts were made to keep all other microstructural variables constant among the heat treatments. However, as seen below, there were also some differences in the carbide microstructures. TEM and optical evaluations were performed to determine the actual

microstrucutres. These analyses are summarized in Table II.

2. CARBIDE ANALYSIS

a) GRAIN BOUNDARY CARBIDES

The coarse grained, small γ' material (F) showed an absence of grain boundary carbides as seen in Figure 8a. Any boundary carbides that existed in the billet were solutioned at the 1100°C (2012°F) temperature. Absence of these carbides permitted easy boundary movement (i.e. grain growth) to occur. The grains grew from an average diameter of 16 μm in the hot-rolled billet, to an average diameter of 125μ after solutioning.

The coarse grained large γ' material (E) had boundary carbides solutioned. However, as Figure 8b illustrates, some grain boundaries contain a continuous film of carbides. This film, as well as plate-like carbides were also observed on some twin boundaries as in Figure 9. These carbides were of the type $M_{23}C_6$ based on analyses by Lawless[1] and Decker[43] et al. The plate-like carbides have been reported to precipitate during the ageing treatment at twin boundaries and slip bands.[44]

These carbide films and plates have been shown[44] to be deterimental to ductility since they initiate cracks which can easily propagate along the film (or plates) and eventually into the matrix.

Since the boundary carbides were solutioned at 1100°C the continuous films of treatment E must have precipitated during the ageing treatment (875°C/24 hrs.). Decker[4] et al.

showed that $M_{23}C_6$ will precipitate at a temperature of about 815°C (1499°F) at extended times. This explains the difference in boundary morphologies between the two coarse grained materials. The ageing treatment at 875°C precipitated carbides, while ageing at 730°C did not.

Fine grained specimens (both ageing temperatures) showed discrete carbide particles at the grain boundaries (Figures 10 and 11). These particles as well as any unsolutioned restricited grain growth during the solutioning treatment. The grains remained roughly the same size as in the billet, 16 μm.

A difference in size and distribution of the carbides was observed between the two ageinq treatments. The material aged at 875°C for 24 hours showed larger and more abundant particles than did the material aged at 730°C for 6 hours. This was again due to the precipitation and growth of the carbides at 875°C

The discrete carbides account for the etching differences among the heat treatments. As observed in Fig. 11, for a fine grained, large γ' specimen, the carbides are around but not necessarily on the boundary, thus the boundary appears wide in optical metallography. This is in contrast to the coarse grained material (Fig 8a) which had very smooth, well-defined boundaries or a continuous carbide film (coarse grained, large γ') as observed in Fig 8b. Etching caused the fine grained material to exhibit very wide boundaries as if environmentally attacked. This is

especially true upon re-etching as explained in Appendix A.

b) MATRIX CARBIDES

All heat treatments contained groups of matrix particles. These groups were generally aligned parallel to the final rolling direction of the billet. The particles were probably of MC[4] type with some being TiN. The TiN contribution is small and henceforth the particles are considered as MC carbides.

Figures 12 and 13 show the matrix carbides. The fine grained, small γ'(B) material had relatively few particles. This is also representative of the initial billet. As the heat treating temperature increased (i.e. either ageing or solutioning temperature increased), the number and size of the matrix particles increased. The fine grained, large γ' (A) and the coarse grained, small γ'(F) materials showed similar matrix carbide structures. Ageing at 875°C for 24 hours seemed to have the same effect on the carbides as solutioning at 1100°C for 2 hours. The coarse grained, large γ' (E) material had the largest size and volume fraction of carbides. The solution and ageing temperatures precipitated and grew numerous carbides.

The carbide structures of these materials agree with the results of Collins.[45] He studied stabilities of various carbide and intermetallic phases in superalloys. Waspaloy was found to contain only $M_{23}C_6$ and MC carbides. Both carbides formed at temperatures higher than 760°C (1400°F). The abundance of $M_{23}C_6$ increased with increasing

temperature up to a maximum at about 930°C (1700°F). They decreased rapidly from this point until complete solutioning at 1025°C (1875°F). The amount of MC carbides decreased with increasing temperature to a saturation minimum between 815°C (1500°F) and 955°C (1750°F). Their abundance increased up to 1040°C (1900°F) at which point saturation was again observed.

These matrix carbides made mechanical polishing nearly impossible. The carbides separated from the matrix, scratching the surface.

3) GAMMA PRIME γ'

The primary strengthening phase, γ', was examined. As previously discussed, these are spherical, ordered particles which are coherent with the matrix.[4] Their spherical shape is a result of the very low misfit paramter. Their size can affect the deformation mode and hence the damage mechanisms. To effectively study this effect, their diameters were varied by about one order of magnitude. This size variation could be made without changing the volume fraction as suggestion by Stoltz and Pineau.[16]

Figure 14 shows a dark field stereo-pair of the fine grained large γ' precipitates. A duplex structure was observed, with precipitate diameters approximately 900Å and 3000Å. The larger particles were unsolutioned and grew further upon ageing. These large γ' represent about 5% of the total volume fraction of precipitates as measured by a point intercept count.[46] Rehrer[5] et al. determined the γ'

solvus for various Al + Ti percentages in Waspaloy. For a 4.3 wt.% of Al + Ti, the γ' solvus was about 1043°C (1910°F).

Solutioning at this temperature would have caused significant grain growth. Solutioning was performed at a lower temperature (1850°F) even though all the γ' wasn't soltuioned to prevent this grain growth.

When solutioned at 1100°C (E), all the γ' was dissolved. Precipitation at 875°C shows large uniform γ' as seen in Fig. 15. The diameters in this treatment are 1300Å.

Treatment F shows an apparent "absence" of precipitates. However, diffraction patterns contained superlattice spots indicative of this ordered phase. High magnification dark field TEM revealed the γ' (Fig. 14b). Their size was calculated to be 50Å-80Å in diameter. This was substantiated by the work done by Stoltz and Pineau[16] who studied Waspaloy aged at 730°C for 6 hours or 875°C for 24 hours. They reported diameters of 80Å and 900Å respectively. This was similar to the results observed here.

Treatment B (fine grained, small γ'), though only showing a few large γ' (Fig. 10) also had a duplex structure. The large, unsolutioned γ' are about 1500Å in diameter while the unobserved γ' are 50-80Å. The unsolutioned γ' again represent about 5% of the total volume fraction of precipitates.

Large γ' materials exhibited different etching characteristics than the small γ' materials. Figs. 6a and 6b indicate the differences. The large γ' materials over-etched very easily expecially in the boundary regions. All heat treatments had a substantial amount of annealing twins. The apparent absence of the twins in the large materials is due to the over-etching effect. A TEM micrograph (Fig. 16) indicates that the twinning actually existed in the large γ' materials.

B) MONOTONIC TENSILE BEHAVIOR

Tensile results are summarized in Table III by Lawless.[1] The ultimate tensile strengths remained constant. Lawless observed that the yield strength for the fine grained specimens was significantly higher than for the coarsed grain specimens. This is consistent with the Petch[36]-Stroh[37] relationship:

$$\sigma_{ys} = \sigma_o + kd_o^{-1/2} \qquad \text{.....(9)}$$

where σ_{ys} = yield strength

σ_o, k = material constants

d_o = average grain diameter

Lawless[1] also indicated that the heat treatment E (coarse grained, large γ') exhibited "brittle" behavior. No necking was observed for this specimen and the ductility (i.e. reduction in area and fracture strain) was about half of the other treatments. No explanation was given for this. However, examination of the microstructure revealed that this treatment contained continuous grain boundary carbide films and plate-like $M_{23}C_6$. This could certainly cause brittle fracture. In fact, Donachie et al.[44] observed both continuous carbide boundary films and plate or lath-like $M_{23}C_6$ at twin and grain boundaries on some heat treatments of Waspaloy. These treatments exhibited elongations of 8% compared to 26% of other heat treatments. This carbide structure also resulted in low stress rupture elongations and low impact energies.

The two treatments (A and F) chosen for LCF evaluations

have similar tensile properties, even though their microstructures are completely different.

C) ROOM TEMPERATURE LOW CYCLE FATIGUE (LCF)

1) DATA ANALYSIS

LCF properties were obtained from both hour glass and solid longitudinal specimens. Both heat treatments were thoroughly investigated at plastic strain ranges of 3.00% to 0.03%. The data are given in Table IV.

Cumulative glide plots (i.e. $\sigma_{r/2}$ vs. N) for various plastic strain ranges are given in Fig. 17. For both heat treatments, the response stress increases with increasing plastic strain range. Both heat treatments initially harden. However, their continued responses are dissimilar. The fine grained large γ' specimens harden to saturation with only slight softening to failure. The number of cycles to saturation increased with decreasing plastic strain range. For example, the number of cycles to saturation is 24 for $\Delta\varepsilon_p$ = 1.00% compared to $\sim$ 1700 for $\Delta\varepsilon_p$ = 0.06%.

The coarse grained small γ' specimens hardened to a maximum and gradually softened to failure. The maximum stress increased with increasing strain range. However, the cycle at which this maximum occured was relatively constant and independent of the imposed strain (only a slight decrease in the cycle to σ_{max} was observed with decreasing strain).

The stress maximum occurred between 15 and 25 cycles depending upon the specimen.

The hardening and softening observed in the cumulative glide plots (Fig. 17) creates an infinite number of possible cyclic stress-strain curves which can be constructed from the data. It is imperative to explain from what cycle the stress values were taken. For purposes of this report, the stress values were taken at the half life ($N_{f/2}$) which is conventional.

The cyclic σ-ε curve for both treatments is given in Fig. 18. The logarithm of half the stress range ($\sigma_r/2$) taken at half the life ($N_{f/2}$) is plotted versus the logarithm of half the longitudinal plastic strain range ($\Delta\varepsilon_p/2$). As observed, the response stress increases log linearly with increasing strain range. The fine grained material has a higher response stress for equivalent strains as compared to the coarse grained material. This is expected based upon the Petch[36]-Stroh[37] relationship discussed previously and has been reported by various other investigators.

A least squares analysis resulted in values for the slopes of the lines as 0.19 for the fine grained and 0.15 for the coarse grained material. These values are known as the cyclic strain hardening exponents or n'.

The monotonic curves are also plotted (i.e. log tensile stress vs. log $\Delta\varepsilon_p$%) from the equations given by Lawless.[1]

In the plastic strain ranges of interest, both heat treatments cyclically harden over the monotonic condition. Morrow and Tuler[47] found similar results on room temperature LCF of Waspaloy. They observed cyclic hardening over monotonic conditions and a cyclic strain hardening exponent of 0.17.

The Coffin-Manson relationship is presented in Fig. 19. The log $\Delta\varepsilon_p$ Vs. log N_f yields a straight line relationships for the strain ranges investigated. Extrapolation of these curves to 1/4 cycle yields values much higher than the tensile ductility points which implies that the fatigue process is different than that of tensile deformation. The actual curve does not continue straight back to the tensile ductility, but changes slope at approximately $\Delta\varepsilon_p$ 3.00% to a lower value. This break has been observed by others and has been attributed to twinning.[22]

A review of the literature contained a good supply of LCF data for Waspaloy. In each case, the compositions (Table V) are quite similar to that studied here. The heat treatments for each case are also given in Table V. Unfortunately, the initial microstructures were poorly defined. Based upon the heat treatments, a guess at the microstrucutres prior to heat treating, and the limited metallography presented in the reports, an estimate can be made of the microstructures as follows:

Morrow and Tuler[47] machined specimens from a forged turbine disc. As with most discs, the grain size was probably small and is estimated at an ASTM 9 as in the billet used for this thesis. After heat treatment A, the microstructure is believed to contain large grains ($\sim$ ASTM 2-4) with a duplex γ' structure of 500-1000Å and 200Å diameters.

Heat treatment B is believed to contain small grains ($\sim$ ASTM 9) with perhaps three sizes of γ'. These consist of large unsolutioned particles ($\sim$ 1000Å), plus the other two sizes mentioned in treatment A. These structures were estimated based upon the information in the materials characterization section of the report.

Clavel et al.[22] indicated a duplex γ' size (400Å + 2000Å diameters) in their material. Grain size was not mentioned, but based on some micrographs it is belived to be an ASTM 4.

In both cases, fatigue testing was performed at 298K in air using a completely reversed strain cycle ($A = \infty$). Clavel et al. used a frequency of 0.05 Hz. Morrow and Tuler[47] did not report a frequency but at room temperature the results should not depend significantly on frequency so long as the specimen does not heat.

The Coffin-Manson curves are given in Fig 20 for both investigations. In all materials, there are two distinct segments. The high strain values ($\Delta\varepsilon_p \geq 3.00\%$) show a slope of about 0.4. For intermediate strains, the slopes range from 0.65 to 1.0.

Morrow and Tuler[47] reported only test results with no material characterization. Clavel[22] et al. indicated planar slip to be the operative mechanism for $\Delta\varepsilon_p \leq 3.00\%$. Precipitate shearing was also observed. At higher strain ranges twinning was reported. Wilson and Freeman[48] also reported twinning at high $\Delta\varepsilon_p$ in their work on Waspaloy. In all cases, this twinning appeared above the break in the Coffin-Manson curve. Longitudinal specimens tested at $\Delta\varepsilon_p$ = 1.00% for this thesis buckled after a few cycles. However, a test was successfully completed at $\Delta\varepsilon_p$ = 3.00% using an hour-glass specimen. No buckling was observed and the deformation was by planar slip. Clavel et al.[22] used hour-glass specimens while Morrow and Tuler [47] used tubular specimens. Though gross buckling was avoided at $\Delta\varepsilon_p \geq 3.00\%$ by using these specimens, some bending moment may have been introduced. This moment may have induced twinning which was the observed mechanism. This would cause an effective strain higher than the actual recorded value. A shorter fatigue life and a corresponding change in slope would result. It was due to this problem that testing above 3.00% was not attempted in the present study.

Unfortunately, no correlation of microstructure to fatigue life could be made due to limited data. Examination of the materials seemed to reveal increasing fatigue life with decreasing impurity content. A decrease in the carbon content from 0.07 wt.% (Morrow and Tuler) to 0.05 wt.%

(present study) resulted in increases of fatigue lives by more than an order of magnitude. Increases in the tensile ductilities were also observed.

There is little difference in total life (at a given plastic strain range) between the two heat treatments used in this study. A least squares analysis revealed the slopes (i.e. β) as 0.76 for the fine grained and 0.86 for the coarse grained material. Note that the value is positive and a negative slope occurs only in the form

$$\Delta\varepsilon_p = CN_f^{-\beta} \qquad \text{.....(10)}$$

Mathematical relationships have been developed to calculate β from n'. Morrow[49] considered an energy approach which gives:

$$\beta = 1/(1+5n') \qquad \text{.....(11)}$$

Tomkins[50] developed a formula based upon the Duqdale plastic zone model to yield:

$$\beta = 1/(1+2n') \qquad \text{.....(12)}$$

Calculated and measured values of β are given in Table IV. Neither model predicts β with much accuracy.

Saxena and Antolovich[2] suggested a similar model to account for specific slip modes. The slip mode was suggested to affect the rate of damage accumulation by the material as given by:

$$N_f(\Delta W)^{\alpha} = C \qquad \text{.....(13)}$$

where N_f = number of cycles to failure

ΔW = work absorbed per cycle

C, α = slip dependent constants.

This equation is plotted for both treatments in Fig 21. ΔW was calculated by the equation:

$$\Delta W = \Delta\varepsilon_p \sigma_\tau / (1+n') \quad \text{.....(14)}$$

where the symbols have their usual meanings and σ_τ is the stress range taken before the final load drop (explained in a latter section). Since the fine grained material exhibits stress saturation, the value of σ_τ is representative of most of the life. The coarse grained specimens exhibit an increase in stress then a softening to failure. A suitable value for σ_τ represents a problem. Aizaz[51] calculated a mean value of σ_τ over the total life for his analysis of 300 Maraging steel. For purposes of this report, the value was taken as the stress before the development of a macrocrack ($\sim$ 80-90% of N_f).

Saxena and Antolovich[2] predicted that:

$$\beta = 1/(1+n') \quad \text{.....(15)}$$

where α = the slope of the ΔW vs. N_f curve. Calculated values of β (Table VI) correlate well with the measured values.

2) FRACTOGRAPHY

SEM and optical micrographs were obtained from each specimen. In all cases, cracks initiated in many locations and there were various secondary cracks. Typical examples are given.

The coarse grained small γ' materials initiated by a classical Stage I (i.e. slip band) cracking for all plastic strain ranges. The fracture surface for lower strain ranges was more crystallographic than at high strain ranges as observed in Fig. 22. Typical initiation sites are given in Fig. 23. The lower strain range ($\Delta\varepsilon_p$=0.30%) exhibited more Stage I faceting (Fig 23) than did the high strain range ($\Delta\varepsilon_p$ = 3.00%) specimen. Both specimens propagated by a Stage II striation-forming mechanism (Fig. 24). The striations were very fine near the origins, but coarsened as the crack grew and gained velocity (Fig. 24C). Occasionally, carbide particles created dimples in the fracture surface.

Investigations of the gauge surface below the fracture, revealed all coarse grained specimens to have extensive slip band cracking. Fig. 25 shows slip band cracking at initiation points for high and low strain range specimens. A stereo-pair is given in Fig. 26 for the high strain range specimen. Extensive slip band cracking developed into a macro-crack. Areas surrounding the crack are grossly distorted due to the high strains encountered. Areas remote from macro-cracks show extensive slip activity. Slip extrusions and intrusions are observed in the stereo-pair in Fig. 27. One large extrusion initiated slip band cracking at a twin boundary apparently due to high stress concentrations.

Once initiated, the crack propagates along the band as a Stage I crack. Eventually, a striation mechanism takes over. High strain range specimens propagate almost immediately by this striated mechanism. Fig. 28 is a stereo-pair of a slip band initiated crack. As observed, the Stage I mechanism lasts for only a few microns. After this, a distinct river pattern was observed and a Stage II mechanism took over. At lower strain ranges the Stage I mechanism lasts for about one grain. (Fig. 22)

Fig. 29 clearly shows slip bands within the grains. The high strain range specimen has a significantly higher slip band density than does the lower strain range. In fact, Clavel[22] and Diederich[21] found an exponential dependence of slip band spacing (inversely proportional to slip band density) with $\Delta\varepsilon_p$, given by the equation:[21]

$$i = 1.212\ \Delta\varepsilon_p^{-0.518} \quad \ldots\ldots(16)$$

where i = slip band spacing

$\Delta\varepsilon_p$ = plastic strain range

This equation agreed with similar results presented by Clavel et al.[22] on their work on fatigued Waspaloy.

The fine grained large γ' materials have a relatively flat, smooth fracture surface (Fig. 30) compared to the coarse grained material. At all strain ranges, initiation occurred by a Stage I mechanism. Figure 31 indicates initiation sites which were less distinct than those in the coarse grained material, but appear to be crystal facets that were rumpled by plastic activity.

Optical micrographs revealed little damage information. Figure 32 does show some coarse slip bands in a low strain range specimen. These slip bands were the source of crack initiation as observed on the gauge below the fracture surface (Fig. 32b). These bands were wavier than those in the coarse grained material.

Specimen 12 (as with other fine grained specimens) contained areas of large elongated grains (Fig. 33a). These were probably formed by anomalous grain growth. The overall specimen grain size was an ASTM 9. These large grains had no apparent effect on the fatigue properties. Specimen 10 (fine grained) exhibited large differences in the properties and in fact resembled the coarse grained properties. Examination revealed areas which contained large grains approximately 100 μ in diameter (Fig. 33b). These grains were apparently present in the original billet. Probably the amount of cold work was not sufficient to cause complete recrystallization. These grains were equiaxed in shaped and contained annealing twins. Those in Spec. 12 were oblong with few microstructural features. Prior grain boundaries, as observed by the carbide structures, are also noticed in Spec. 10. Due to these anomalies, the data from Spec. 10 were neglected in all calculations.

3) TRANSMISSION ELECTRON MICROSCOPY

After testing, specimens were examined using TEM to determine the deformation substructure. The coarse grained

small γ' specimens experienced inhomogeneous deformation. SEM and optical microscopy showed extensive slip band activity. TEM indicated that deformation was confined to specific slip planes. Figure 34 is a view of these planes for strain ranges of 0.30% and 0.06% (Schmid Factor = 0.42) operating under { 111} reflections. The higher plastic strain range specimen contained a larger density of bands as was indicated in the optical investigations.

Crystallographic orientation of the grains made it possible to determine the specific planes on which slip occurred. Both specimens had slip on { 111 } planes (see Appendix C for details) which is in agreement with planar deformation in fcc materials.[52] The low strain specimen contains multiple slip systems, both of which have the { 111 } orientation.

Figure 35 indicates slip transfer across a grain boundary. Deformation was restricted to the bands and few dislocations were observed between them.

Further investigation of these bands revealed them to contain a tightly spaced network of dislocations. Using a { 200 } reflection, these dislocations became observable inside the band (Fig. 36, $\Delta\varepsilon_p$ = 0.06%). Note the dislocation pairs in the slip bands. Increasing the strain range caused the dislocations to react inside the band. In Fig. 37, $\Delta\varepsilon_p$ = 0.30%) a { 200 } reflection was used to show an almost cellular dislocation arrangement within the slip

band. Beside the slip band are a few dislocation pairs. Due to the extreme fineness of the precipitates, the individual dislocation-precipitate interactions could not be observed. However, the pairs were indicative of precipite shearing.[53] Figure 38 ($\Delta\varepsilon_p$= 0.30%) clearly shows these pairs along a slip band. These dislocations have been determined as a/2 <110> types.[53] The first dislocation cuts and disorders the precipitate while the second is "pulled through" to remove the APB and reorder the precipitate. These pairs have been observed in various other superalloys,[54,55] and in other alloy systems with ordered precipitates.[56,57]

Based upon elementary dislocation theory, a forumla can be derived to estimate the APB energy. The repulsive force between the edge dislocation pairs (edge was chosen rather than screw based upon the analysis in Appendix C. The APB energy was calculated from Fig. C3d) was set equivalent to the amount of APB intersected by the dislocations. The formula was:

$$Gb_1b_2/2\pi \frac{dkf}{\rho} = \gamma_{APB} \quad \ldots\ldots\ldots (17)$$

where G = shear modulus

γ_{APB} = APB energy

$b_1 = b_2$ = a/2 <110> Burger's vector of the two dislocations

d_p= average dislocation pair spacing as viewed perpendicular to the slip plane

k = dislocation factor. k = 1 for screw,

k = $(1-\nu)$ for edge

f = volume fraction of precipitates.

γ_{APB} was calculated to be 56 erg/cm^2. Brown and Ham[58] calculated the APB energy for various Ni alloys. A value of 149 erg/cm^2 was given for a Ni-Al alloy. The APB energy depends upon the precipitate radii and their volume fraction. A Ni-Cr-Al alloy containing precipitates of 110Å diameters and 5% volume fraction (this is close to what was observed in the Waspaloy) gave a value of 89 erg/cm^2. It was clear that the value arrived at for Waspaloy is in agreement with previously measured APB energy.

Fine grained large γ' specimens exhibited a different deformation substructure. The precipitates are large and the dislocations were usually unable to penetrate them. Instead, they frequently bowed around them. Figure 39a shows an edge on view of the bands for a low strain range ($\Delta\varepsilon_p$=0.06%, Schmid Factor = 0.43) specimen. These bands were restricted to { 111 } planes and are also shown (Fig. 39b) for another grain using a { 111 } reflection. The bowing effect was clearly seen in Fig. 39c. The arrow indicates dislocations emitted from a boundary. These dislocations were aligned parallel to the boundary and resembled those in the coarse grained material. A precipitate ahead of them created a back stress restricting the movement of the top portion of the dislocations. The dislocations then moved at an angle to the

boundary. When the precipitate was reached, the dislocations began to bow around it. The structure then became more homogeneous. If the bowed dislocations could pinch-off, they would leave a loop around the precipitate as observed in the same figure in region A.

High strain range specimen N_i 4 ($\Delta\varepsilon_p$ = 1.00%, Schmid Factor = 0.44) contained a higher slip band density as indicated in Fig. 40a. The figure showed an edge on view of the slip planes using a { 111 } reflection. Figures 40b and c showed the looping mechanism (g = {200}) in the same specimen. The precipitates appeared black from the "attached" dislocation loops.

As observed in the figures, the dislocations generally bowed between the precipitates. However, under certain circumstances, even the large precipitates could be sheared. For instance if the precipitates were sufficiently close to each other, the dislocation would not be able to bow between and would instead shear them. Several attempts were made to locate γ' shearing (i.e. an offset precipitate). However, none were observed.

4) INITIATION TESTS

Two tests per heat treatment were run to study the development of cracking during the fatigue test. Hour glass specimens were tested at high and low strain ranges. At various cycles during testing, the specimens were removed,

examined under a metallograph and retested. All micrographs were taken on the specimen gauge. The surface was prepared only by electropolishing prior to testing.

At $\Delta\varepsilon_p$ = 0.12% (N_f = 68020, spec. N_i 1), the fine grained small γ' specimen showed no apparent change on the surface for about 6000 cycles. At 6000 cycles, some grains exhibited slip band formation (Fig. 41). Note that there was only about one band per grain. Another specimen ($\Delta\varepsilon_p$ = 0.12%) was cycled to 6000 cycles and examined under the SEM. Figure 42 shows slip bands on the gauge surface. No cracks were observed. At 9000 cycles, bands began to link-up in adjacent grains (Fig. 41b). More grains now contain these bands. From this point to ~72% of the life (i.e. 49000 of 68020 total cycles), the number of grains with bands increased. There was still little cracking. A high strain range (N_i 4 $\Delta\varepsilon_p$ = 1.00%) specimen showed similar behavior. At ∿ 80% of the life, numerous grains showed bands. The link-up of these bands have initiated cracking. Figure 43 indicates one of these cracks which was ∿ 450 μ in length. This is on the same order of, a 100 μ crack which is usually considered as initiation. It should be noted that the 450 μ is not the crack depth, but the crack length on the surface. Assuming a typical thumbnail crack (as usually observed) the depth would be less, probably about half of this. Assuming this to be an elliptically shaped crack, the load drop corresponding to the reduction in specimen area was

calculated. It was assumed that the specimen showed stress saturation behavior such that the response stress remained constant. Load drops for various crack sizes are given in Table VII. The 450μ crack length resulted in a load drop of $\sim$ 12 lbs. On the strip chart recorder, the difference between the non-cracked load and this cracked load is about 0.2mm. This was too small to effectively detect. A 3mm difference could be detected. This was equivalent to a load drop of 235 lbs. or a crack length of 2000μ . A computer controlled digital readout may have been able to detect cracks much smaller than 450μ .

At 2900 cycles (N_f = 3174, $\Delta\varepsilon_p$ = 1.00%), the load response began to drop considerably. Figure 44 is a load vs. cycles plot from the strip chart recorder for coarse grained small γ' specimen 25 (800°C). This is a typical load vs. cycle curve and is used to illustrate the final load drop. This point is taken by many as initiation. As observed, the crack length at this point is on the order of hundreds of microns. For testing at elevated temperatures, this may be too long. An oxidized grain boundary could easily be cracked by an intersecting slip band. A better value for initiation may be a one grain diameter crack (perhaps even a slip band). This would be $\sim$ 16μ in the fine grained large γ' material.

Coarse grained small γ' specimens exhibited extensive slip band formation at 18 cycles. This corresponded to the maximum stress value for spec. N_i 2 ($\Delta\varepsilon_p$ = 0.15%). Figure

45 shows these bands in various grains. Unlike the fine grained specimens, the coarse grained specimen contained numerous bands per grain. As the material continued to soften, the slip bands filled more of the grains and became more numerous within any given grain. Figure 45b shows the bands at 1000 cycles. Another specimen ($\Delta\varepsilon_p$ = 0.15%) was stopped at 1000 cycles and examined under the SEM. Figure 46 shows slip bands on the gauge surface. No cracks were observed. At 12000 cycles of 41924 cycle life (Fig. 47), the bands began to crack and link-up in adjacent grains. At 2/3 of the life, (27940 of a 41924 cycle life) extensive cracking was observed as seen in Fig. 48. The cracks proceeded from one grain to another via the slip bands. The final load drop did not occur until ~ 90% of the life. In this particular case, the point at which the load begins to rapidly drop off is probably not a good value for N_i.

A high strain specimen (N_i 3, $\Delta\varepsilon_p$ = 3.00%) indicated crack lengths of 500μ at 90% of the life (Fig. 49). This corresponded to the final load drop.

Initiation is hard to define. Various methods have been used to determine this value. One method is the cycle at which there is a 5% drop in the load. This is not very reasonable if the material softens from the beginning of the test as in the case of the coarse grained material used here. The method of using the final load drop seemed to work fairly well for Waspaloy. Figure 44 indicates a load vs. cycles

plot showing the final load drop for a coarse grained small γ' specimen. This drop usually occurred at 85-95% of the life. As observed, this usually corresponded to a crack length of a couple hundred of microns. A crack depth of 100μ is sometimes taken as N_i since it is the value at which a Stage I crack can no longer be sustained in many materials. One should note that this final load drop occurred in a material which had multiple cracks. If this were not the case (i.e. if there were no secondary cracks) this final load drop may occur at much larger crack lengths.

5) ANALYSIS OF ROOM TEMPERATURE LCF MECHANISMS

The fatigue of Waspaloy revealed an initial hardening of both coarse grained small γ' and fine grained large γ' materials. Stopped tests indicated the existence of slip bands at σ_{max}. The coarse grained specimens had much more slip bands per grain at this point. As cycling continued, the fine grained materials showed stress saturation while the coarse grained continually softened to failure. During this time, both materials showed an increase in the number of grains with slip bands, an increase in the number of bands per grain, and link-up of these bands to form cracks. Continued softening of the coarse grained material could perhaps be explained by the following: Most of the slip bands are developed by the time the maximum stress is reached. Continued cycling shears the fine γ' (as evident by dislocation pairs, seen in Figs. 37 and 38) resulting in

a smaller mean radius for other dislocations. An effective smaller γ' radius results in less strengthening capabilities. In addition the slip bands eventually form cracks which are also significant in reducing the response stress. Any new slip bands which form and cause matrix hardening are not sufficient to counter the effects of the two softening mechanisms.

The stress saturation of the fine grained specimens could be explained as follows: At the stress maximum, few bands were developed. Continued cycling produces more bands which tend to harden the material. In addition, the γ' looping creates stress fields thus increasing the resistance to further dislocation motion. Continued cycling would simply shuffle the dislocations around the grain generally without shearing precipitates. Eventually, the dislocations obtain some critical arrangement which results in cracking. In both treatments, the crack becomes sufficiently large to cause a rapid load drop and final failure. This size was observed to be in the hundreds of microns and is perhaps a reasonable value for initiation.

Stoltz and Pineau[16] investigated the fatigue properties of Waspaloy given the same heat treatments used in this thesis. They found similar stress responses; hardening to saturation for the fine grained large γ' material and hardening to a maximum then softening to failure for the coarse grained small γ' material. TEM was performed on stopped tests. The coarse grained material showed slip

bands in the majority of the grains just past the σ_{max} (40 cycles). No dislocations were observed between the bands. The fine grained material revealed broad, loosely organized slip bands at 40 cycles (below σ_{max}). No dislocations were observed between the bands. After saturation, dislocations filled the areas between the bands. Dislocations accumulated on the γ' due to the looping.

Calabrese and Laird[14,17] studied Al-Cu alloys containing both shearable and non-shearable precipitates. Cyclic hardening was observed, followed by softening for alloys containing shearable, ordered precipitates. Hardening was attributed to the build up of dislocations. Dislocation interactions created hardening (i.e. matrix hardening). During this hardening period, a few slip bands formed in the grains. They formed in the first few cycles in grains oriented for maximum shear. Due to the work hardening of these grains, slip bands eventually formed in grains which were less suitably oriented for slip.

Softening was reported as a result of the shearing of the precipitates. A disordering mechanism due to the to and fro cutting motion of the dislocations was suggested. Irreversible cutting caused a break-up of the precipitates and reduced the resistance to dislocation motion.

Lawless[1] reported a significant difference between the fine grained large γ' and the coarse grained small γ' FCP properties. The coarse grained showed crack growth rates

an order of magnitude lower for equivalent ΔK values over the fine grained. As observed, there was little difference in the LCF lives between the two. This might be explained by examining the initiation and propagation stages. The coarse grained material initiates earlier in the life due to the slip band extrusions. Once initiated, the crack propagates slowly due in part to the decreasing stress response. This is evident by the small portion of the crack that is Stage I (Fig. 28). The fine grained material on the other hand, initiates later in life but propagates rapidly owing to the high stress. These two factors have opposing effects and result in equivalent total lives for the size of the specimens used in this study.

D) HIGH TEMPERATURE LCF ANALYSIS

1) DATA ANALYSIS

LCF specimens were tested at 500 and 800°C (both heat treatments) and at 700°C (coarse grained small γ' only). All fatigue data are given in Table VIII. All high temperature tests were performed at $\Delta\varepsilon_p$ = 0.30% and 0.33Hz. The elastic modulus (calculated from the first hysteresis loop) is presented in Table IX. The modulus decreased with increasing temperature and moduli for Waspaloy tested by CEAT[59] are also given for comparative purposes and show the same trend.

Cumulative glide plots (i.e. stress amplitude vs. cycle) are given in Fig. 50. Tests at 700 and 800°C show the same general trends as at room temperature: hardening to saturation for the fine grained material and hardening to a stress maximum then softening to failure for the coarse grained material. The 500°C tests show a unique behavior. Both heat treatments hardened to failure. Stress values at $N_f/2$ (500°C) are equivalent to (fine grained specimen) or higher than (coarse grained specimen) the values for an equivalent strain range when tested at room temperature. To verify this phenomena, a duplicate test was performed using a coarse grained specimen. It was run 1000 cycles at which point significant hardening was observed and testing was stopped.

Examination of the LCF data (Table VIII) revealed that for both heat treatments, the total life decreased with

increasing temperature. These data were plotted in a manner which yields an experimental activation energy for failure. Figure 51 is the plot of ln $(1/N_f)$ vs. 1/T. The hyperbolic shaped curve indicates that this experimental activation energy (which is proportional to the slope) changes with changing temperature. Asymptotic slopes revealed the activation energy, Q, to be 0.10 KCal/M for temperatures of $\sim$ 25-500°C and 7.8 KCal/M for temperatures of $\sim$ 700-800°C. These are in agreement with results for FCP data by Shahinian[60] et al. James[61] et al. and Jablonski[62] et al. Shahinian[60] et al. and James[61] et al. found a hyperbolic type curve in the ln (da/dN) vs. 1/T plots for 316 and 304 SS respectively. In each case, the apparent activation energy was lower for lower test temperatures. Values of $\sim$0.11 KCal/M were found for temperatures between 75 and 300°F and 8.7 KCal/M for temperatures between 800 and 1200°F

Jablonski[62] et al. found a linear relationship for ln (da/dN) vs. 1/T for Multimet (Ni-Fe-Cr-Co alloy). Experimental activation energies ranged from 8.0-12.7 KCal/M for various stress intensities. Data was analyzed only for temperatures between 538-871°C and the change in slope at lower temperatures was not reported.

2) FRACTOGRAPHY

Fractographic examinations were performed on all elevated temperature specimens. Representative micrographs are presented. In each case, multiple cracking was observed.

The fine grained large γ' specimen tested at 500°C Spec. #21 revealed little fractographic information. Figure 52a shows a typical intitation site. Cracks initiate transgranularly and propagate (Fig. 52b) by a striation forming mechanism. Examination of the gauge section (Fig. 53) indicates that initiation was transgranular. Figure 53 also indicates minor grain boundary oxidation around carbide particles. Apparently, boundary oxidation at this temperature was not sufficient to cause intergranular cracking.

Testing at 800°C resulted in both intergranular initiation and propagation (Fig. 54). The fracture surface is heavily oxidized. Fig. 54 also shows preferential grain boundary oxidation and subsequent grain boundary cracking on the gauge surface. The grain interiors are oxidized, but the boundaries exhibit more oxidation forming ridges on the boundaries.

The coarse grained small γ' specimen tested at 500°C exhibited transgranular cleavage type initiations (Fig. 55a). Propagation occurred by a well-defined striated mechanism (Fig. 55b). Gauge examination revealed extensive slip band activity and light oxidation of these bands. Fig. 56 shows cracking following these bands in three adjacent grains.

Specimen #24, tested at 700°C, contained mixed mode cracking. Fig. 57 indicates one crack origin which initiated as a Stage I facet. Transgranular cleavage fracture is observed radiating from the facet. The gauge surface immediately underneath this facet (Fig. 57b) shows extensive

slip band oxidation and some grain boundary oxidation. This was not observed on the room temperature specimens (Figs. 25 and 27). Boundary oxidation resulted in occasional intergranular cracking as observed at another initiation site (Fig. 58a) and in propagation (Fig. 58a). However, striated transgranular cracking was the primary mode of propagation as observed in Fig. 58b.

Specimen 23, tested at 800°C shows extensive intergranular cracking (Fig. 59). Both initiation and propagation occurred by intergranular modes (Fig. 60) with occasional cleavage tearing (Fig. 59b).

Examination of the gauge indicated extensive slip band and grain boundary oxidation. A stereo-pair (Fig. 61) clearly shows oxide ridges on slip bands and grain boundaries. These oxidized boundaries were easily cracked by intersecting slip bands. Fig. 62 shows cracking of an oxidized grain boundary apparently due to the stress concentrations which resulted from slip activity.

Optical micrographs (Fig. 63) indicates slip band activity for all three coarse grained specimens. Slip bands were not as distinct as in the room temperature specimens (Fig. 29).

3) TRANSMISSION ELECTRON MICROSCOPY

Foils were taken from all high temperature LCF specimens as in Fig. 5b. Foils were rigorously examined and typical features were photographed.

The fine grained large γ' specimens tested at 500 and 800°C exhibited deformation by a looping mechanism. Deformation was similar to that observed at room temperature (Fig. 39). Specimen 21 (500°C) exhibited high slip band densities. The density at 500°C and $\Delta\varepsilon_p$ = 0.30% (Fig. 64 . Schmid Factor = 0.35) was higher than the density at room temperature for a $\Delta\varepsilon_p$ = 1.00% (Fig. 40 Schmid Factor = 0.44) Deformation was concentrated on { 111 } planes as observed at room temperature (Fig. 40). Figure 64 taken using a { 111 } reflection indicates edge on views of these planes. At least two active slip systems were indentified for this grain. Precipitates are heavily looped by the dislocations and appear black (Fig. 65). Figure 65b taken using a { 200 } reflection clearly shows the bowing and looping mechanism.

Specimen 22, tested at 800°C, also exhibited γ' looping by dislocations as seen in Fig. 66 ({111 } reflection). No slip bands were observed in the specimen and deformation was more homogeneous.

The coarse grained small γ' specimens exhibited deformation by planar slip. Specimen 20, tested at 500°C, had an extremely dense slip band structure as observed in Fig. 67a. A comparison for an equivalent strain range specimen ($\Delta\varepsilon_p$ = 0.30% Schmid Factor = 0.38) tested at room temperature (Fig. C3a) indicates the room temperature specimen to have a less dense deformation structure. Figure 67b shows the dislocation structure inside the bands (500°C) using a (002) reflection. Dislocations existed in pairs as observed at room

temperature. One grain (Fig. 68) is observed to have three active slip systems. Plane "A" was taken in the edge on condition and had a Schmid factor of 0.41. Schmid factors were 0.50 for plane "B" and 0.44 for "C". This indicates that the internal stresses caused by boundary compatibility requirements were substantial and complex.

The γ' precipitates were observed to coarsen during testing at 500°C. Figure 69a is a dark field micrograph ({300 } reflection) indicating the precipitates. The diameters were 90-120A which was about double the initial size (50-80A).

Carbides were observed to precipitate at some of the grain boudaries. Figure 69b indicates that these carbides were very fine and were plate-like in shape. The particles were observed at only a few places along the grain boundaries.

Specimen 24, tested at 700°C, exhibited a less dense deformation structure than specimen 20 (500°C). Figure 70 shows a grain which contained multiple slip systems (Schmid factor = 0.35). { 111 } reflections show edge on and near edge on (explained in Appendix C) views of each slip system. Included in the micrographs is a grain boundary. Close examination of this boundary revealed it to contain small, discrete boundary carbides as seen in Fig. 71. These carbides were absent in the initial structure (Fig. 8a) and obviously precipitated during testing. Dark field analysis

of these carbides (Fig. 72) reveal a rectangular network of similar carbides above the boundary (i.e. in the grain interior). The carbide network coincided with the slip planes which were observed in Fig. 70. The associated diffraction pattern indicates that these were not γ' particles.

Specimen 23, tested at 800°C, exhibited a low dislocation density. Slip bands were rare and dislocations were loosely organized within them. Several grains had to be examined in order to observe slip bands. Figure 73 shows a multiple slip system within a grain operating under a (022) reflection. Thermal energy was sufficient to anneal some dislocations resulting in lower dislocation densities than observed at other temperatures.

γ' precipitates were observed to grow to $\sim$ 190Å diameters (Fig. 74a). This was about three times the initial 50-80Å size. They appeared to have a chopped-up shape and were not as spherical as prior to testing.

Extensive carbide precipitation was observed at boundaries in this specimen. Figure 74b shows a carbide network at a twin boundary. Stacking faults are observed coming out of the twin. Kear et al.[63] observed similar results for the Ni-base alloy Udimet 700. Cr rich $M_{23}C_6$ carbides precipitated on boundaries between 760 and 900°C. They suggested that the accompanying stacking faults were extrinsic. The faults grew by the climb of Frank partials thru the matrix. Figure 75a shows a grain boundary triple

point filled with carbides. At higher magnification (Fig. 75b) it is observed that the carbides were continuously distributed. These carbides were about 10 times larger than those observed at 700°C (specimen 24, Fig. 71). No carbides were observed on slip bands as in the 700°C test.

4) HIGH TEMPERATURE LCF ANALYSIS

The fatigue deformation substructure of Waspaloy tested at elevated temperatures showed similarities to that observed at room temperature. The fine grained large γ' material exhibited homogeneous slip or Orowan looping. The coarse grained small γ' material exhibited inhomogeneous slip with precipitate shearing as evident by the dislocation pairs. One primary difference between room temperature and elevated temperature tests was the decrease in life with increasing temperature. This is the usual case for polycrystalline materials.[28] Many reasons have been attributed to this decrease, such as environmental interactions,[30], creep and structural instabilities.[26]

As temperature increases, the tendency for the metal to oxidize becomes greater. Tests at 500°C exhibited surface discoloration due to oxidation. 700 and 800°C tests had grain boundary, slip band, and fracture surface oxidation. The effects of oxidation cannot be separated from the other damage factors, but some important observations suggest that it is a critical damage mode.

Antolovich[34] et al. suggested that failure occurred by the development of oxide spikes or poisoned boundaries for Rene' 80 tested at 871 and 982°C. These attained a critical length and resulted in failure. The dislocation substructure consisted of interfacial edge dislocations on the cube faces of the γ'. It was suggested that this structure reduced the strain energy of the matrix but was not damaging.

Grain boundary oxidation can sufficiently embrittle a boundary and cause intergranular cracking. A planar slip material results in stress concentrations at the grain boundaries and can cause cracking of an oxidized boundary as shown in Fig. 62. A more homogeneous deformation structure may not cause such concentrations and as a result, not crack the oxidized boundary. It was interesting to note that both heat treatments (one having planar slip, the other having homogeneous slip) had the same fatigue lives at high temperatures. This was especially true at 800°C where both materials exhibited intergranular cracking. Environmental effects were apparently more important to the failure criterion than the actual slip mechanisms.

At the lower temperatures (i.e. 500 and 700°C), fracture surfaces revealed areas of cleavage fracture. This is typical of brittle type failure, perhaps suggesting the influence of oxidation.[64]

Analysis of the experimental activation energies (Fig. 51) showed that it increased with increasing temperature. The "Q" values represent some overall damage process

activation energy which is probably comprised of oxidation, creep, and other stress assisted mechanisms. It is important to note that the asymptotic value of 7.8KCal/M occurs at temperatures where intergranular fracture was observed. Ericsson[65], on his review of oxidation effects, suggested that the small activation energies ($\sim$10KCal/M) indicates that the rate controlling process is not thermally activated. Perhaps a better statement may be that it is a stress assisted mechanism and not entirely thermally controlled (such as the case of self diffusion). At lower temperatures such as 25-300°C, the damage process is apparently not thermally activated, but is only stress activated as indicated by the low activation energy. It is reasonable to assume that as the temperature approaches absolute zero, Q would approach zero and the material would be infinitely brittle.

Oxidation has been observed to increase with stress application. McMahon and Coffin[66] noticed that the depth of grain boundary oxidation increased with increasing stress for the Nickel base alloy Udimet 500. Grain boundary oxide spikes were observed to be longer at the minimum cross-section (i.e. the maximum stress) of hour glass specimens. As the cross-sectional area became larger (i.e. the stress dropped), the spikes became shorter.

Stress assisted oxidation could perhaps explain the high dislocation densities and the increase in the response stress of the 500°C specimens. No copious oxidation was observed,

but surface discoloration was apparent. If small amounts of oxygen diffused into the specimens, this could restrict slip reversibility and even hinder dislocation motion. Oxygen diffusion would not be large enough to cause severe embrittlement. To maintain a constant plastic strain range to this "hardened" material, more dislocations must be generated and additional slip bands must be activated. Such was the case at 500°C in this study where the dislocation densities were extremely high.

Restriction of slip reversibility by oxygen has been suggested to cause the formation of striations.[67] It also has been suggested to increase the fatigue lives of MarM 200 single crystals compared to those of vacuum tested specimens.[40]

Fujita[68] suggested that slip may enhance oxidation diffusion by the method pictured in Fig. 76. Active slip bands create intrusions and extrusions on the surface. These extrusions have sufficient time to become oxidized. Upon reversing the cycle, the slip extrusion may disappear by a reverse motion. Oxide on the once extruded plane surface will be spalled off while oxygen just below the oxide/metal interface (i.e. that diffused in a few atoms distance) will be pulled into the grain interior. Continued cycling could move these atoms throughout the entire specimen. This diffusion could also be enhanced by the movement of dislocations through the lattice. This is certainly feasible since edge dislocations contain an area of lattice expansion under the

extra half plane. Interstitial atoms such as oxygen can easily fit into this area and in fact reduce the energy of the system.

A similar explanation could be used for γ' coarsening at elevated temperatures. There was limited coarsening of the precipitates when statically heat treated at 800°C (Fig. 77). However, cycling caused rapid growth at temperatures as low as 500°C. The stress assisted diffusion by slip plane and dislocation motion apparently resulted in coarsening. Another important factor may be the increase in surface area of the γ' due to it's shearing. Precipitate growth was not evident in the fine grained large specimens where shearing did not occur and where the driving force would be lower.

$M_{23}C_6$ carbides began to precipitate at grain boundaries at temperatures as low as 500°C in tested coarse grained small γ' specimens. Specimen 24 (700°C) had discrete particles at grain boundaries (Fig. 71). No carbide change was observed in the fine grained large γ' specimens since there were already carbides existing prior to testing and there was no unstable supersaturation of carbon in the material.

Apparently, there was a regime in which there was both thermal and athermal energy supplied to the process. This range appeared to fall in the "elbow" region (i.e. 500-700°C) of the activation energy graph. Above these temperatures, the process appeared to be thermally controlled. The species could diffuse to their lowest energy positions.

This was the grain boundaries for carbides. At slightly lower temperatures, the stress assistance constituted a large portion of the diffusion mechanism and the carbides may precipitate on the slip bands before reaching the grain boundaries. Such nucleation was treated by Cahn,[69] assuming an elastic dislocation model and an incoherent precipitate matrix interface. The change in free energy, ΔG, for the formation of a cylindrical nucleus was given as the sum of the strain energy reduction, the surface energy, and the volume energy and given by the equation:

$$\Delta G = -A (\log r) + 2\pi\gamma_E r + \pi r^2 \Delta G_v \quad .....(18)$$

where r = radius of the precipitate per unit length

A = elastic constant for dislocations taken as $Gb^2/4\pi(1-\nu)$ for edge and $Gb^2/4\pi$ for screw

γ_E = surface energy

ΔG_v = change in the volume free energy

If $|2A \cdot \Delta G_v| < \pi\gamma_E^2$ then ΔG passes thru a minimum at r_o, increases to a maximum at r_c and then rapidly decreases. r_o was a radius approximately equal to the size of a Cottrell atmosphere and r_c was the critical nucleus size. If $|2A \cdot \Delta G_v| > \pi\gamma_E^2$ then there was no barrier ($\Delta G_{r_c} - \Delta G_{r_o}$) for nucleation. More generally, with increasing precipitate radius, nucleation becomes more favorable. Even with the barrier, it was much lower due to the strain term (i.e. -A [log r]) than that associated with homogeneous nucleation. For typical conditions, it was shown

that nucleation on dislocations (or in this study, slip planes) occurred 10^{78} times faster than homogeneous nucleation and the observation of this study are in general agreement with this theoretical model.

V SUMMARY AND CONCLUSIONS

The room and elevated temperature properties of Waspaloy were studied. Two microstructures were employed, one containing coarse grains and small γ' and the other containing fine grains and large γ'.

Room Temperature

1) Coarse grained small γ' specimens tested at room temperature exhibited Stage I crack initiation and transgranular propagation. Slip occurring on { 111 } planes and precipitate shearing was observed.
2) Fine grained large γ' specimens exhibited Stage I initiation and transgranular propagation. Slip was confined to { 111 } planes. Dislocations looped the large γ'.
3) The stress response for the coarse grained specimens was hardening to a maximum and then softening to failure.
4) The coarse grained and fine grained specimens exhibited approximately equivalent LCF lives per equivalent strain range.

Elevated Temperatures

1) Coarse grained small γ' specimens exhibited transgranular cracking when tested at 500°C. At 700°C, cleavage, faceting and intergranular cracking was observed. Intergranular and cleavage cracking was observed at 800°C.

Fine grained large γ' specimens exhibited transgranular cracking at 500°C. Intergranular cracking was observed at 800°C.

3) Observed deformation substructures were planar slip ({ 111 } planes) and precipitate shearing for the coarse grained specimens and planar slip ({ 111 } planes) and precipitate looping for the fine grained specimens. No slip bands were observed in the fine grained specimen tested at 800°C

4) Carbides precipitated in the grain boundaries of coarse grained specimens at 500, 700 and 800°C. Carbides also precipitated on slip planes at 700°C. Carbide precipitation or growth was not observed in the fine grained material.

5) γ' precipitates grew at 500, 700 and 800°C in the coarse grained material. Their growth was assisted by plastic deformation. No γ' growth was observed in the fine grained materials.

6) A decrease in the fatigue life was observed for increasing temperatures. Both heat treatments exhibited similar LCF lives for equivalent strain ranges and temperatures.

7) Stress responses for both heat treatments were similar to those at room temperature with the following exceptions: a) The stress level decreased with increasing temperature and b) At 500°C, both heat treatments exhibited continual hardening to failure. These specimens also exhibited

very dense deformation structures.

8) A plot of ln $1/N_f$ vs. $1/T$ revealed a hyperbolic type curve whose slope was proportional to the experimental activation energy, Q. At low temperatures, Q approached zero indicating that the failure was athermally activated. At high temperatures, Q = 7.8 KCal/M which suggested that thermal activation played a large role in failure. In between, there were both thermal and athermal components controlling failure.

VI REFERENCES

1 Lawless, B. H., "Correlation Between Cyclic Load Response and Fatigue Crack Propagation Mechanisms in the Ni-Base Superalloy Waspaloy," Masters Thesis, University of Cincinnati, 1980.

2 Saxena, A. and Antolovich, S. D., "Low Cycle Fatique, Fatique Crack Propagation and Substructures in a Series of Polycrystalline Cu-Al Alloys," Met. Trans., Vol. 6A, 1975, pp. 1809-1828.

3 Beardmore, P., Davies, R. G., and Johnston, T. L., "On the Temperature Dependence of the Flow Stress of Nickel-Base Alloys," AIME Trans., Vol. 245, 1969, pp. 1537-1545.

4 Decker, R. F. and Sims, C. T., "The Metallurgy of Nickel-Base Alloys," The Superalloys, Eds. Sims, C.T. and Hagel, W.C., 1972, pp. 33-77

5 Rehrer, W. P., Muzyka, D. R., and Heyatt, G. B., "Solution Treatment and Al + Ti Effects on the Structure and Tensile Properties of Waspaloy," Journal of Metals, 1970, pp. 32-38.

6 Sims, C. T., "The Occurrence of Topologically Close-Packed Phases," The Superalloys, Eds. Sims, C. T. and Hagel, W. C., 1972, pp. 259-284.

7 Woodyatt, L. R., Sims, C. T. and Beattie, Jr,. H. J., "Prediction of Sigma-Type Phase Occurrence from Compositions in Austenitic Superalloys," AIME Trans., Vol. 236, 1966, pp. 519-526.

8 Luetjering, G. and Weissman, S., "Mechanical Properties of Age Hardened Titanium-Aluminum Alloys," Acta Met., Vol. 18, 1970, pp. 785-795.

9 Mitchell, W. I., "Ausscheidungshaertung, von Hochtemperaturlegierungen auf NickelBasis," Zeitschrift Fur Metallkunde, Vol. 57, 1966, pp. 586-589.

10 Gleiter, H. and Hornbogen, E., Physica Status Solidi, Vol. 12, 1965, pp. 251-264.

11 Brown, L. M. and Ham, R. K., Strengthening Methods in Crystals, Elsevier Amsterdam, 1971, pp. 9-135.

12 Copley, S. M. and Kear, B. H., "A Dynamic Theory of Coherent Precipitation Hardening with Application to Nickel-Base Superalloys," AIME Trans., Vol. 239, 1967, pp. 984-992.

13 Orowan, E., "Effects Associated with Internal Stresses: (a) Effects on a Microscopic and Sub-Microscopic Scale," Symposium on Internal Stresses in Metals and Alloys, 1948, pp. 451-453.

14 Calabrese, C. and Laird, C., "Cyclic Stress-Strain Response of Two-Phase Alloys Part I. Microstructures Containing Particles Penetrable by Dislocations," Materials Science and Engineering, Vol. 13, 1974, pp. 141-157.

15 Silcock, J. M., Heal, T. J. and Hardy, H. K., "Structural Ageing Characteristics of Binary Aluminum-Copper Alloys," Journal of the Institute of Metals, Vol. 82, 1953, pp. 239-248.

16 Stoltz, R. E. and Pineau, A. G., "Dislocation-Precipitate Interaction and Cyclic Stress-Strain Behavior of a Strengthened Superalloy," Materials Science and Engineering, Vol. 34, 1978, pp. 275-284.

17 Calabrese, C. and Laird, C., "Cyclic Stress-Strain Response of Two-Phase Alloys Part II. Particles Not Penetrated by Dislocations," Materials Science and Engineering, Vol. 13, 1974, pp. 159-174.

18 Sanders, Jr. R. E. and Starke, Jr. E. A., "The Effect of Grain Refinement on the Low Cycle Fatigue Behavior of an Aluminum-Zinc-Magnesium (Zirconium) Alloy," Materials Science and Engineering, Vol. 28, 1977, pp. 53-68.

19 Fournier, D. and Pineau, A., "Low Cycle Fatigue Behavior of Inconel 718 at 298K and 823K," Met. Trans., Vol. 8, 1977, pp. 1095-1105.

20 Merrick, H. J., "The Low Cycle Fatigue of Three Wrought Nickel-Base Alloys," Met. Trans., Vol. 5, 1974, pp. 891-897.

21 Diederich, D., "A Study of Fatigue Plastic Zones in Waspaloy," Senior Research Project University of Cincinnati, 1981.

22 Clavel, M., Levaillant, C., and Pineau, A., "Influence of Micromechanisms of Cyclic Deformation at Elevated Temperature on Fatigue Behavior," Creep-Fatigue-Environment Interactions, Ed. R. M. Pelloux and N. S. Stoloff, AIME, 1980, pp. 24-45.

23 Paris, P. C. and Erodogan, F., "A Critical Analysis of Crack Propagation Laws," Trans of ASME, J. of Basic Eng., Vol. 85, 1963, pp. 528-534.

24 Merrick, H. F. and Floreen, S., "The Effects of Microstructure on Elevated Temperature Crack Growth in Nickel-Base Alloys," Met. Trans., Vol. 9A, 1978, pp. 231-236.

25 Bartos, J. and Antolovich, S. D., "Effects of Grain Size and Size on Fatigue Crack Propagation in Rene 95," Fracture, Vol. 2, 1977, pp. 995-1005.

26 Antolovich, S. D., "Metallurgical Aspects of High Temperature Fatigue," Paper Presented at Sherbrooke Canada, 1978.

27 Wells, C. H., "High-Temperature Fatigue," Fatigue and Microstructure, 1979, pp. 307-333.

28 Tomkins, B. and Wareing, J., "Elevated-Temperature Fatigue Interactions in Engineering Materials," Metal Science, Vol. 11, 1977, pp. 414-424.

29 Runkle, J. C. and Pelloux, R. M., "Micromechanisms of Low-Cycle Fatigue in Nickel-Based Superalloys at Elevated Temperatures," Fatigue Mechanisms, Ed. Fong, J. T., ASTM STP 675, 1979, pp. 501-527.

30 Coffin, Jr. L. F., "The Effect of High Vacuum on the Low Cycle Fatigue Law," Met Trans., Vol. 3, 1972, pp. 1777-1788.

31 Bashir, S., Taupin, P., and Antolovich, S. D., "Low Cycle Fatigue of As-HIP and HIP + Forged Rene 95," Met Trans, Vol. 10A, 1979, pp. 1481-1489.

32 Antolovich, S. D., Rosa, E., and Pineau, A., "Low Cycle Fatigue of Rene 77 at Elevated Temperature," Materials Science and Engineering, Vol. 47, 1981, pp. 47-57.

33 Antolovich, S. D., Domas, P., and Strudel, J. L., "Low Cycle Fatigue of Rene 80 as Affected by Prior Exposure," Met. Trans., Vol. 10A, 1979, pp. 1859-1868.

34 Antolovich, S. D., Liu, S., and Baur, R., "Low Cycle Fatigue Behavior of Rene 80 at Elevated Temperature," Met. Trans., Vol 12A, 1981, pp. 473-481.

35 Prager, M. and Sines, G., "Embrittlement of Precipitation Hardenable Nickel-Base Alloys by Oxygen," ASME Trans., Journal of Basic Engineering, 1971, pp. 225-230.

36 Petch, N. J., "The Cleavage Strength of Polycrystals," Journal of Iron and Steel Inst., Vol. 174, 1953, pp. 25-28.

37 Stroh, A. N., Advances in Physics, Vol. 6, 1957, pp. 418-465.

38 Pilling, N. B., and Bedworth, R. E., "The Oxidation of Metals at High Temperature," Journal of the Institute of Metals, No. 1, Vol. 29, 1923, pp. 529-591.

39 Romanoski, G., "A Study of Mechanisms of Deformation and Fracture in HTLCF of Rene 80 and IN-100," Masters Thesis University of Cincinnati, 1981.

40 Duquette, D. and Gell, M., "The Effects of Environment on the Elevated Temperature Fatigue Behavior of Nickel-Base Superalloy Single Crystals," Met. Trans., Vol. 3A, 1972, pp. 1899-1905.

41 Hirschberg, M. H., "A Low Cycle Fatigue Testing Facility," Manual on Low Cycle Fatigue Testing, ASTM STP 465, 1969, pp. 67-86.

42 ASTM E 112-74, "Estimating the Average Grain Size of Metals," pp. 208-235.

43 Decker, R. F., "Strengthening Mechanisms in Nickel-Base Superalloys," Paper Presented at the Steel Strengthening Mechanisms Symposium Zurich, Switzerland, 1969.

44 Donachie, M. J., Pinkowish, A. A., Danesi, W. P., Radavich, J. F., and Couts, W. H., "Effect of Hot Work on the Properties of Waspaloy," Met. Trans., Vol. 1, 1970, pp. 2623-2630.

45 Collins, H. E., "Relative Long-Time Stability of Carbide and Intermetallic Phases in Nickel-Base Superalloys," Transactions of the ASM, Vol. 62, 1969, pp. 82-104.

46 Underwood, E. E., "Statistically Exact Expressions for Points, Lines, Surfaces, and Volumes," Quantitative Stereology, 1970, pp. 23-47.

REFERENCES (con't)

47 Morrow, J. and Tuler, F. R., "Low Cycle Fatigue Evaluation of Inconel 713C and Waspaloy," ASME Trans., Journal of Basic Engineering, 1965, pp. 275-289.

48 Wilson, D. J. and Freeman, J. W., "The Dependence of Mechanical Characteristics of Waspaloy at 1000-1400°F on the Gamma Prime Phase," NASA Report, CR-72572.

49 Morrow, J., ASTM-STP-378, 1965, p. 45.

50 Tomkins, B., "Fatigue Crack Propagation - An Analysis," Philosophical Magazine, Vol. 18, 1968, pp. 1041-1065.

51 Aizaz, A., "Low Cycle Fatigue, Fatigue Crack Propagation and Microstructure in High Purity and Commercial 300 Grade Maraging Steel," Masters Thesis, University of Cincinnati, 1978.

52 Hull, D., "Dislocations in Face-Centered Cubic Crystals," Introduction to Dislocations, 1975, pp. 101-121.

53 Hull, D. "Dislocations in Other Crystal Structures," Introduction to Dislocations, 1975, pp. 139-144.

54 Davies, R. G. and Stoloff, N.S., "On the Yield Stress of Aged Ni-Al Alloys," AIME. Trans., Vol. 233, 1965, pp. 714-719.

55 Inoue, A., Kojima, Y., Minemura, T., and Masumoto, T., "Microstructure and Mechanical Properties of Ductile Ni_3Al-Type Compound in Fe-(Ni, Mn)-Al-C Systems Rapidly Quenched from Melts," Met. Trans., Vol. 12, 1981, pp. 1245-1253.

56 Bell, W., Roser, W. R., and Thomas, G., "Diffraction Analysis of Dislocation Pairs for Detecting Order in Solid Solutions," Acta Met., Vol. 12, 1964, pp. 1247-1253.

57 Marcinkowski, M. J., Brown, N., and Fisher, R. M., "Dislocation Configurations in $AuCu_3$ and AuCu Type Superlattices," Acta Met., Vol. 9, 1961, pp. 129-137.

58 Brown, L. M. and Ham, R. K., Strengthening Mechanisms in Crystals, Ed. Kelly, A. and Nicholson, R. B., 1972, pp. 96-113.

59 Perruchet, C., "Contribution A L'Evaluation De La Methode Strain Range Partitioning Application A L'Alliage Base Nickel Waspaloy," Characterization of Low Cycle High Temperature Fatigue by the Strain Range Partitioning Method, AGARD-CP-243, 1978, pp. 9-1 - 9-19.

60 Shahinian, P., Smith, H. H., and Watson, H. E., "Fatigue Crack Growth in Type 316 Stainless Steel at High Temperature," ASME Trans., Journal of Engineering for Industry, 1971, pp. 976-980.

61 James, L. A. and Schwenk, E. B. Jr., "Fatigue-Crack Propagation Behavior of Type 304 Stainless Steel at Elevated Temperatures," Met. Trans., Vol. 2, 1971, pp. 491-496.

62 Jablonski, D. A., Carisella, J. V., and Pellous, R. M., "Fatigue Crack Propagation at Elevated Temperatures in Solid Solution Strengthened Superalloys," Met Trans., Vol. 8A, 1977, pp. 1893-1900.

63 Kear, B. H., Oblak, J. M., and Giamei, A. I., "Stacking Faults in Gamma Prime $Ni_3(Al, Ti)$ Precipitation Hardened Nickel Base Alloys," Met Trans., Vol. 1, 1970, pp. 2477-2486.

64 Fractography and Atlas of Fractographs, ASM Metals Handbook, Vol. 9, 1974, pp. 64-78.

65 Ericsson, T., "Review of Oxidation Effects on Cyclic Life at Elevated Temperature," Canadian Metallurgical Quarterly, Vol. 18, 1979, pp. 177-195.

66 McMahon, C. J., and Coffin, L. F. Jr., "Mechanisms of Damage and Fracture in High-Temperature, Low-Cycle Fatigue of a Cast Nickel-Based Superalloy," Met Trans., Vol. 1, 1970, pp. 3443-3450.

67 Pelloux, R. M., "Mechanisms of Formation of Ductile Fatigue Striations," ASM Trans Quarterly, Vol. 62, 1969, pp. 281-285.

68 Fujita, F. E., "Oxidation and Dislocation Mechanisms in Fatigue Crack Formation," Fracture of Solids, Eds. Drucker, D. C., and Gilman, J. J., 1962, pp. 657-670.

69 Cahn, J. W., "Nucleation on Dislocations," Acta Met, Vol. 5, 1957, pp. 169-172.

70 Martin, K., "A Preliminary Study of the Effect of Microstructure on the Low Cycle Fatigue Behavior of Waspaloy," Senior Project, University of Cincinnati, 1980.

71 Dubois, L. G., "Effect of Deformation Mechanism on Constant Amplitude and Single Peak Overload Fatigue Behavior of Waspaloy," Senior Research Project, University of Cincinnati, 1978.

72 Hirsch, P. B., Howie, A., Nicholson, R. B., Pashley, D. W., and Whelan, M. J., "Kinematical Theory of Image Contrast," Electron Microscopy of Thin Crystals, London Chapter 7, 1967, pp. 176-182.

73 CRC, Handbook of Chemistry and Physics, Ed. Weast, R. C., 1971.

Page Missing in Original Document

APPENDIX A

METALLOGRAPHIC PREPARATION

MOUNTING

Specimens submitted for metallography were sectioned to size on an abrasive cut-off wheel. The wheel was a resin bonded Al_2O_3 type (Buehler Ltd. product #10-4112). Sufficient cooling water was applied to prevent heating of the specimen and possible structural change. Cut sections were then mounted in an epoxide mounting material. Alumina particles (+150 mesh) were added to the mount to insure good edge retention upon polishing.

POLISHING

Mounts were hand ground on silicon carbide discs mounted on motor driven polishing wheels. Mounts were ground on 180, 240, 320, 400 and 600 grit papers successively. Specimens were then hand polished on lapping wheels. These wheels were covered with a short-napped felt cloth (similar to billiard cloth) and impragnated with an Alumina slurry. Successive Alumina particle sizes were used: 15 μ , 1 μ , 0.3 μ and 0.05 μ. This provided a surface suitable for viewing under a metallograph.

ETCHING

Unless otherwise indicated, the etching reagant used was a solution of:

15ml HCl (37% solution)
10ml HNO_3 (70% solution)
10ml Acetic Acid (Glacial)

Specimens were immersed in the reagant for approximately one minute at room temperature. This etchant proved suitable for deliniating grain boundaries as well as slip bands.

When necessary, specimens were etched, repolished and re-etched to provide more microstructural details. In doing this however, the specimens had to have some surface material removed, or the grain boundaries would appear very wide upon re-etching.

Specimens were photographed on a Reichert MeF metallograph when necessary.

APPENDIX B

TEM FOIL PREPARATION AND EXAMINATION

FOILS

Specimens submitted for TEM evaluation were sectioned appropriately. 0.010" thick wafers were cut from the specimen. These wafers were further sectioned to 3mm X 3mm squares. All sectioning was done on a Bronwill thin sectioning machine. A slow feed rate and ample coolant prevented specimen heating and possible change of the substructure.

The squares were hand ground on both surfaces on 180 and 600 grit silicon carbide paper to a thickness of 0.004". The foils were then electropolished by a dual-jet unit until suitable for viewing.

The electrolyte was:

45ml Acetic Acid (Glacial)
45ml Butyl Cellusolve
10ml Perchloric Acid (70% solution)

This solution was used at a temperature of $\sim$8°C. The polishing conditions were $\sim$20mA and $\sim$35V for a time of about five minutes. These conditions were also used for polishing the LCF specimens prior to testing.

This solution had no apparent detrimental effects on the material. The resulting microstructure was similar to that observed by others for Waspaloy in which other foil making techniques were used.

TEM

The microscope used to examine the foils was a JEOL JEM-200A. This model has a three lens 200KV potential. A beam deflector made it possible to do high resolution center dark field work. All dark field work was done in this manner.

The stage was equipped with a 30° tilt capability with a 360° azimuthal control. Such a device provided an effective tilt range of 60°. Thus orientation work as well as tilting experiments were performed.

APPENDIX C

SLIP PLANE DETERMINATION

TEM was used to determine the slip planes. This procedure is shown for coarse grained small γ' specimen #5 tested at room temperature and $\Delta\varepsilon_p = 0.06\%$.

The grain was first oriented and a stereo-graphic projection constructed as observed in Fig. C1. As can be seen in this case, the beam corresponds to [121] direction.

The angle of the slip planes from the North-South axis was then determined. The protractor screen in the TEM (Fig. C2) provided this information. For this particular grain, there were two active slip systems. Fig. C2 shows their orientation with respect to the protractor screen. Slip band "A" was at an angle of 80° from the N-S axis and plane "B" was 32° from the N-S axis. The aximuth (i.e. the axis about which tilting occurred) was rotated to correspond to one of the planes. In this manner, tilting would occur about the axis of the slip plane. An extra 10° rotation with respect to the diffraction pattern for which the screen was determined, was added to account for an image rotation at a magnification of 10,000X. The azimuthal angles were 255° and 75° for plane "A" and 302° and 122° for plane "B". The two values per plane are given since the tilt stage does not rotate a full 90°. The 180° shift in azimuth gave an effective tilt range of 60° (i.e. $\pm$ 30°).

Figures C3a thru d are micrographs showing tilting about the planes axis. As observed (Fig. C3a and C3d), the planes are edge-on when they are the thinnest. At this point, the g-vector is perpendicular to the plane. Tilting away from this edge-on condition increases the band width as observed in the other figures.

The reflections which illuminated these planes in the edge-on conditions were the $(\bar{1}11)$ for plane "B" and the $(11\bar{1})$ for plane "A". These were the active slip planes. The stereo-graphic projection (Fig. C1) indicates that for an azimuth of 75°, which corresponded to plane "B's" tilt axis, the $(\bar{1}11)$ reflection fell outside of the 30° tilt range. True edge-on character could not be achieved. Changing the azimuth to 122° made it possible to bring up the $(\bar{1}11)$ reflection. This was called a "near-edge" condition. In this position, the plane had limited width and the g-vector was almost perpendicular to the plane.

Figures C3a thru C3d were used to determine the orientation of the dislocation line and the Burger's vector for plane "B". Dislocations are evident in Fig. C3d. The dislocations therefore lie in the $(11\bar{1})$ plane which was the operating reflection. By Fig. C3a it is observed that they are also contained in the $(\bar{1}11)$ plane or plane "B". The only direction common to both planes is the [101] (See Fig. C1). This is the line direction of the dislocations. The Burger's vector was determined by the g.b = 0 invisibility criterion.[72] In Fig. C3a, the dislocations are almost invisible for

g = [$\bar{1}$11]. The [110] direction is 90° from [$\bar{1}$11] and is therefore the corresponding Burger's vector. As observed in the stereo-graphic projection (Fig. C1), [110] was 56° from [101]. The dislocations are therefore of mixed character, but show stronger edge characteristics. This explains why the g.b = 0 invisibility criterion (Fig. C3a) did not cause complete extinction of the slip planes. Invisibility occurs for only pure screw dislocations.

Analysis of the stereo-graphic projection indicates that slip should have occurred on the ($\bar{1}$11) and (11$\bar{1}$) planes. Schmid factors for all { 111 } planes and <110> directions are given in Table C1. As observed, the ($\bar{1}$11) [110] system and the (11$\bar{1}$) [011] system have the highest Schmid factor (0.38) and therefore the highest resolved shear stress. Since both have equivalent Schmid factors, slip could occur on either system just as easily. This was indeed the case as observed in Figs. C3a-d.

TABLE CI

Schmid Factors

	[011]	[110]	[10$\bar{1}$]	[101]	[01$\bar{1}$]	[$\bar{1}$10]
($\bar{1}$11)		0.38		0.28	0.04	
(11$\bar{1}$)	0.38			0.28		0.03
(111)			0.00		0.10	0.07
(1$\bar{1}$1)	0.06	0.06	0.00			

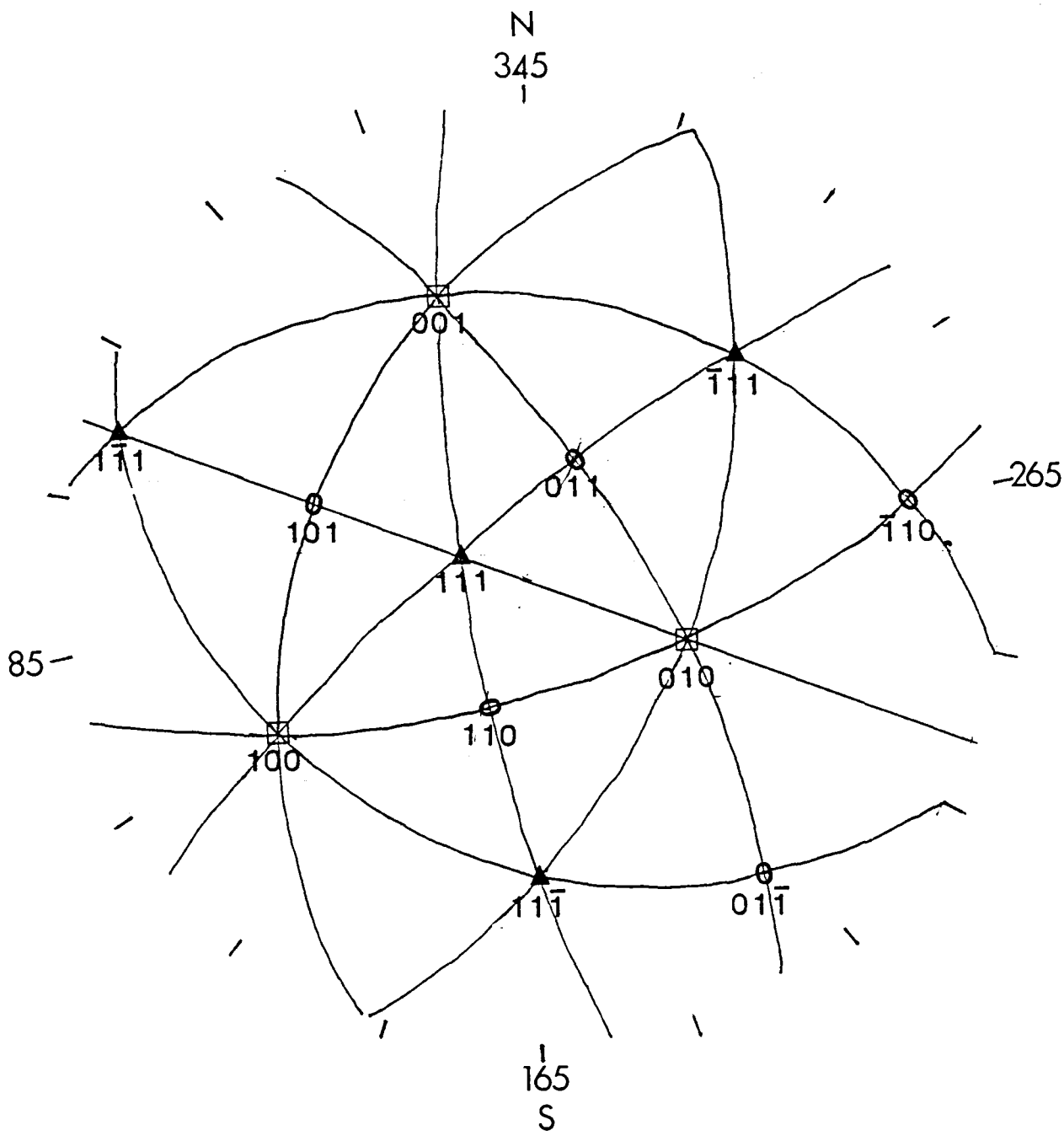

Figure C1 Stereo graphic projection of a grain in near [112] orientation. Slip had occurred on the (111) [110] and (11$\bar{1}$) [011] systems. Azimuthal angles are given on the outside of the projection.

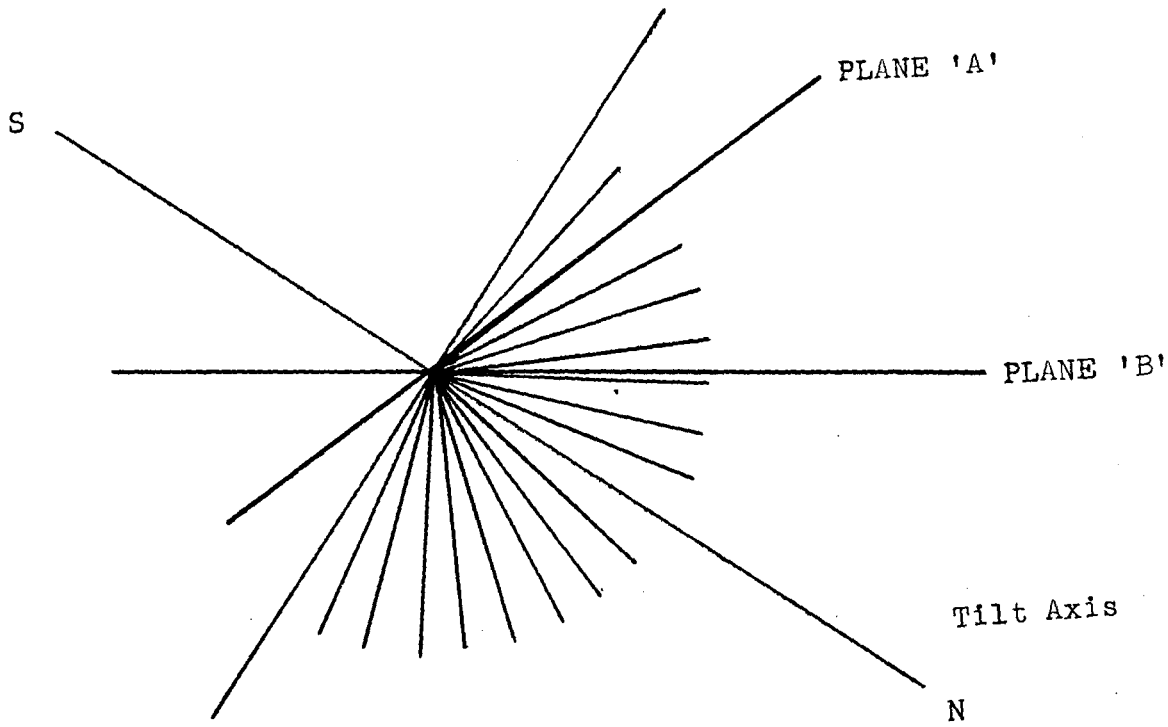

Figure C2 TEM protractor viewing screen indicating slip plane orientation with respect to the North-South axis. Note that there was a rotation between the bright field and the diffraction images.

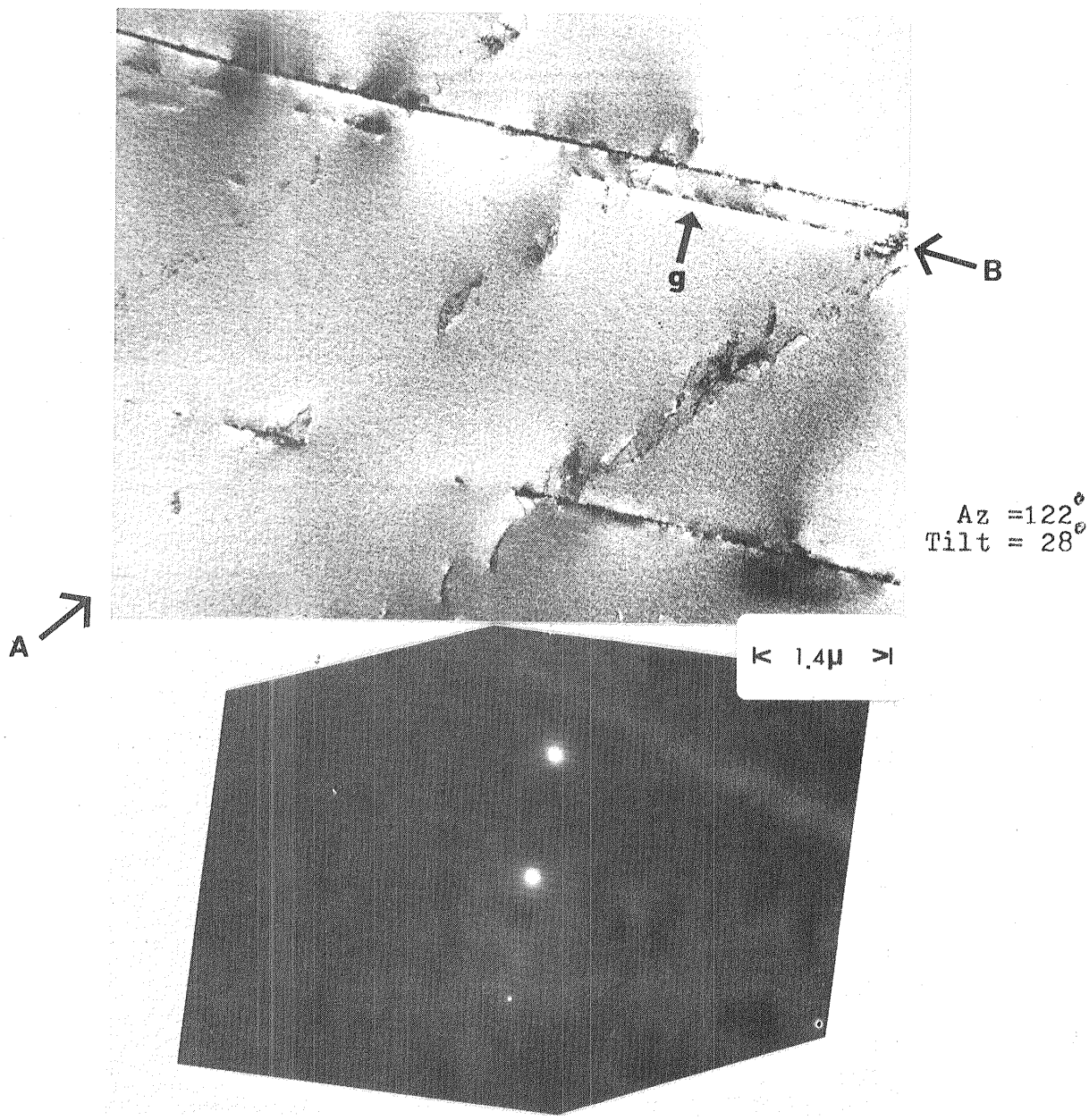

Figure c3a Coarse grained small γ' specimen #5 tested at room temperature($\Delta\varepsilon_p$= 0.06%). Plane 'B' is in the near edge condition. ($\bar{1}11$) g-vector is perpendicular to plane 'B' as indicated by the diffraction pattern. Figures c3a - c3d indicate band widening as the specimen is tilted. g-vectors are not perpendicular at other tilts. Figure c3d shows plane 'A' in near edge character. In this position, plane 'B' is the widest.

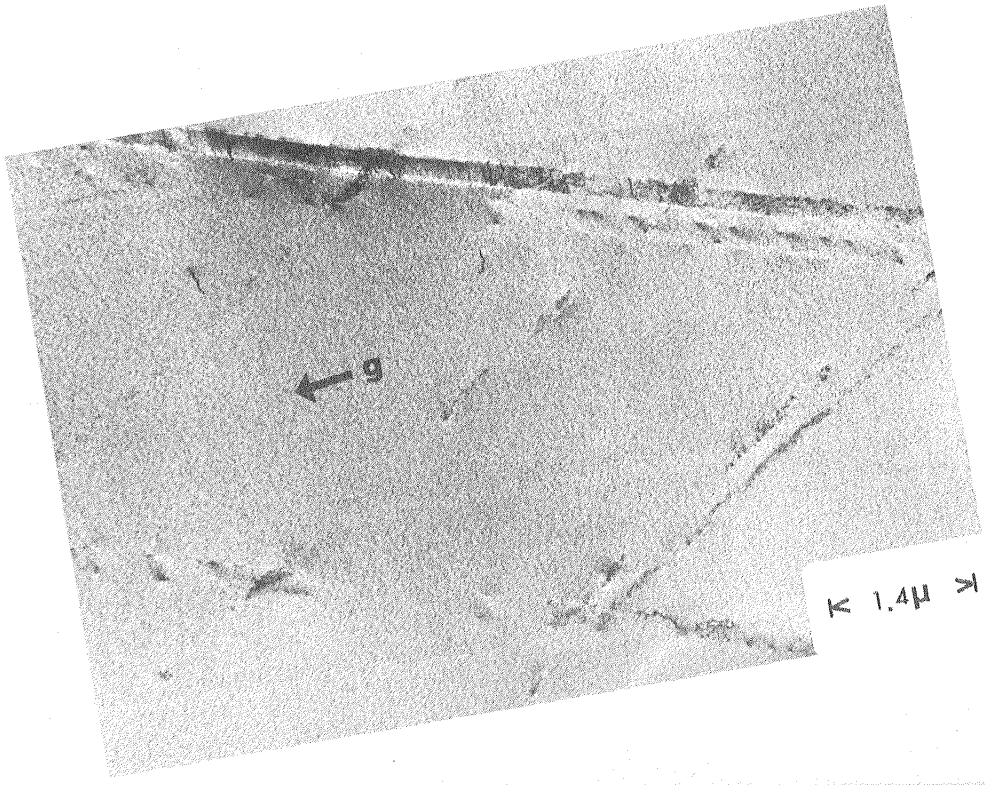

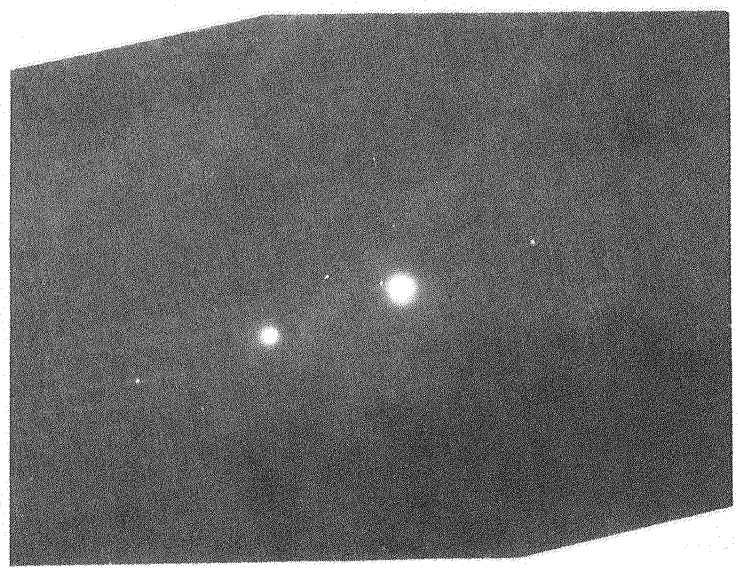

Figure c3b

$g = 1\bar{1}1$

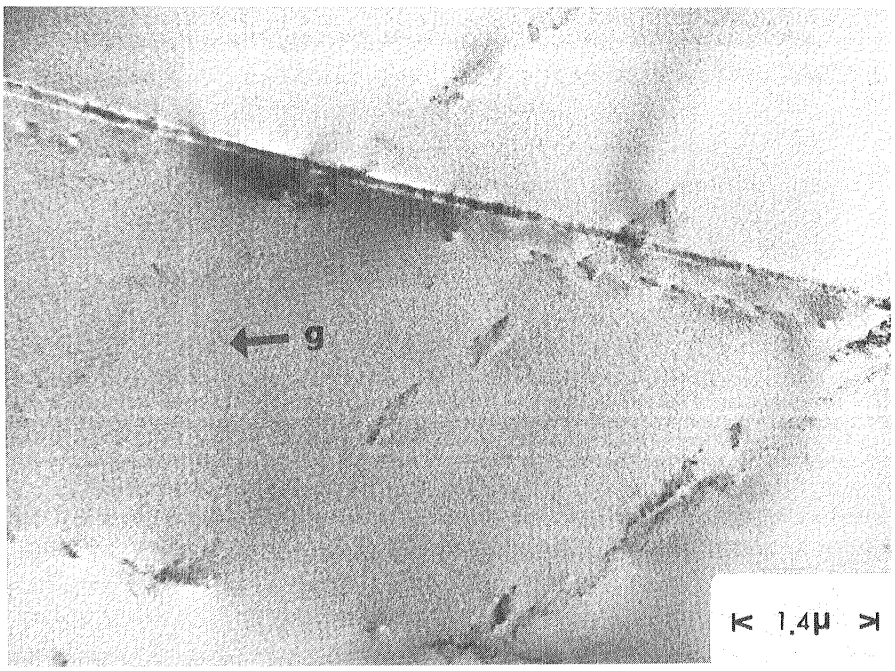

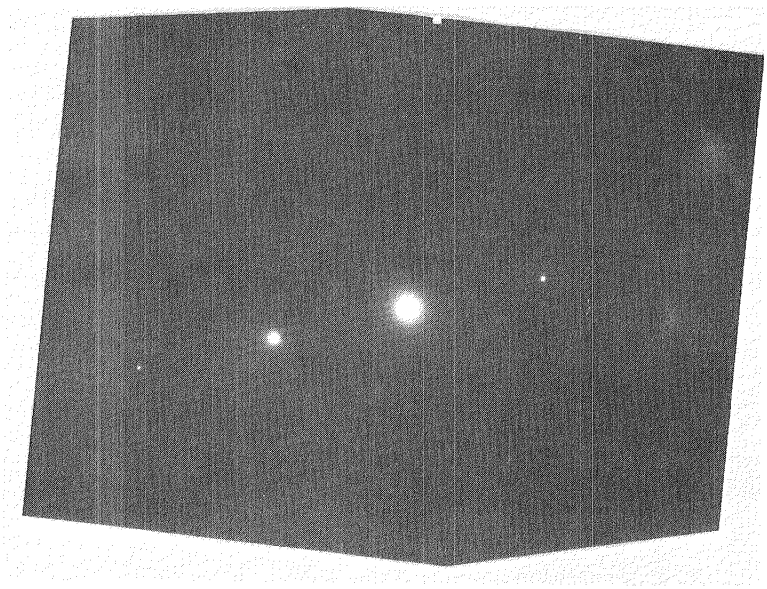

Figure c3c

$g = \bar{1}\bar{1}1$

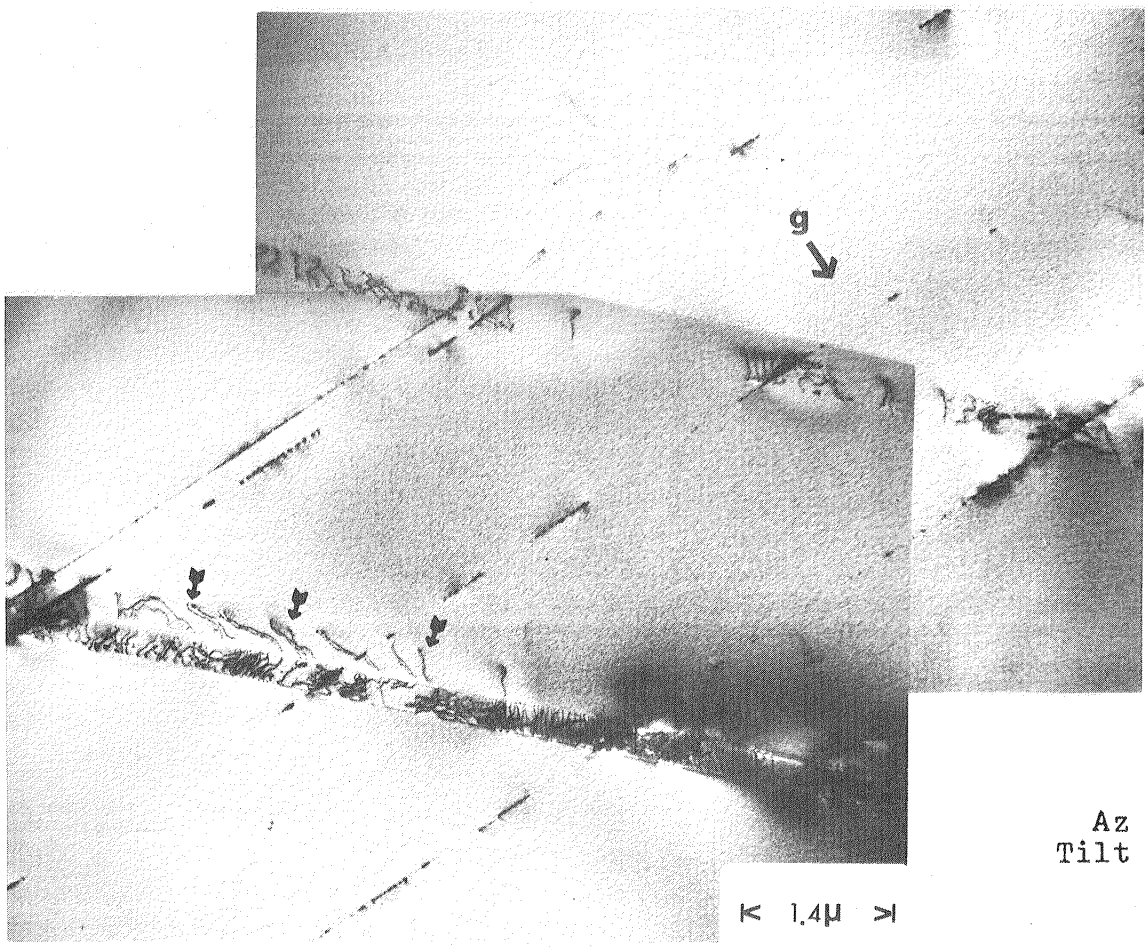

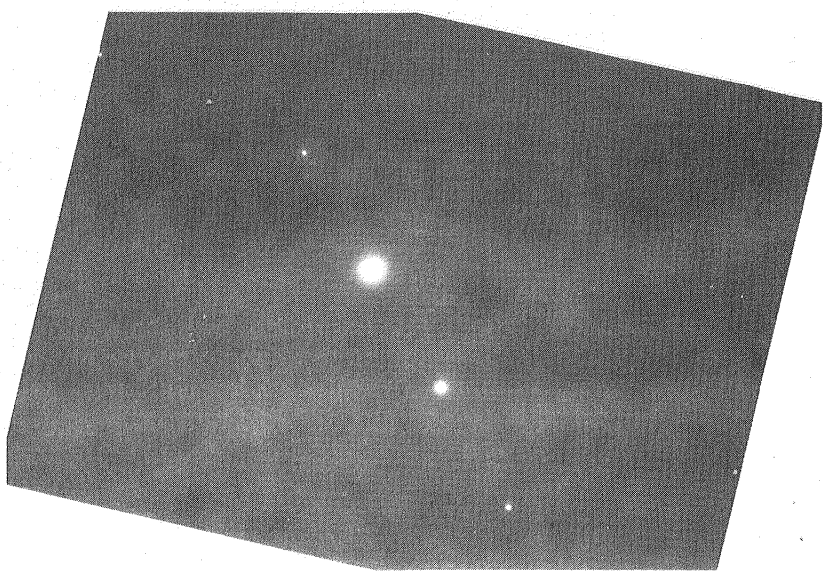

Figure c3d Arrows indicate dislocation pairs.

$g = 11\bar{1}$

APPENDIX D

THERMOCOUPLE CALIBRATION

Two gauges of Chromel-Alumel thermocouple wire were used for this thesis. Both were calibrated by running heating and cooling curves on various pure metals: Tin (99.995%), Lead (99.95%), and Aluminum (99.995%). The metals were placed in a crucible and melted in a resistance furnace. The top of the crucible was covered with charcoal to prevent oxidation of the metals. Each thermocouple was insulated by Alumina tubes. They were inserted into the molten metal and allowed to air cool. Once solidified, the crucible was re-heated and the melting temperature recorded.

Thermocouple voltage was plotted on a strip chart recorder. To insure accuracy, the chart was calibrated against a potentiometer output. A typical cooling curve is given in Fig. D1. The constant temperature region (the horizontal portion of the curve) indicates the freezing point of the metal. Once solidification was complete, the slope changed and the temperature continued to drop. Some supercooling (arrow) is observed prior to solidification. The melting and freezing temperatures are given in Table DI. Comparison with the actual temperatures indicates the temperature differential to be acceptable within the measuring capabilities of the equipment. Errors may have been introduced by the reported purities of the metals, and by the "actual" melting temperatures of the metals. The 30

gauge wire was not calibrated against Al due to the severe attack that the molten Al had on the wire and on the Alumina insulators.

TABLE DI

THERMOCOUPLE CALIBRATION

PURE METAL	MEASURED TEMP. (C)	ACTUAL[73] TEMP. (C)	TEMPERATURE DIFFERENTIAL (C)
		24 Gauge	
Sn	234.0		2.03
	(231.5)	231.97	-0.47
Pb	331.0		3.50
	(331.0)	327.50	3.50
Al	667.0		6.63
	(661.0)		0.63
	667.0	660.37	6.63
	(661.0)		0.63
		30 Gauge	
Sn	229.0		-2.97
	(230.0)	231.97	-1.97
Pb	327.0		-0.50
	(324.0)	327.50	-3.50

NOTE: Values in parenthesis are the melting temperatures. The other values are freezing temperatures.

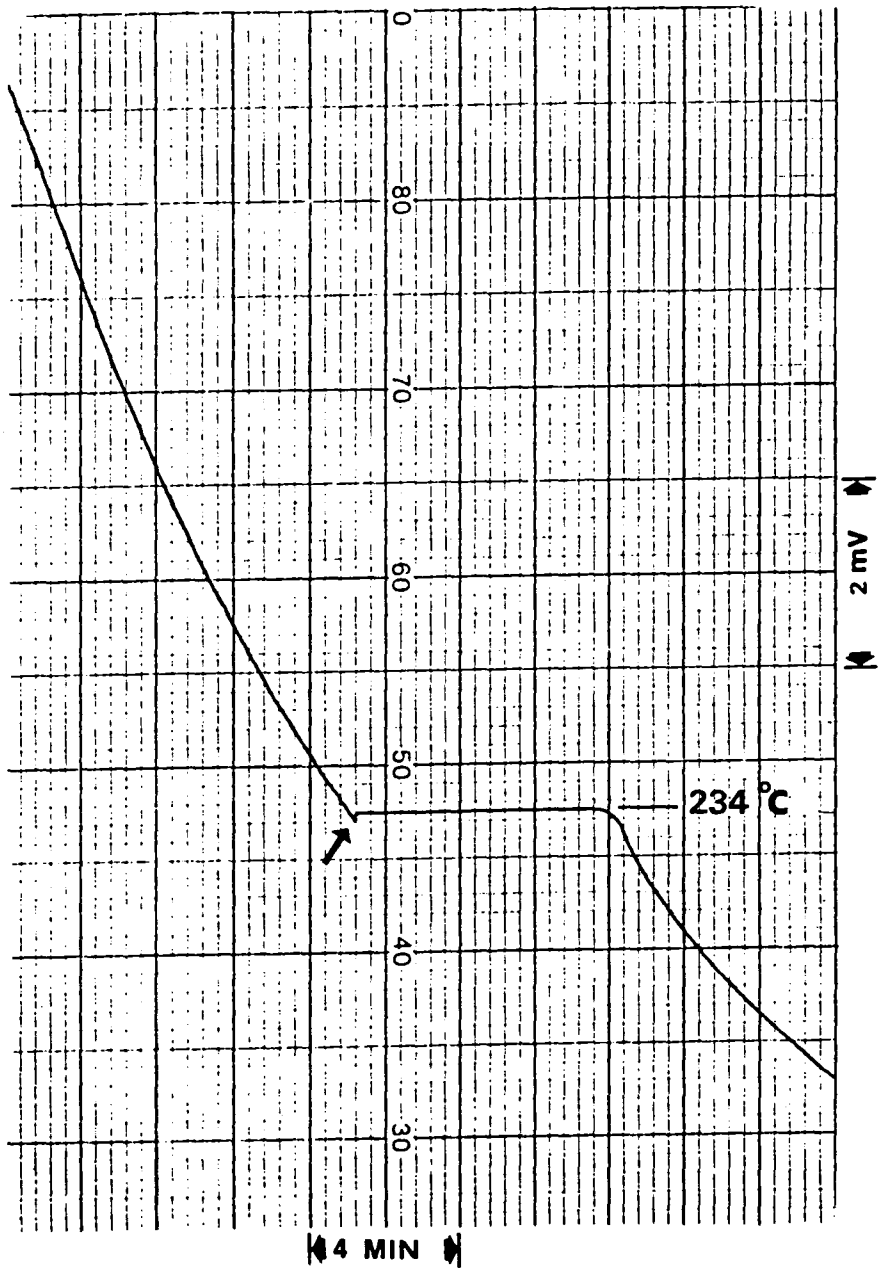

Figure D1 Cooling curve of Tin for calibration of 24 gauge Chromel-Alumel thermocouple wire. Arrow indicates supercooling before solidification.

TABLE I

COMPOSITION OF WASPALOY PLATE

Ni	56.80
Cr	19.18
Co	13.93
Mo	4.40
Ti	2.98
Al	1.31
Fe	1.17
Zr	0.076
Si	0.06
C	0.045
Mn	0.03
B	0.006
S	0.004
P	0.004

NOTE: This analysis has been furnished by Universal Cyclops Speciality Steel Division.

TABLE II

Microstructural Analysis

	Heat Treatment	Grain Size	γ' Size	Boundary Carbides	Matrix Carbides
A.	1010°C(1850°F)/2 Hrs OQ + 875°C (1607°F)/24 Hrs OQ	ASTM 9 16μ m Dia.	3000 Å + 900 Å	Discrete Particles of $M_{23}C_6$	Numerous large particles significant increase in size and distribution over treatment B.
B.	1010°C(1850°F)/2 Hrs OQ + 730°C (1346°F)/6 Hrs OQ	ASTM 9 16μ m	1500 Å + 50-80 Å	Discrete Particles of $M_{23}C_6$	A few particles
E.	1100°C(2012°F)/2 Hrs OQ + 875°C (1607°F)/24 Hrs OQ	ASTM 3 125μ m	1300 Å	Continuous films and plate-like $M_{23}C_6$ on some twin and grain boundaries	Largest size and distribution of particles
F.	1100°C(2012°F)/2 Hrs OQ + 730°C (1346°F)/6 Hrs OQ	ASTM 3 125μ m	50-80 Å	No boundary carbides	Similar to treatment A

TABLE III

ROOM TEMPERATURE TENSILE PROPERTIES [1]

HEAT TREATMENT	MICRO-STRUCTURE	0.2% YIELD STRENGTH Ksi(MPa)	ULTIMATE TENSILE STRENGTH Ksi(MPa)	PERCENT REDUCTION IN AREA	TRUE FRACTURE STRAIN	STRAIN HARDENING EXPONENT
A	Fine G/S	113(778)	229(1581)	45.6	0.61	0.32
	Large γ'	110(760)	227(1562)	45.6	0.61	0.32
F	Coarse G/S	96(664)	231(1593)	51.5	0.72	0.36
	Small γ'	94(649)	230(1587)	54.0	0.78	0.36

MONOTONIC STRESS-STRAIN RELATIONSHIPS

Heat Treatment	Equation (σ in Ksi)
A	$\sigma = 358 (\varepsilon)^{0.32}$
F	$\sigma = 304 (\varepsilon)^{0.36}$

TABLE IV

LCF DATA (25°C)

Spec #	$\Delta\varepsilon_T$ %	$\Delta\varepsilon_e$ %	$\Delta\varepsilon_p$ %	N_f	σ_T (psi) @ $N_f/2$	σ_C (psi) @ $N_f/2$	t_f (Min)
			GRAIN SIZE 9				
N_i4	1.49	0.49	1.00	3174	128,133	132,781	158.7
4^1	0.97	0.63	0.34	10500	101,996	126,747	525.0
2^1	0.94	0.61	0.34	10700	106,925	112,016	535.0
8^3	0.84	0.70	0.24	12911	98,523	98,447	430.4
11^3	0.72	0.57	0.15	25208	96,275	114,178	840.3
N_i1	0.49	0.37	0.12	68020	100,647	99,636	3401.0
10^3	0.59	0.52	0.07	29225	80,800	80,790	974.2
12^3	0.53	0.47	0.06	135527	79,450	79,450	4517.6
$9^{2,3}$	0.37	0.34	0.03	196425	60,164	70,431	6547.5
			GRAIN SIZE 3				
N_i3	5.73	2.73	3.00	740	128,947	134,040	37.0
3^1	1.39	0.45	0.94	3150	103,828	106,434	157.5

GRAIN SIZE 3 (Con't)

Spec #	$\Delta\varepsilon_t$%	$\Delta\varepsilon_e$%	$\Delta\varepsilon_p$%	N_f	σ_τ (psi) @ $\tau N_f/2$	σ_c (psi) @ $cN_f/2$	τ_f (Min)
5[1]	0.81	0.48	0.34	11100	88,554	98,795	555.0
4[3]	0.75	0.45	0.30	12847	88,978	89,379	428.2
N_i[2]	0.45	0.30	0.15	41924	72,555	97,817	2096.2
5[3]	0.47	0.41	0.06	42472	72,745	71,544	1415.7

1) Tested by Martin[70]
2) Specimen Run-Out at 196,425 cycles
3) Specimens tested at 0.5Hz. All others at 0.33 Hz.

TABLE V

SUMMARY OF VARIOUS WASPALOY MICROSTRUCTURES AND COMPOSITIONS

COMPOSITION (wt%)										
Ni	Cr	Co	Mo	Ti	Al	Fe	C	Si	Mn	
56.00	19.00	14.00	4.30	3.00	1.30	1.00	0.07	0.40	0.70	Morrow[47]
58.74	18.70	14.21	3.86	2.99	1.44	*	0.06	*	*	Clavel[22]
56.80	19.18	13.93	4.40	2.98	1.31	1.17	0.05	0.06	0.03	Lerch

HEAT TREATMENT		Expected Microstructure	
		ASTM Grain Size	γ' Dia. (Å)
Morrow[47] et al.			
A	1080-1090°C/4 Hrs AQ + 850 C/2-4 Hrs FC to 760 C/16 Hrs FC	2-4	200+500-1000
B	996-1010 C/4 Hrs OQ + 850 C/2-4 Hrs FC to 760 C/16 Hrs AC	9	200+500-1000+ 1000
Clavel[22] et al.			
	1010 C/4 Hrs OQ + 850 C/4 Hrs AC + 760 C/16 Hrs AC	4	400 + 2000
Lerch			
A	1010 C/2 Hrs OQ + 875 C/24 Hrs OQ	9	900 + 3000
F	1100 C/2 Hrs OQ + 730 C/6 Hrs OQ	3	50 - 80

* Not reported
AQ = AC = air cool FC = furnace cool OQ = oil quench

TABLE VI

COFFIN-MANSON SLOPES

	GRAIN SIZE 9	GRAIN SIZE 3
n'	0.19	0.15
α	1.05	1.00
β	0.76	0.86
β^1	0.52	0.58
β^2	0.73	0.77
β^3	0.80	0.87

β = Measured

β^1 = Calculated from[49] $1/(1 + 5n')$

β^2 = Calculated from[50] $1/(1 + 2n')$

β^3 = Calculated from[2] $1/(1 + n')\alpha$

TABLE VII

CALCULATED LOAD DROP FOR VARIOUS CRACK SIZES

Crack Size (μ)[1] 2C	a	Cracked Area (In^2)	Load Drop (lbs)[2]	Distance Dropped[3] On Strip Chart (Mils)	(mm)
100	50	6.1×10^{-6}	0.6	0.3	0.008
250	175	7.5×10^{-5}	7.4	3.7	0.094
450	225	1.2×10^{-4}	12.1	6.1	0.154
500	250	1.5×10^{-4}	14.7	7.4	0.187
800	400	3.9×10^{-4}	38.2	19.1	0.485
1000	500	6.1×10^{-4}	59.8	29.9	0.759
1500	750	1.4×10^{-3}	134.1	67.1	1.704
2000	1000	2.4×10^{-3}	235.2	117.6	2.987

1 Assumes Elliptical Crack having minor axis (a) half of the major axis (2C)

2 Load Drop calculated using a saturation stress (σ_s) of 98,000 psi (i.e. $\Delta\epsilon_\rho \cong 0.12\%$). Load drop = σ_s X (Cracked area)

3 Calculated for a strip chart scale of 2000 lbs./in.

TABLE VIII

ELEVATED TEMPERATURE LCF DATA

Spec #	Temp (°C)	$\Delta\varepsilon_t$%	$\Delta\varepsilon_e$%	$\Delta\varepsilon_p$%	N_f	σ_T(psi) @ $N_f/2$	σ_T(psi) @ $N_f/2$	t_f(Min.)[1]
				GRAIN SIZE 9				
21	500	0.95	0.65	0.30	5806	92,225	96,143	277.1
22	800	0.77	0.47	0.30	1080	58,540	61,347	54.0
				GRAIN SIZE 3				
20	500	0.85	0.55	0.30	6000	97,536	101,643	300.0
24	700	0.69	0.39	0.30	4970	52,174	50,310	248.5
23	800	0.68	0.38	0.30	1095	51,524	51,925	54.8
25	800	0.69	0.39	0.30	1587	51,132	51,940	79.4

1 Test frequency was 0.33 Hz.

TABLE IX

THE EFFECTS OF TEMPERATURE ON THE ELASTIC MODULUS*

TEMP (°C)	25	500	600	700	800
GRAIN SIZE					
3	34.1×10^6 (2.35×10^5)	25.7×10^6 (1.77×10^5)		22.8×10^6 (1.57×10^5)	20.7×10^6 (1.43×10^5)
	31.7×10^6 (2.19×10^5)	26.4×10^6 (1.82×10^5)			22.7×10^6 (1.57×10^5)
7**	29.2×10^6 (2.01×10^5)		25.4×10^6 (1.75×10^5)	23.5×10^6 (1.62×10^5)	21.6×10^6 (1.49×10^5)
9	28.2×10^6 (1.97×10^5)	24.5×10^6 (1.69×10^5)			18.5×10^6 (1.28×10^5)
	33.0×10^6 (2.28×10^5)				

* Values in psi (MPa)

** Values from CEAT[59]

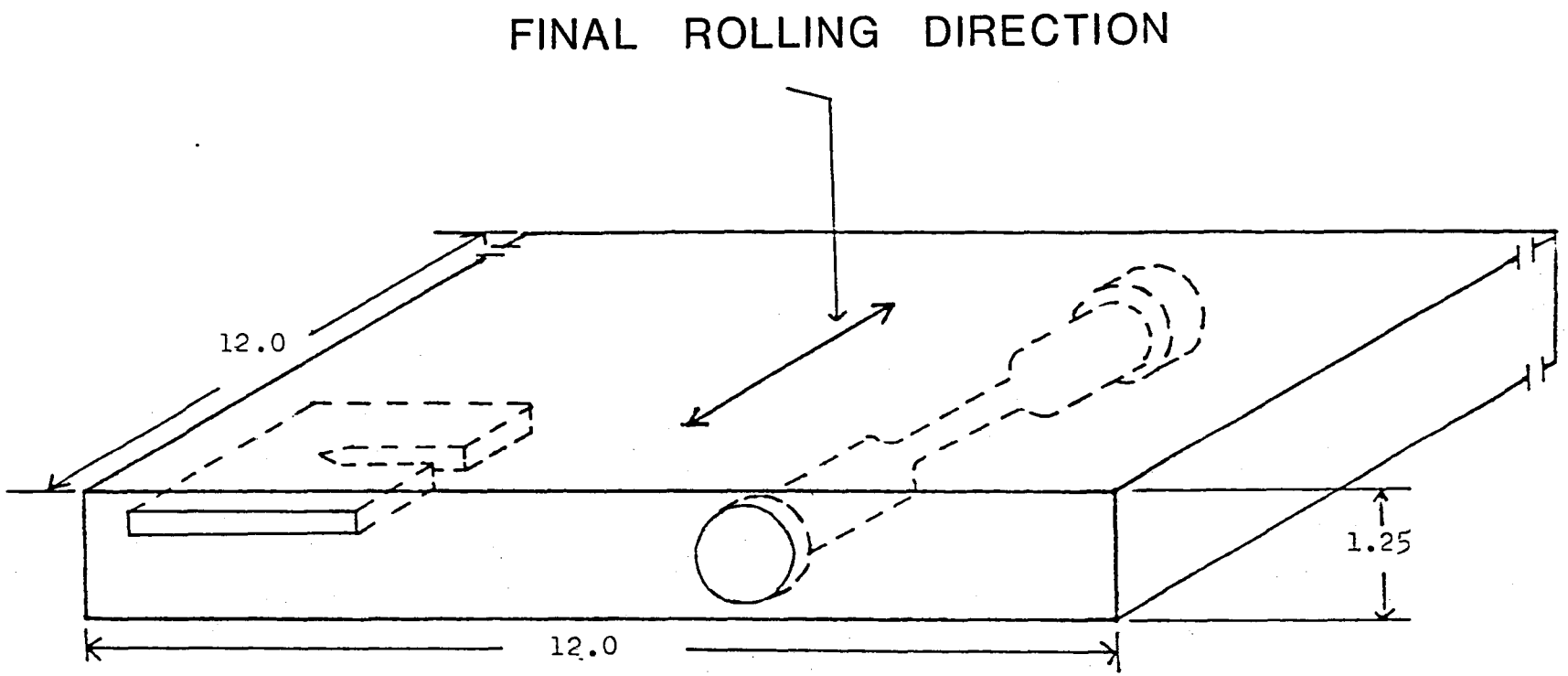

Figure 1 The Waspaloy billet indicating the positions of FCP(Lawless)[1] and LCF specimens. Note that the LCF specimens were machined with the stress axis parallel to the final rolling direction.

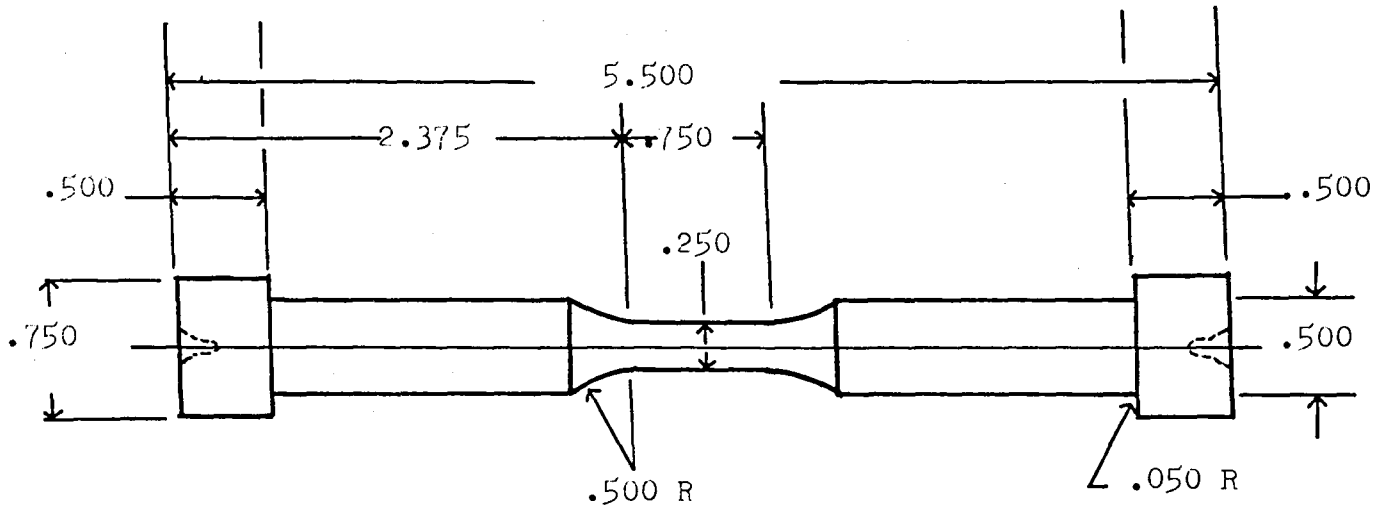

Figure 2 Solid longitudinal LCF specimen configuration.
(All dimensions are in inches)

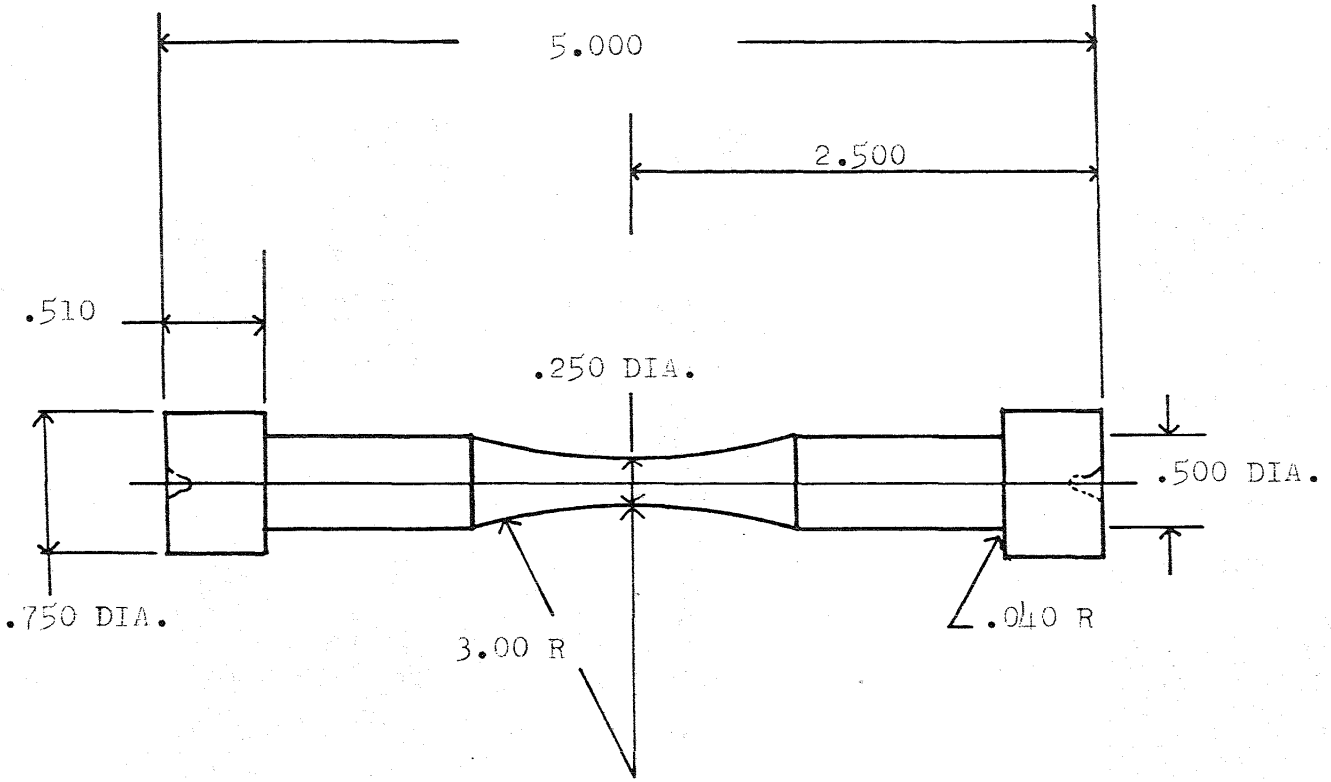

Figure 3 Hour-glass LCF specimen configuration.
(All dimensions are in inches)

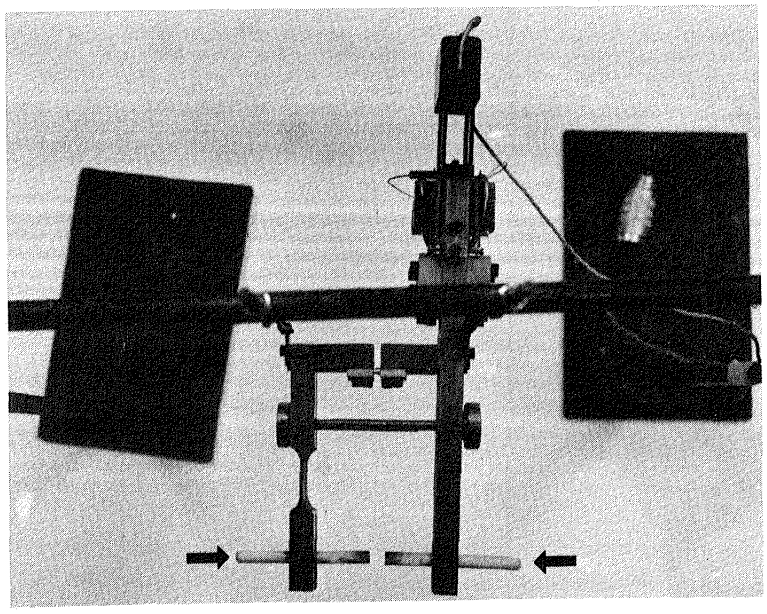

(a)

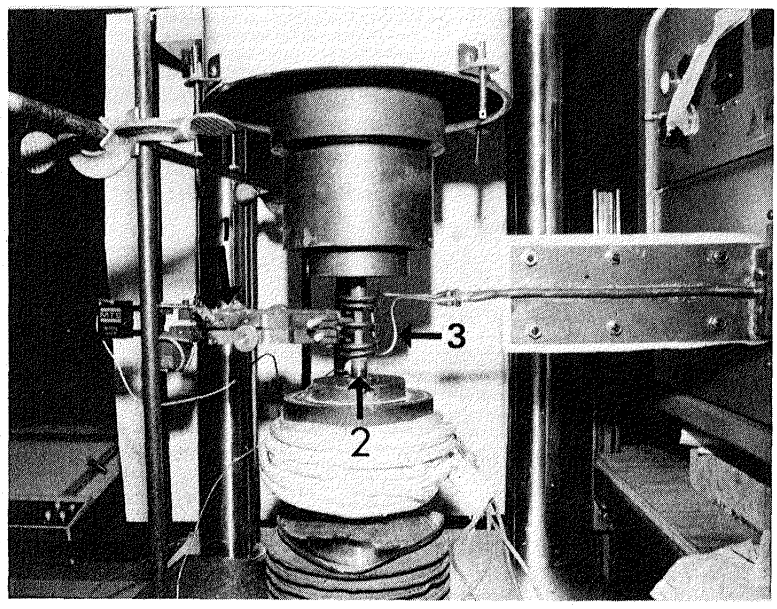

(b)

Figure 4 a) Top view of the extensometer used for measuring longitudinal displacements. Four ceramic probes (arrows) clamp onto the specimen's gauge. b) High temperature test arrangement. Arrow 1 indicates the extensometer. Arrow 2 indicates the LCF specimen. Arrow 3 indicates the copper induction coil.

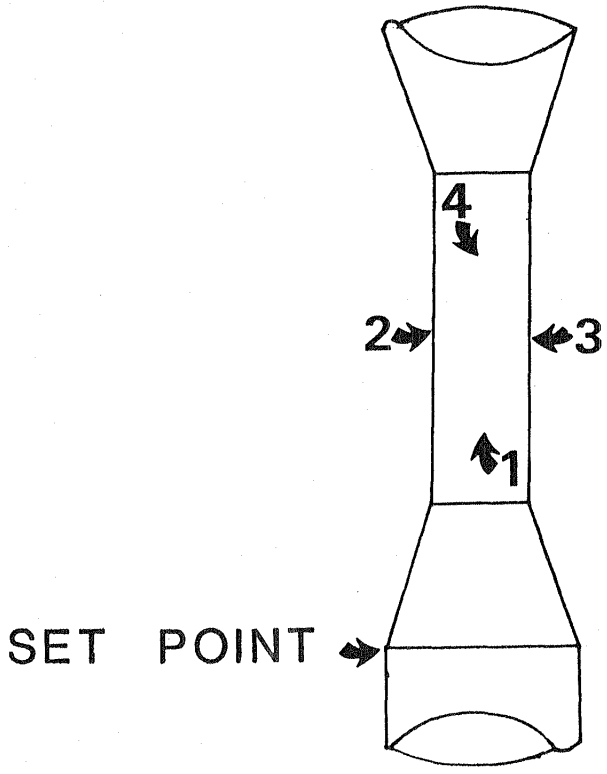

(a)

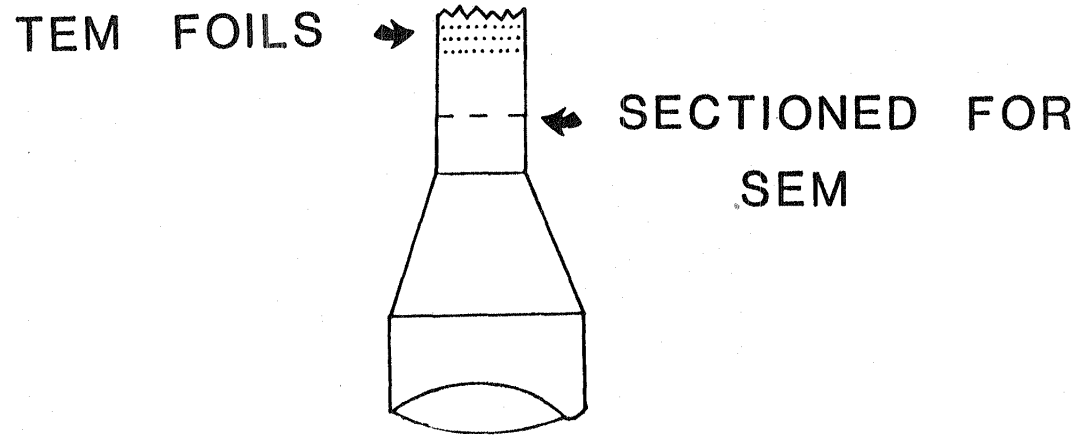

(b)

Figure 5 a) Schematic of the thermocouple positions for test temperature calibration. Set point(at the specimen's shoulder) indicates thermocouple position during testing. b) orientation of specimens for SEM and TEM(foils) examination.

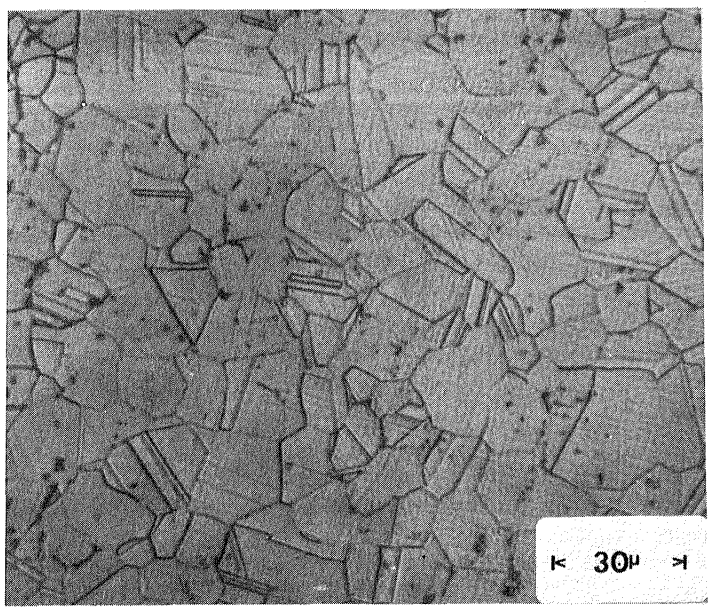

(a)

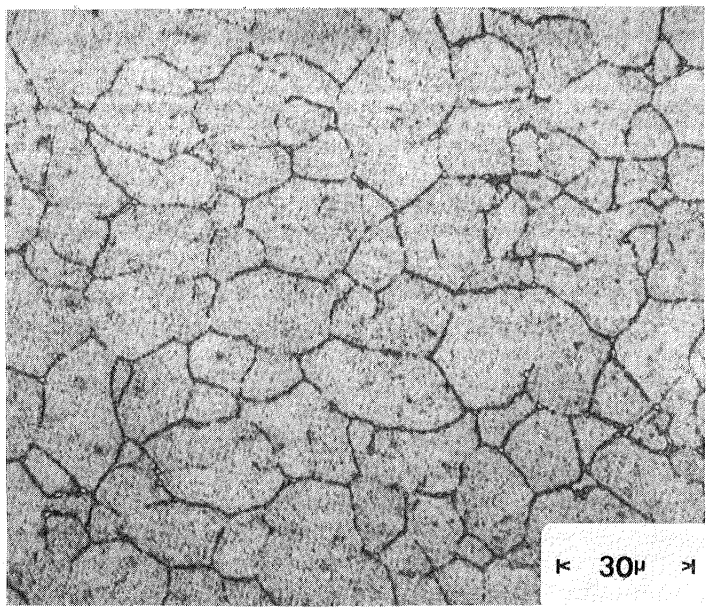

(b)

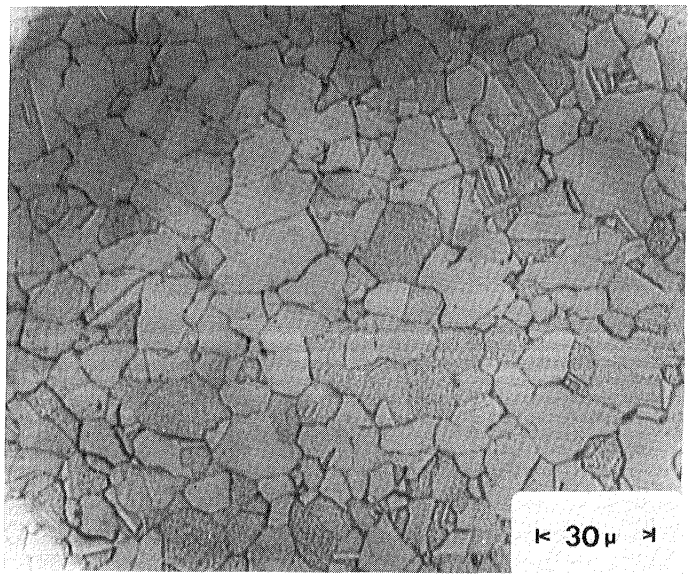

(c)

Figure 6 Optical micrographs of the fine grained specimens. a) Small γ' b) Large γ' c) As-received billet. All photos taken on the rolling face.

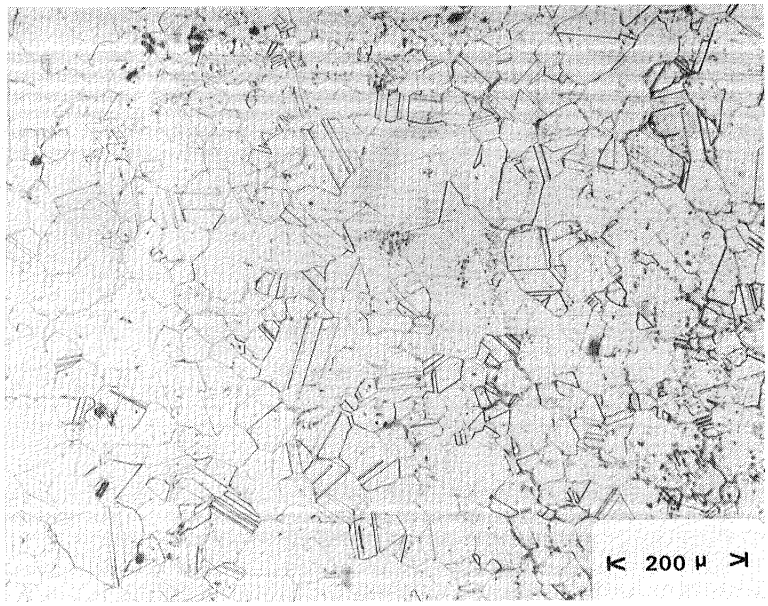

(a)

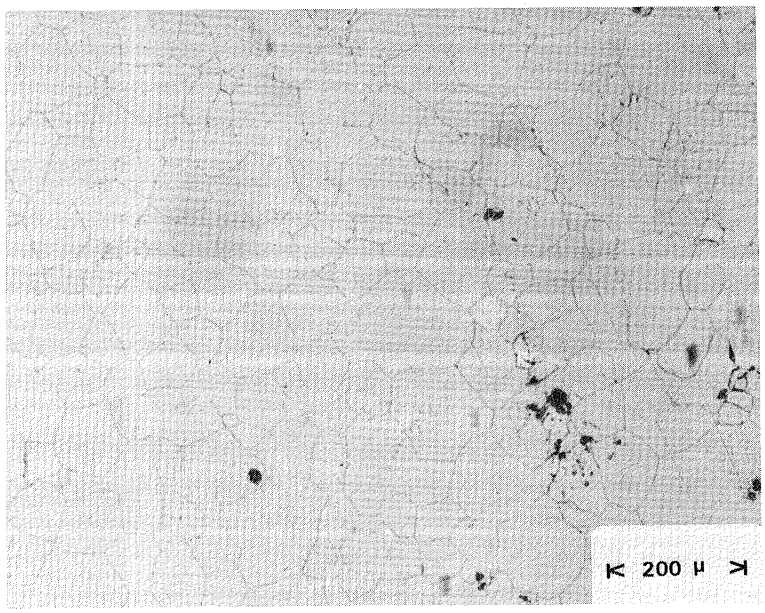

(b)

Figure 7 Optical micrographs of the coarse grained specimens. a) Small γ' b) Large γ'. Photos taken on the rolling plane.

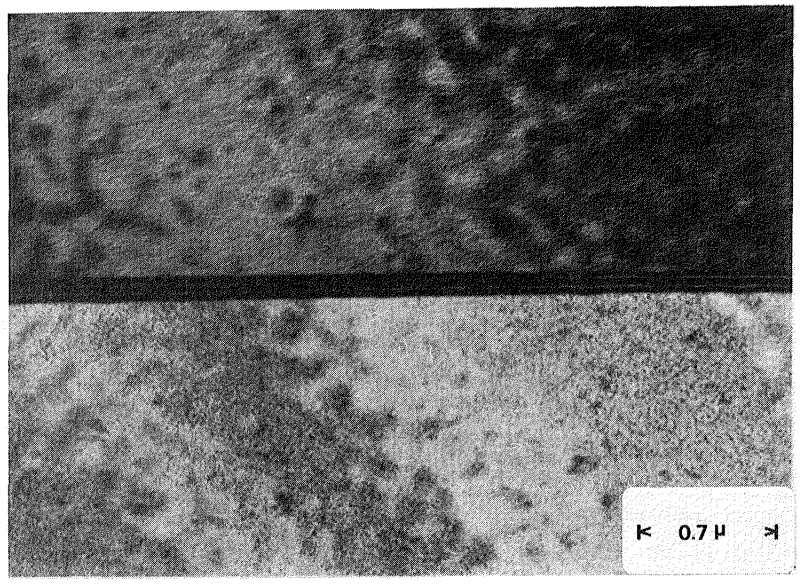

(a)

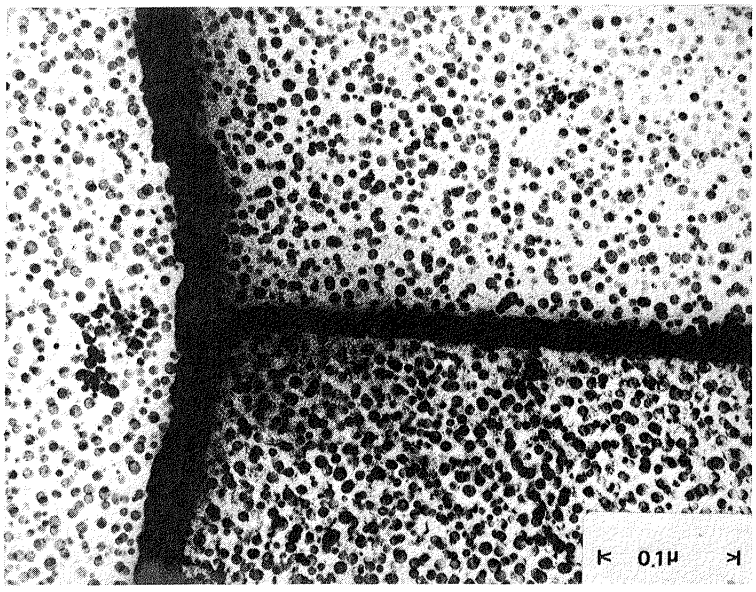

(b)

Figure 8 TEM micrographs of the boundary morphologies of the coarse grained specimens. a) Small γ' material. Straight boundary containing no carbides. b) Large γ' material showing a continuous $M_{23}C_6$ carbide film.

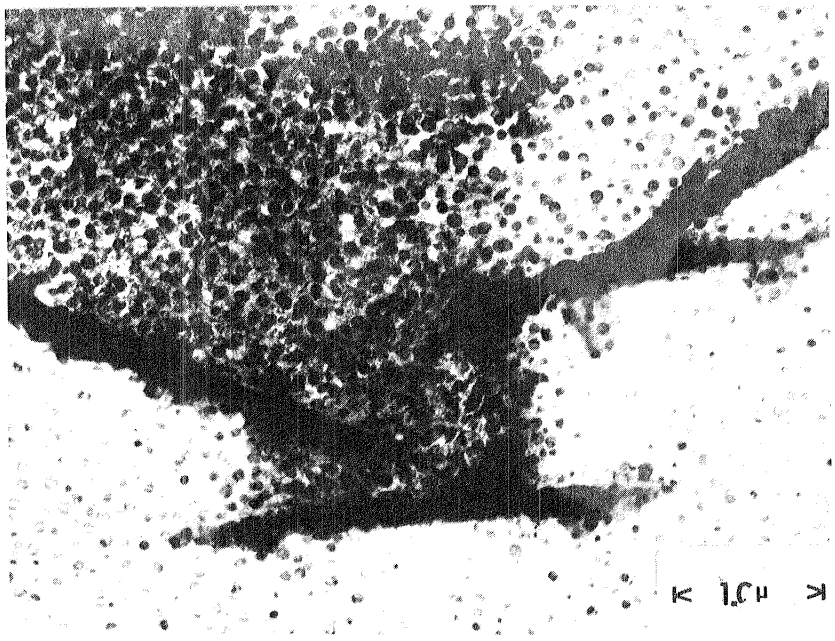

(a)

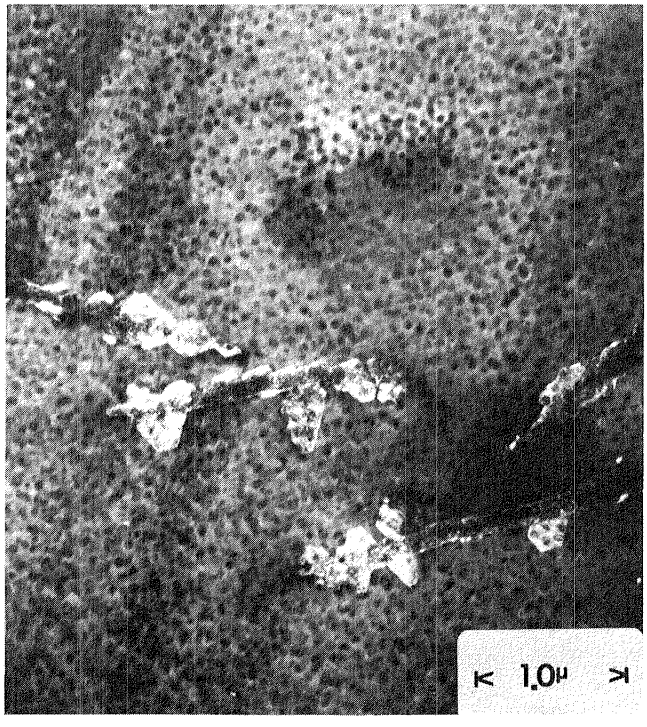

(b)

Figure 9 Plate-like $M_{23}C_6$ carbides observed at some twin and grain boundaries of the coarse grained large γ' specimen. a) Bright field b) Dark field.

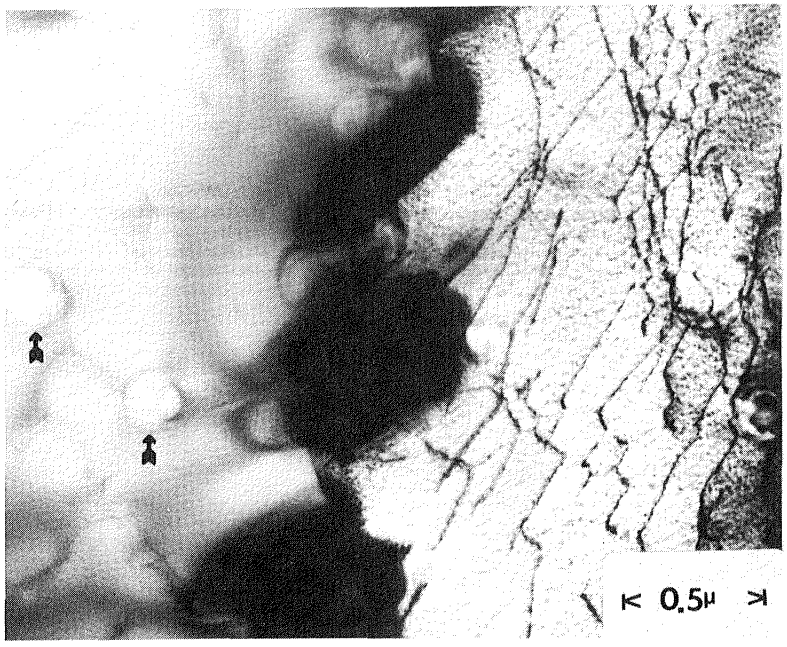

(a)

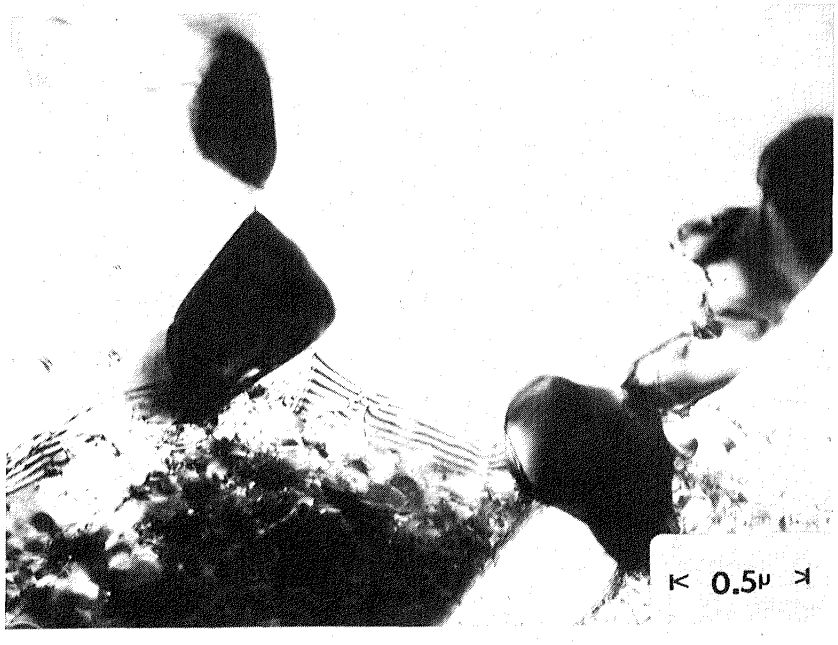

(b)

Figure 10 TEM micrographs of the boundary morphologies of the fine grained specimens. a) Small γ' material showing discrete boundary carbides. Arrows indicate some unsolutioned γ' in the matrix. b) Large γ' material showing discrete boundary carbides.

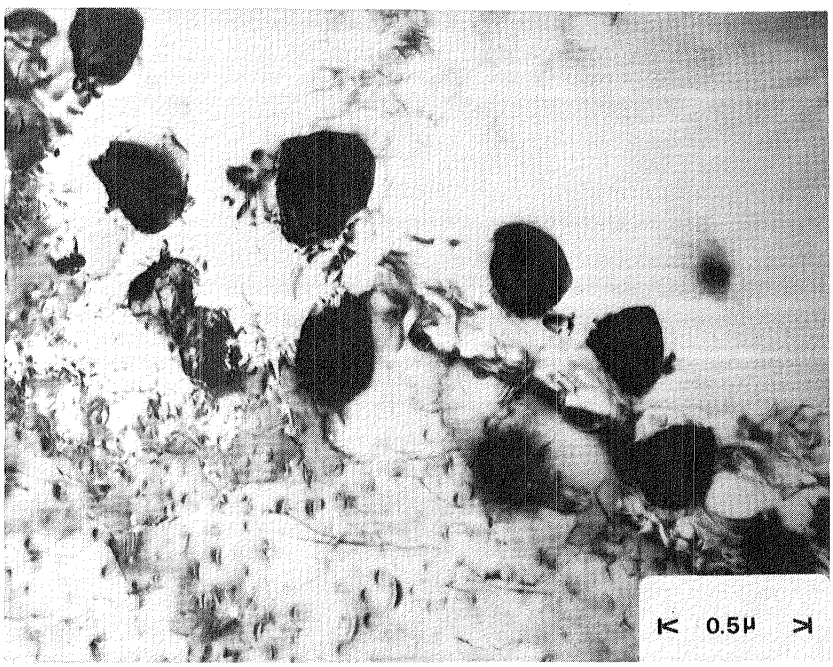

Figure 11 A typical grain boundary in the fine grained large γ' material. There are many $M_{23}C_6$ carbides in the vicinity of the boundary.

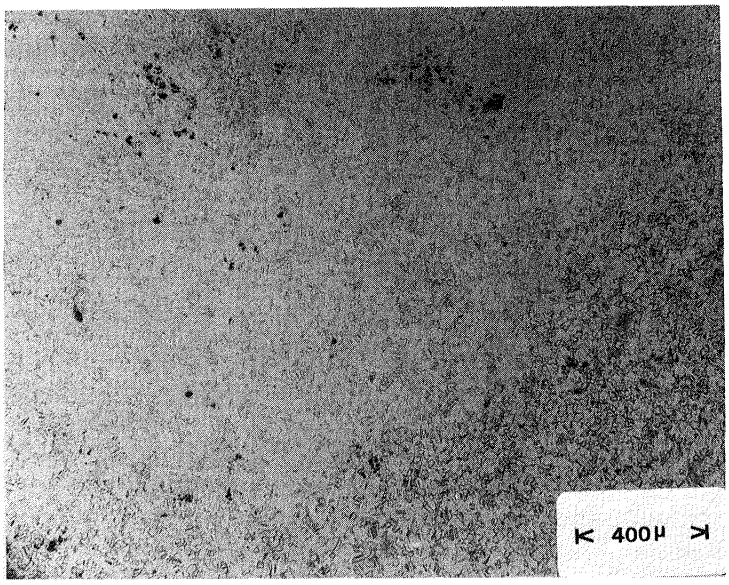

(a)

ROLLING DIRECTION

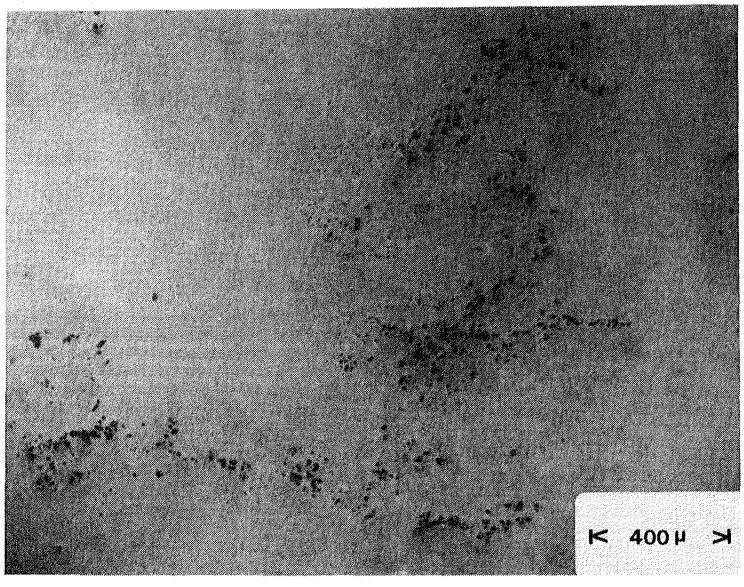

(b)

Figure 12 Matrix carbides of the fine grained specimens a) Small γ' and b) Large γ' taken on the rolling plane. Carbides are generally of the MC type. The large γ' material contains more of these carbides.

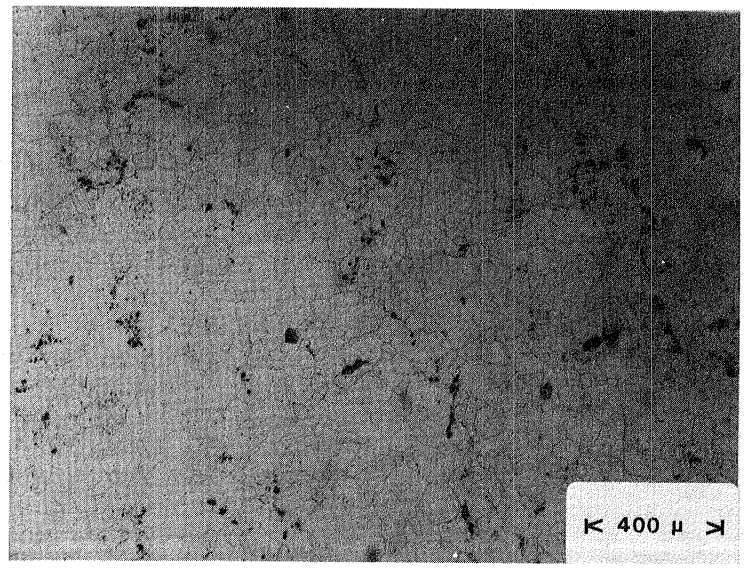

(a)

ROLLING DIRECTION

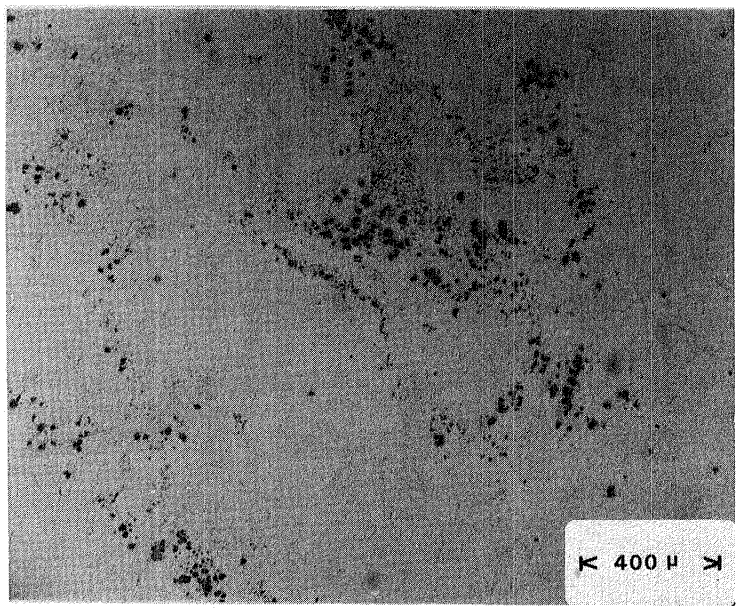

(b)

Figure 13 Matrix carbides of the coarse grained specimens a) Small γ' and b) Large γ' taken on the rolling plane. The large γ' material has both the greatest number and largest size of carbides.

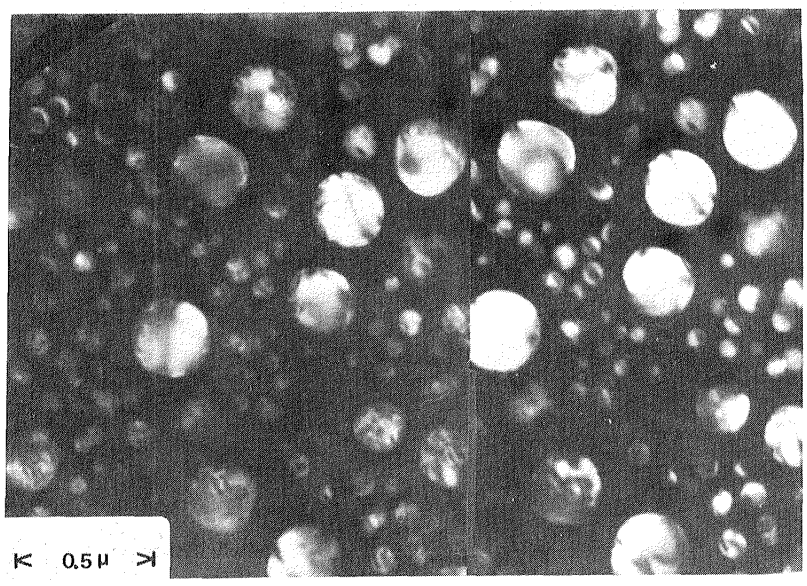

(a)

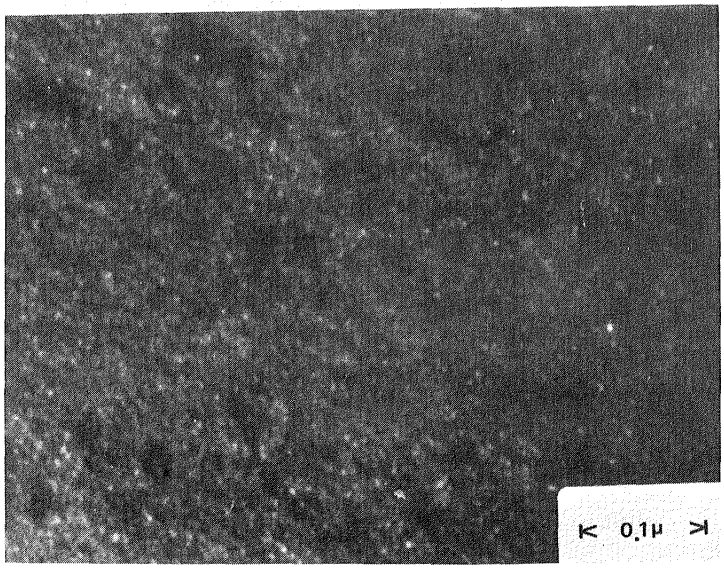

(b)

Figure 14 TEM dark field of the γ' precipitates. a) Stereo pair of γ' in the fine grained large γ' material. γ' diameters are 3000 and 900 A. The large particles represent unsolutioned γ' which constitute about 5% of the total volume fraction as determined by a point intercept count. b) γ' in the coarse grained small γ' material.

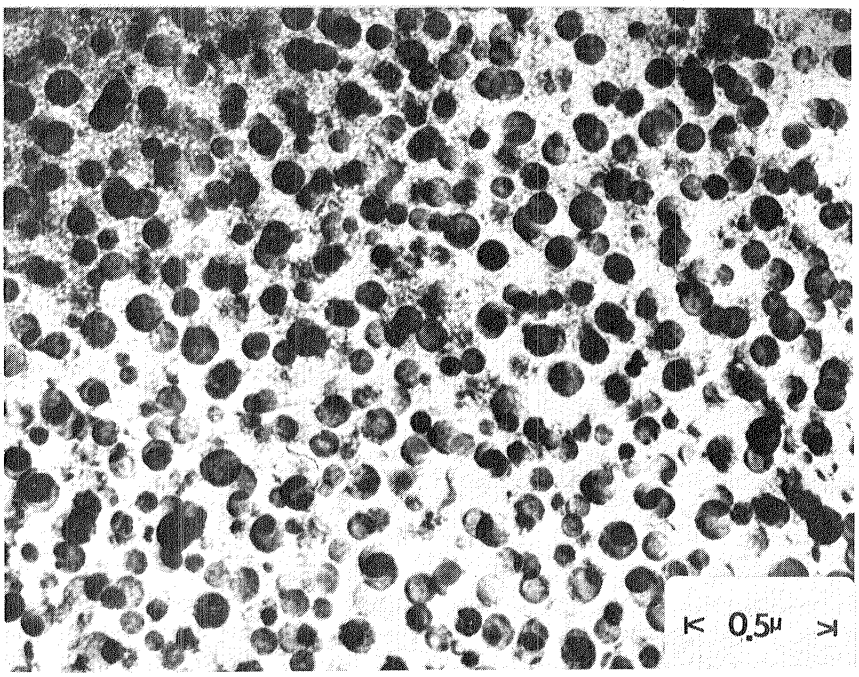

Figure 15 TEM bright field of the γ' precipitates in the coarse grained, large γ' specimens. γ' diameters are 1300Å.

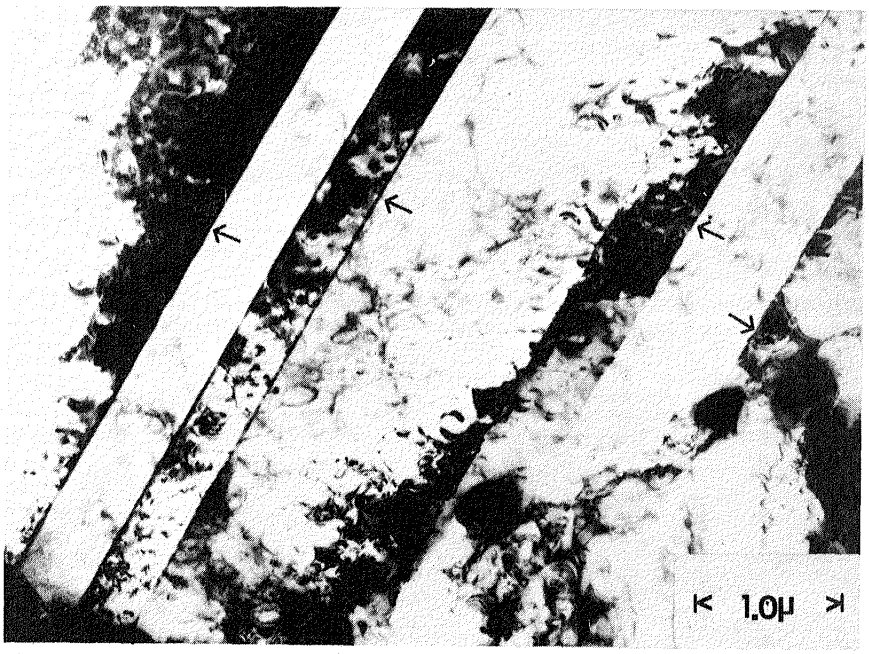

Figure 16 Fine grained large γ' specimen indicating annealing twins(arrows) in a grain.

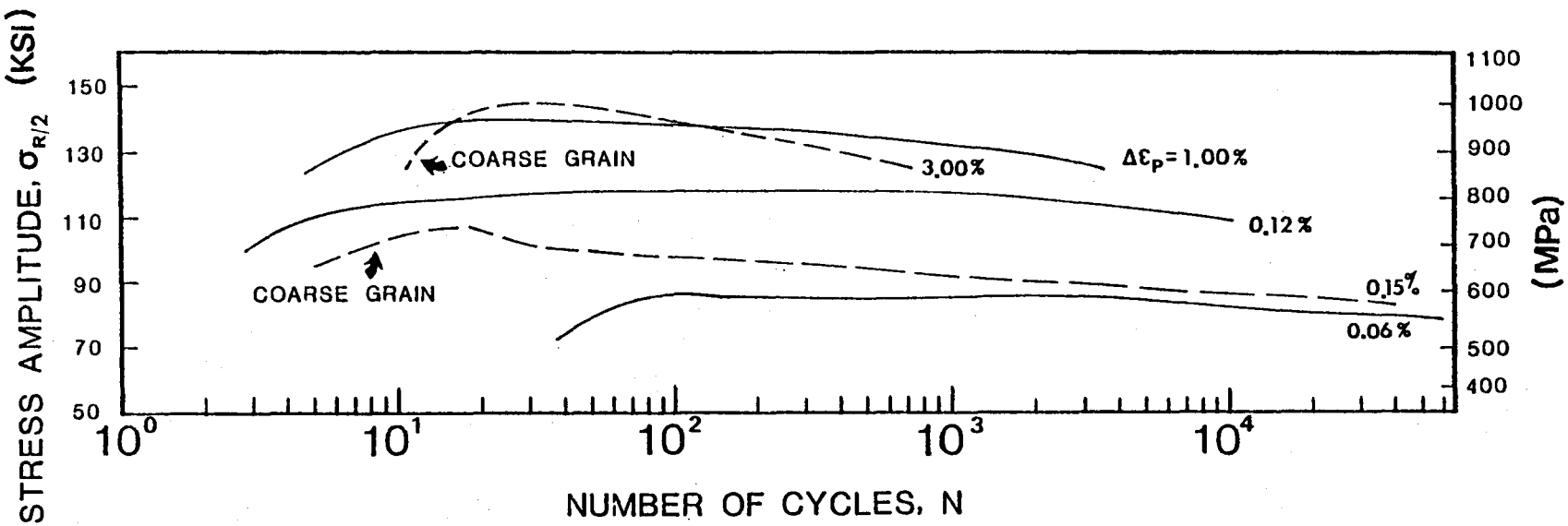

Figure 17 Cumulative glide plots for Waspaloy specimens tested at room temperature. Coarse grained small γ' specimens (dashed lines) harden to a stress maximum and then soften to failure. Fine grained large γ' specimens (solid lines) harden to stress saturation.

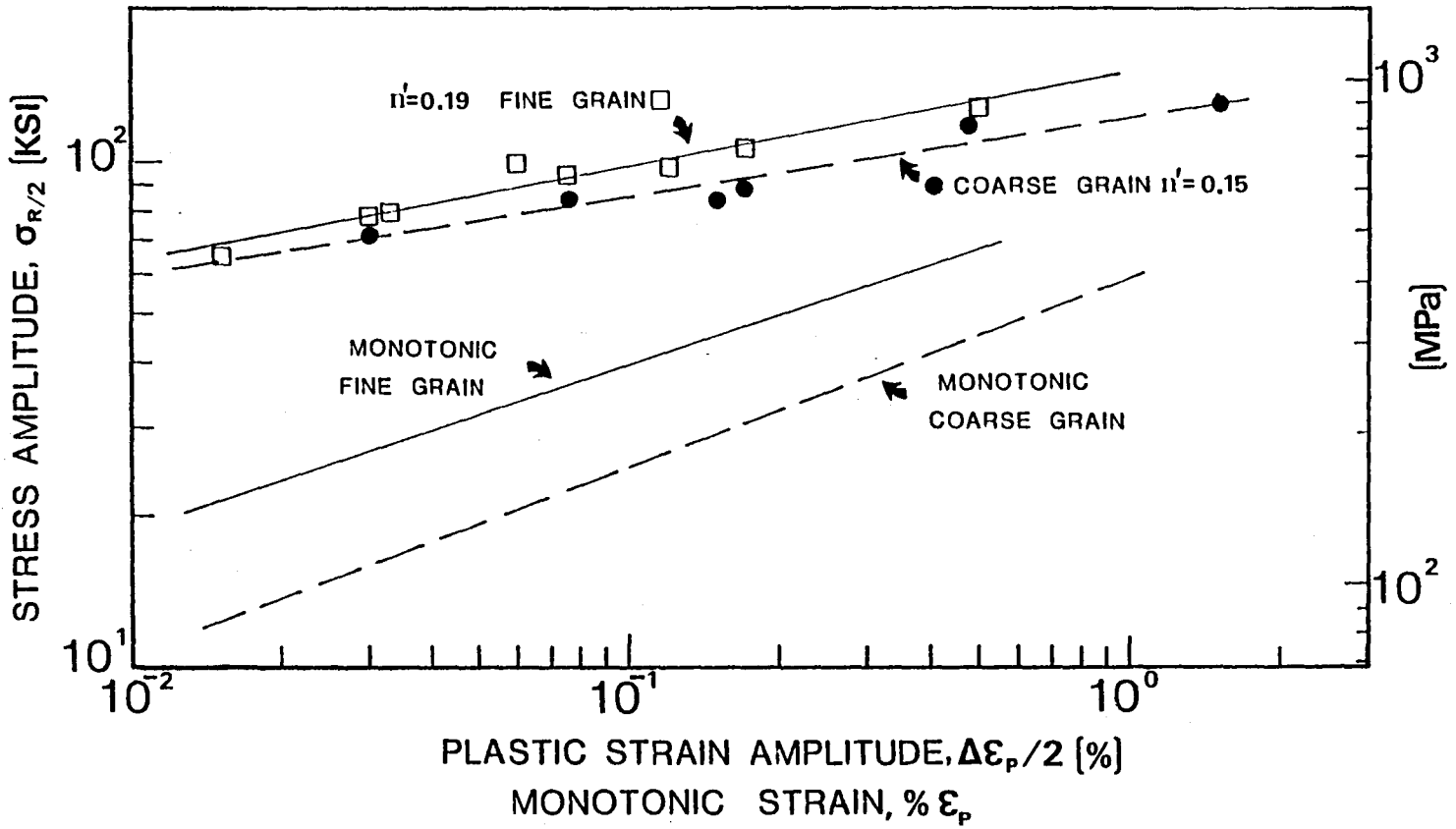

Figure 18 Waspaloy room temperature cyclic stress-strain curve. Cyclic hardening is observed over monotonic conditions.

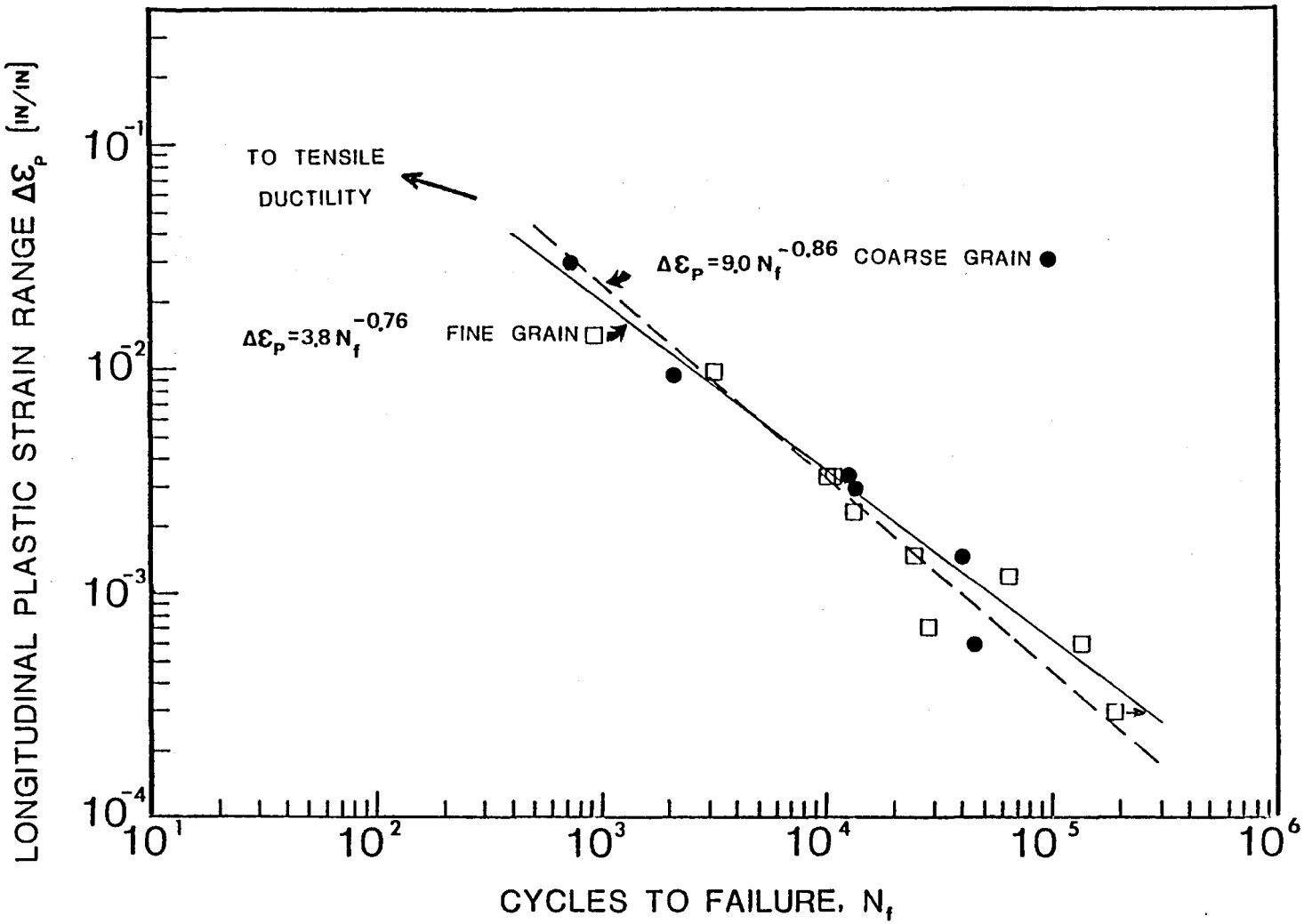

Figure 19 Coffin-Manson plots for Waspaloy tested at room temperature. Arrow indicates tensile ductility. Note that the LCF data does not extrapolate to the tensile ductility and is better observed in Fig. 20.

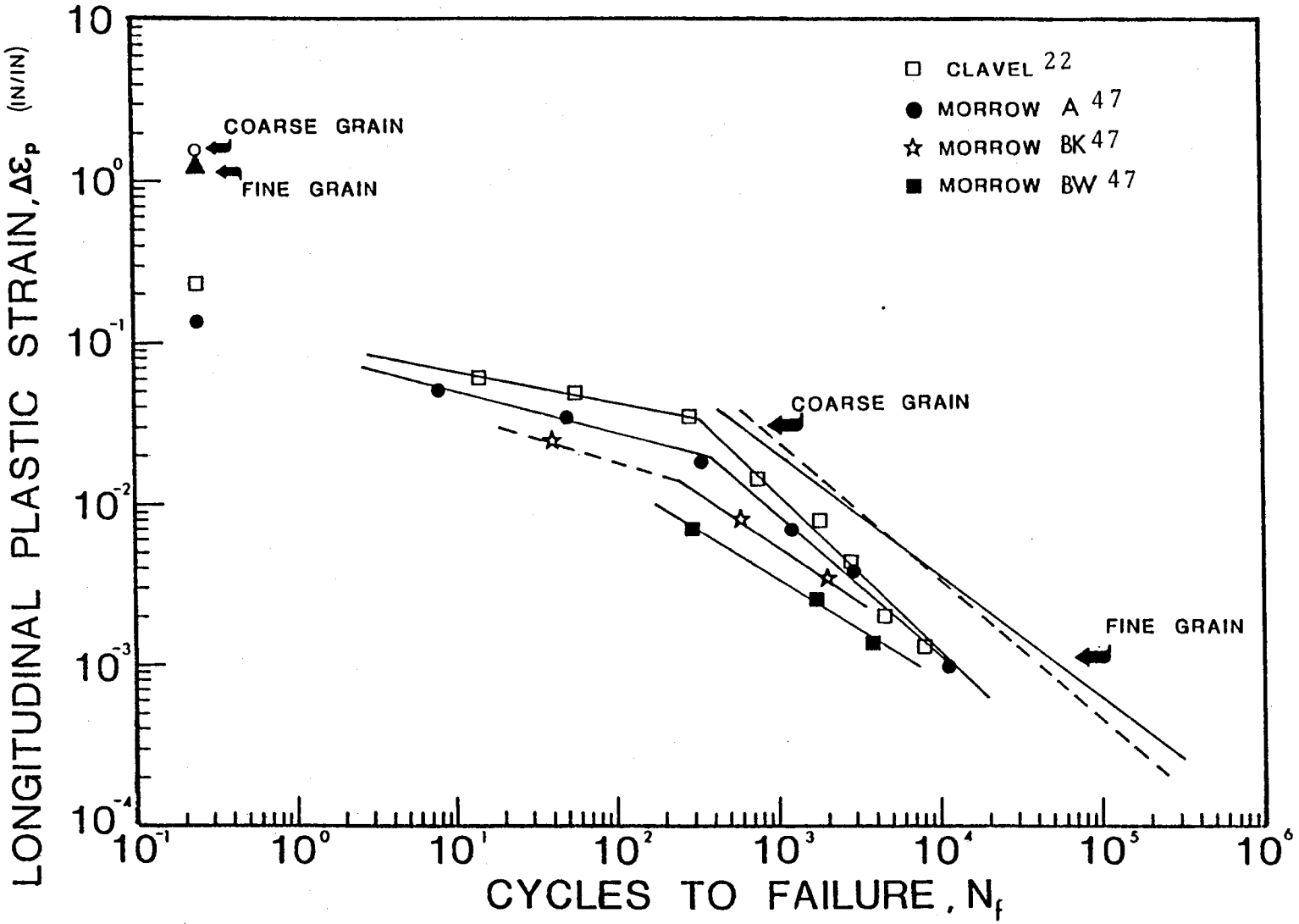

Figure 20 Coffin-Manson curves for Waspaloy LCF data. Morrow's data consist of two heat treatments A and B, Each treatment using materials from two different vendors, K and W. The materials used in the present study show the longest LCF lives per equivalent strain range and also the highest tensile ductility.

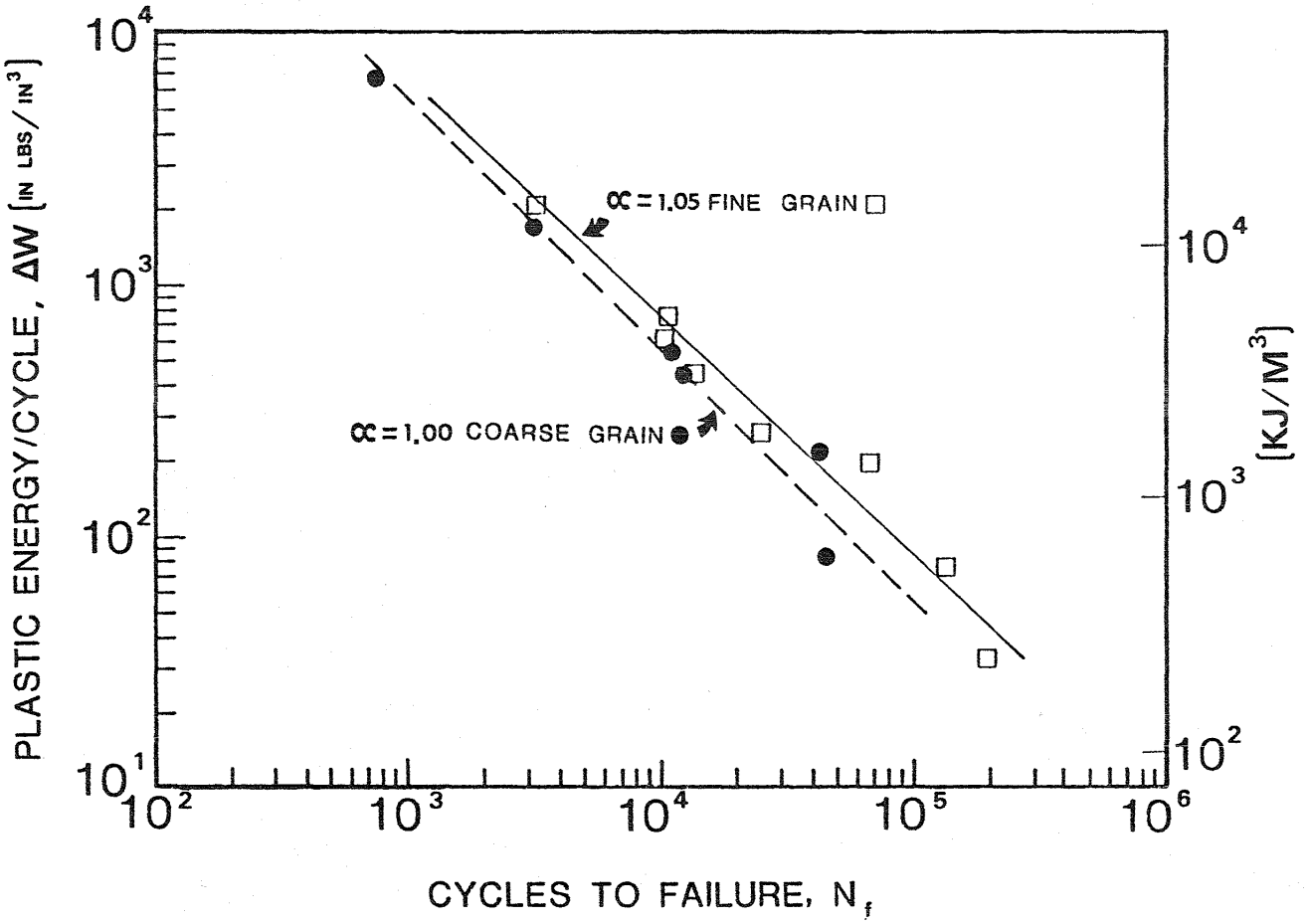

Figure 21 Plastic energy per cycle vs. cycles to failure for room temperature Waspaloy.

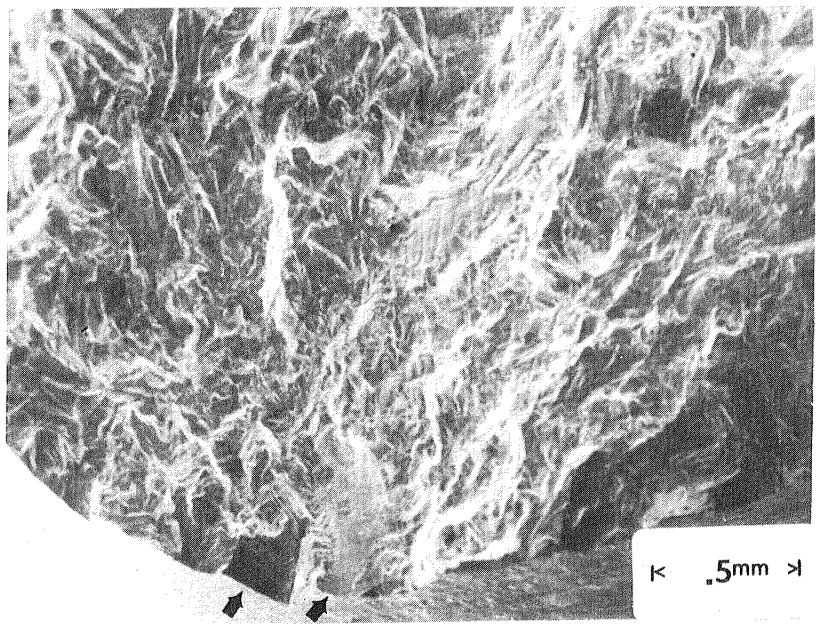

(a)

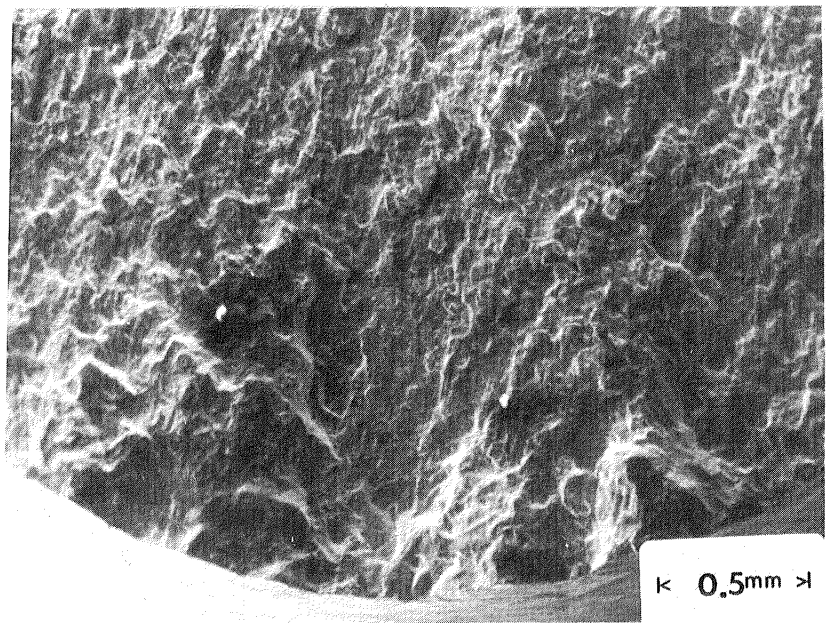

(b)

Figure 22 Fracture surfaces of coarse grained small γ' specimens. Low strain($\Delta\varepsilon_p$ =0.06%) specimen (a) exhibits a more crystallographic fracture than does the high strain($\Delta\varepsilon_p$ =3.00%) specimen (b). Arrows(a) indicate Stage I faceting of about one grain diameter.

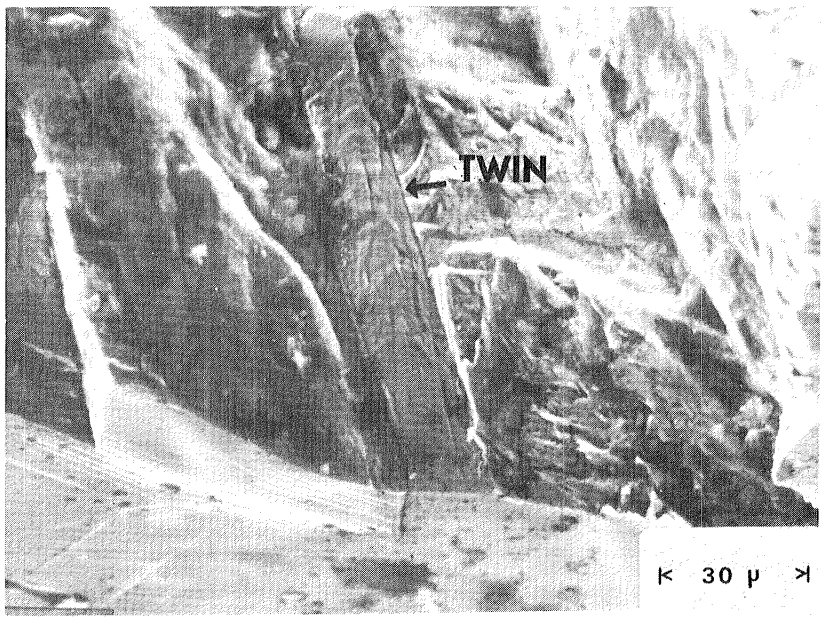

(a)

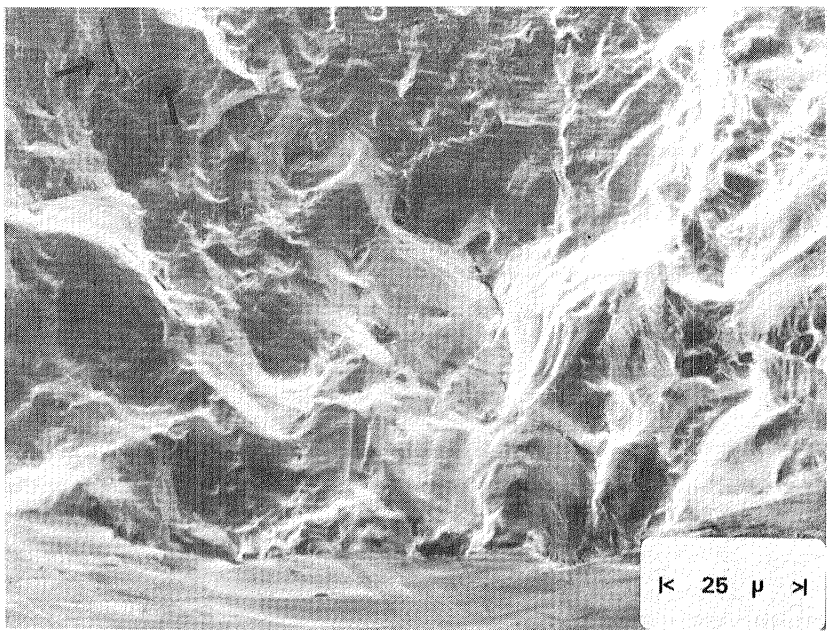

(b)

Figure 23 Typical initiation sites for the coarse grained small γ' specimens. a) Low strain($\Delta\varepsilon_p$ =0.06%) specimen exhibits slip band cracking(arrows). b) High strain($\Delta\varepsilon_p$ =3.00%) specimen exhibits relatively flat striated initiations with secondary slip band cracking(arrows).

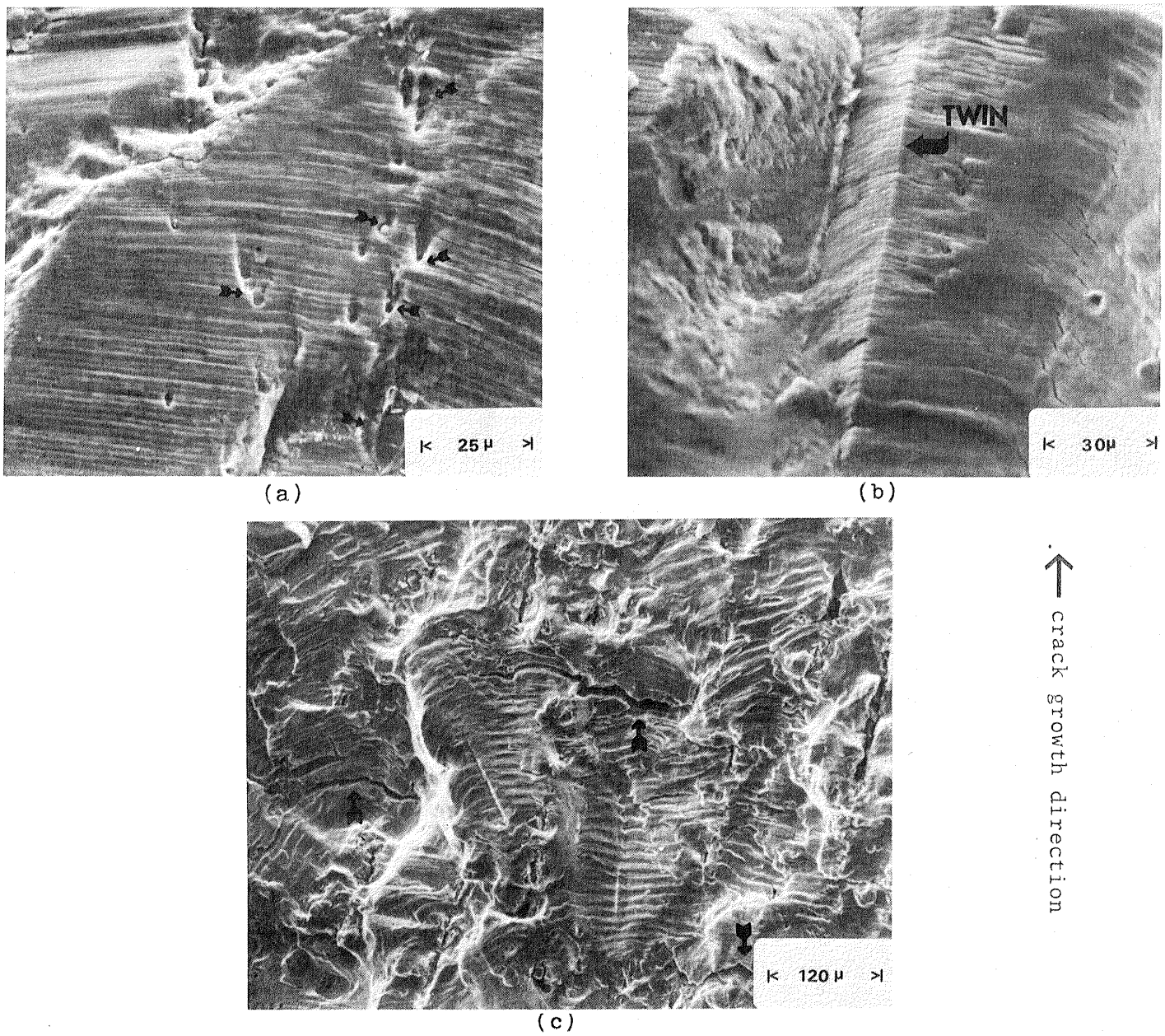

Figure 24 Striated propagation mechanisms for the coarse grained small γ' specimens. a) Spec. #5 low $\Delta\varepsilon_p$ indicates fine striations near an origin. Arrows indicate matrix carbides which form dimples in the fracture surface. Apparently these particles do not affect the growth of the crack as the striations do not 'bend' around these particles. b) Spec N_i 3 high $\Delta\varepsilon_p$ indicates fine striations near an origin. c) Spec N_i 3 remote from an origin shows a decreased striation density as the crack grows. Severe secondary cracking is also observed (arrows).

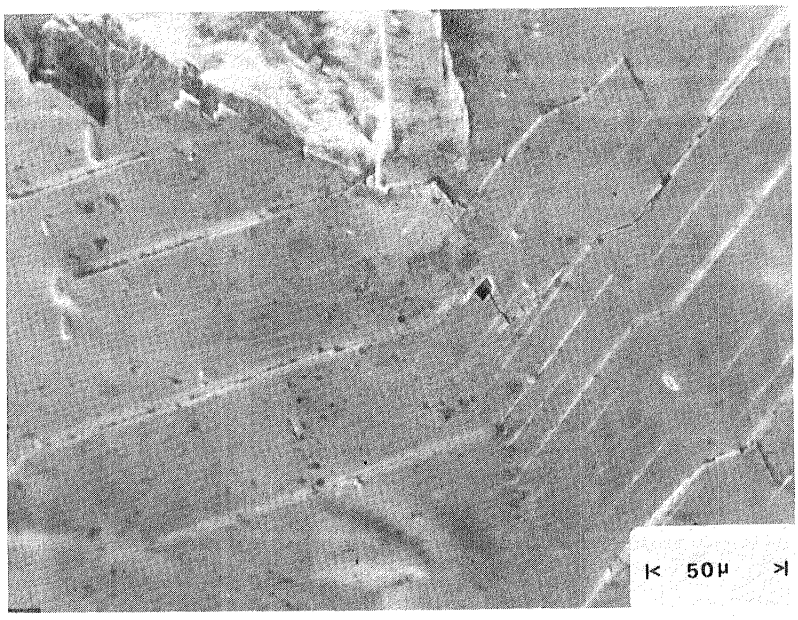

(a)

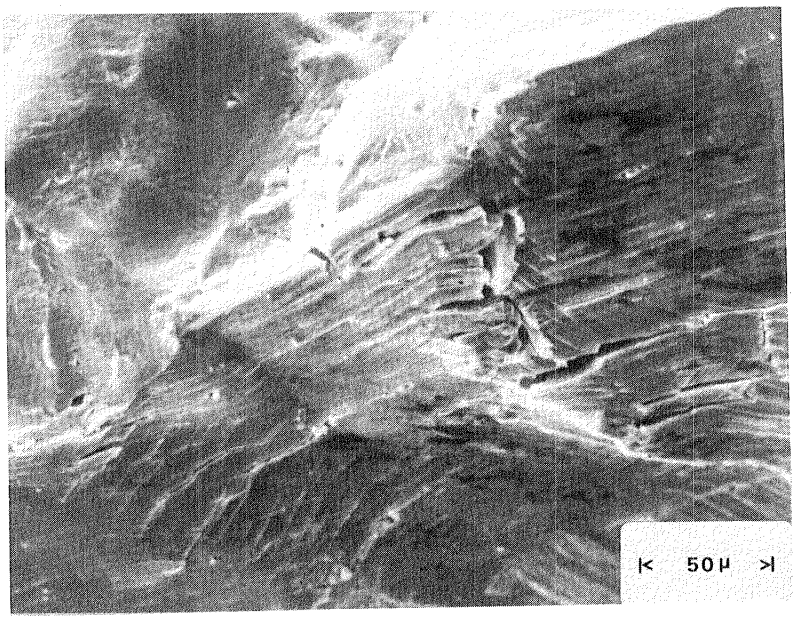

(b)

Figure 25 Slip band cracking on the gauge surfaces of the coarse grained small γ' specimens near crack origins. The slip band density is higher for a high strain($\Delta\varepsilon_p$ =3.00%) specimen(b) than for a low strain($\Delta\varepsilon_p$ =0.06%) specimen(a).

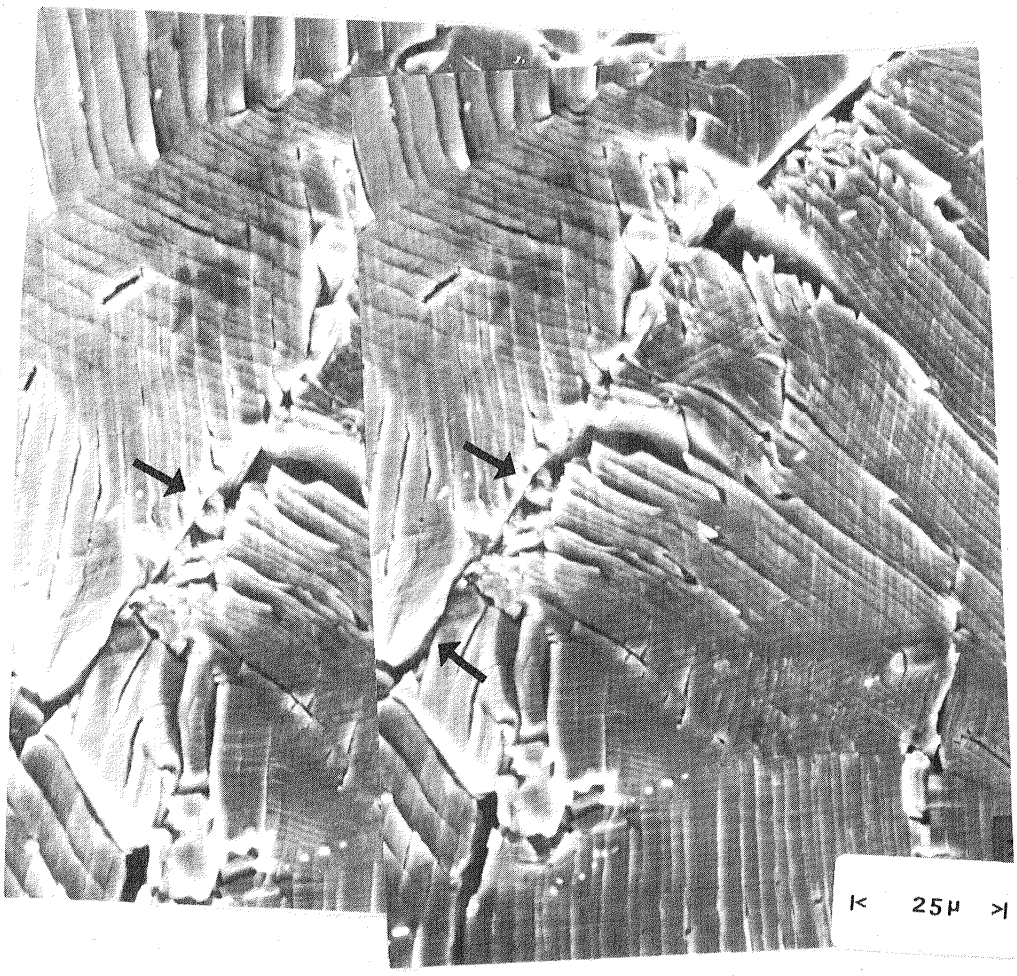

Figure 26 Stereo-pair of slip band cracking for coarse grained small γ' spec. N_i 3. Note that slip accommodation problems appear to be causing twin boundary cracking (arrows). $\Delta\varepsilon_p$ =3.00%

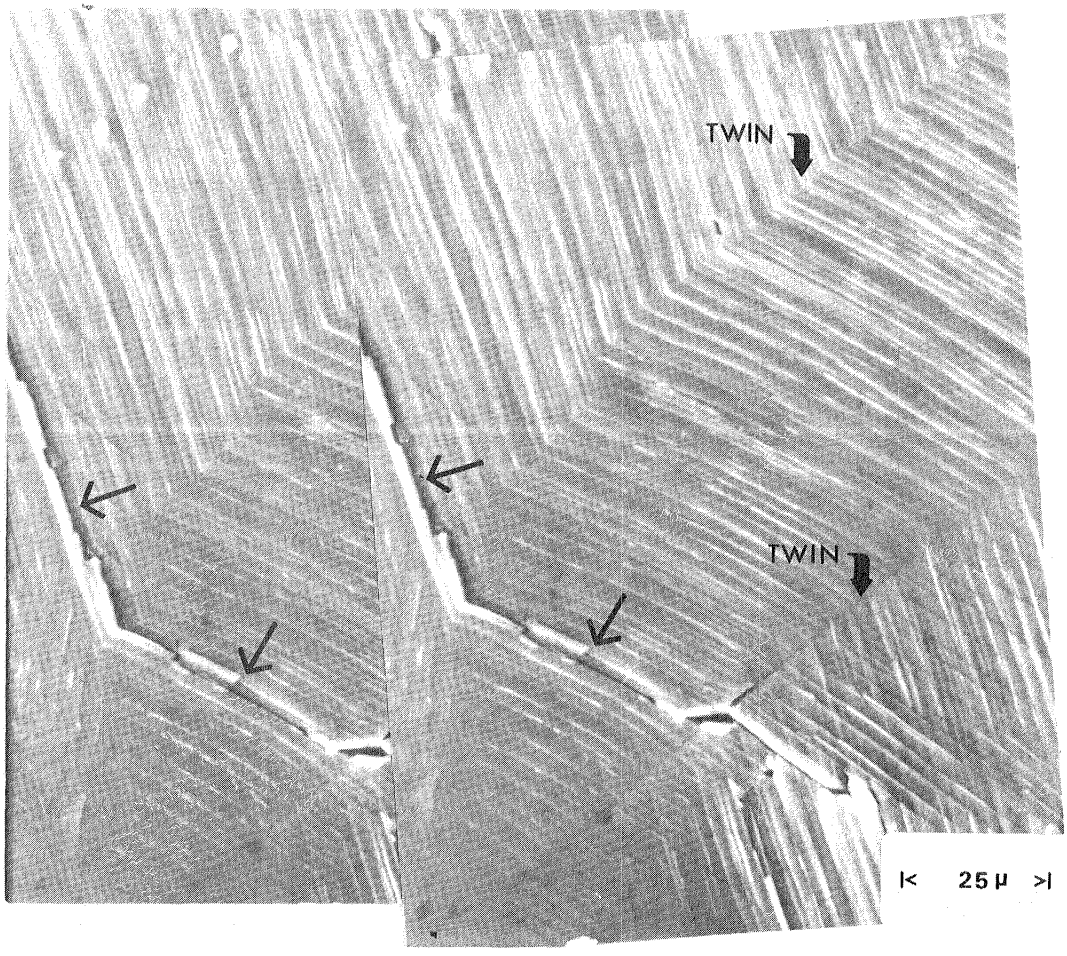

Figure 27 Stereo-pair of slip band activity for coarse grained small γ' specimen($\Delta\varepsilon_p$ =3.00%). Arrows indicate a slip band extrusion-intrusion. Slip accommodation problems at a twin boundary apparently initiated twin boundary cracking.

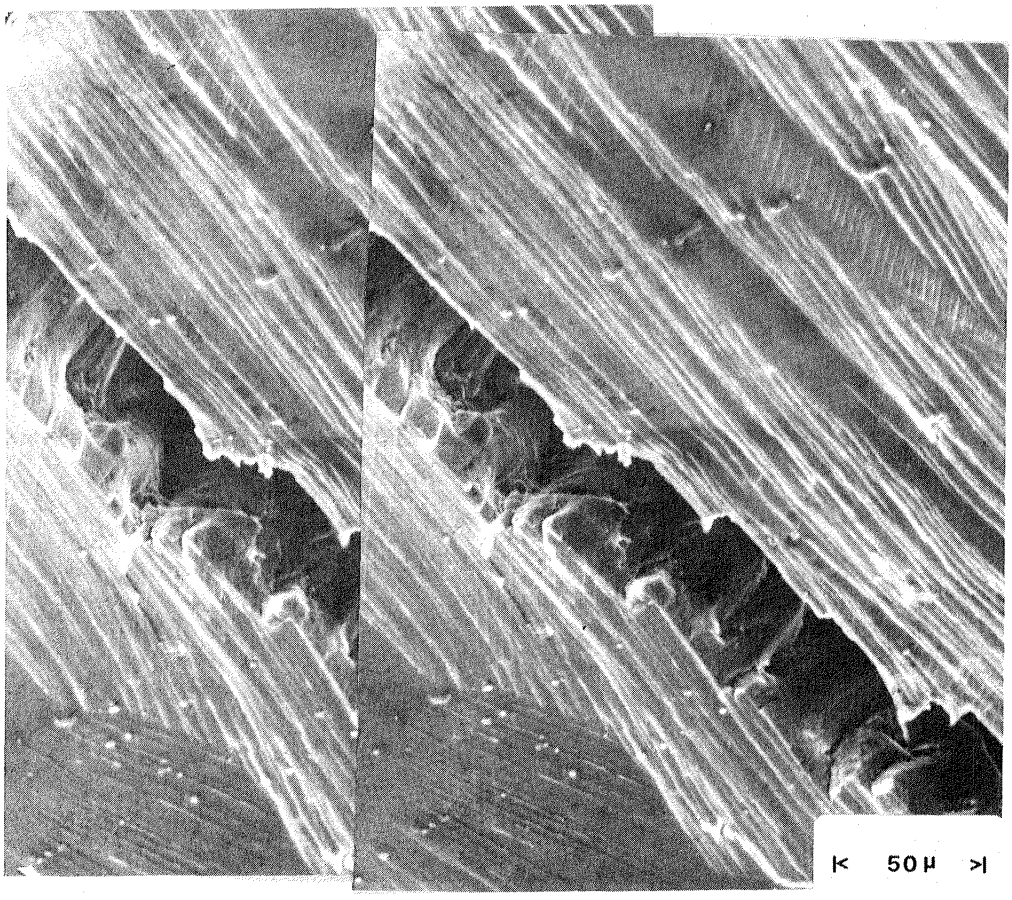

Figure 28 Stereo-pair of slip band initiated crack on the gauge of coarse grained small γ' spec. Ni 3. Propagation occurs almost immediately by a Stage II mechanism and is indicated by the river patterns inside the crack. $\Delta\varepsilon_p$ =3.00%

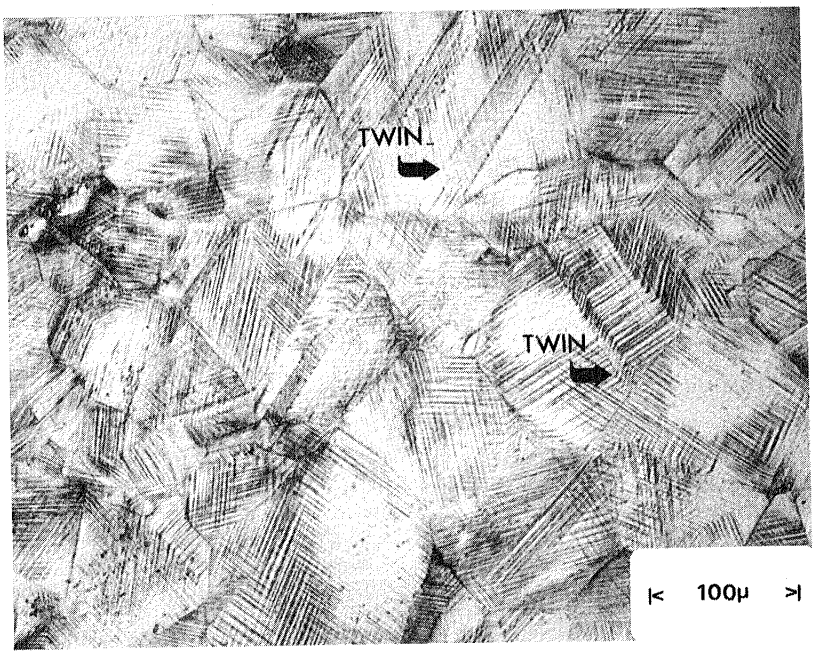

(a)

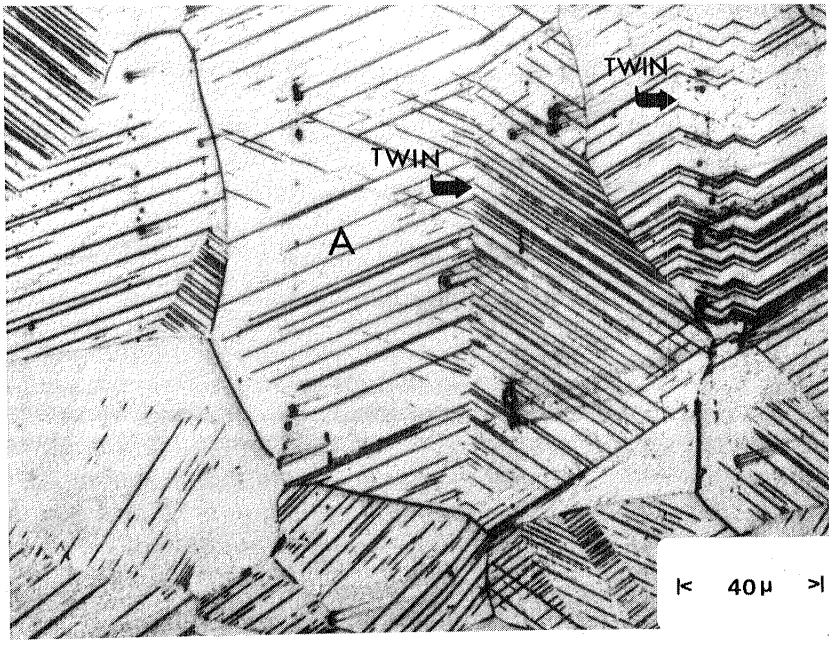

(b)

Figure 29 Optical micrographs of coarse grained small γ' specimens. High strain($\Delta\varepsilon_p$ =3.00%) specimen(a) has a higher slip band density than the low strain ($\Delta\varepsilon_p$=0.06%) specimen(b). Grain A as well as others exhibit multiple slip systems.

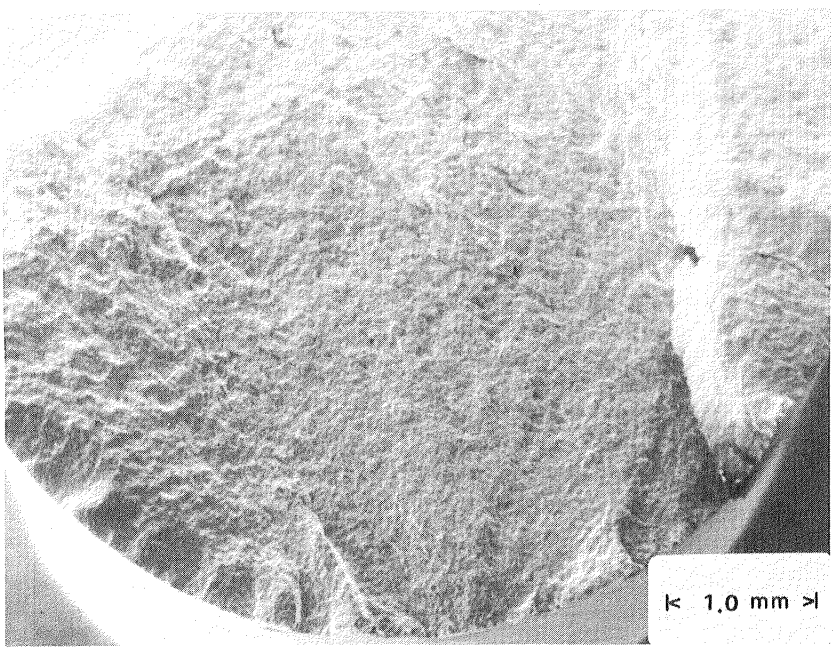

(a)

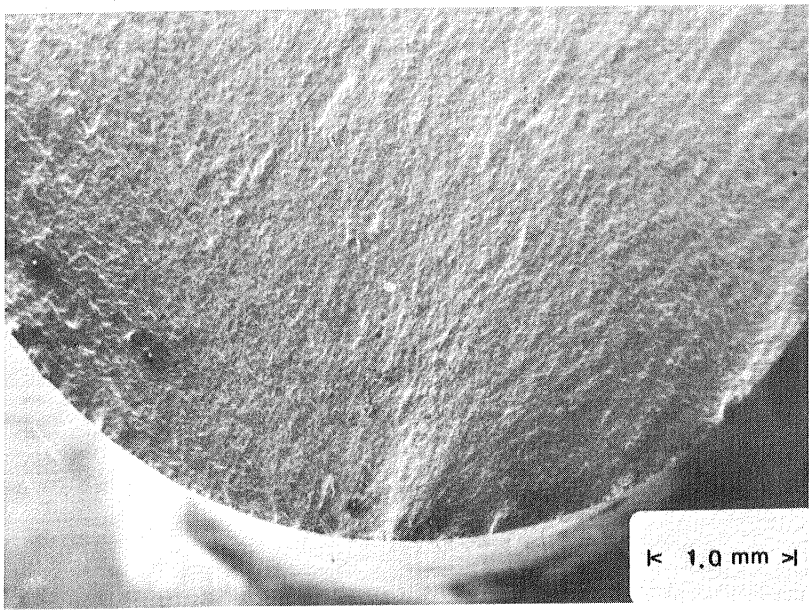

(b)

Figure 30 Fracture surfaces of the fine grained large γ' material. a) High strain($\Delta\varepsilon_p$ =1.00%) specimen b) Low strain($\Delta\varepsilon_p$=0.06%) specimen.

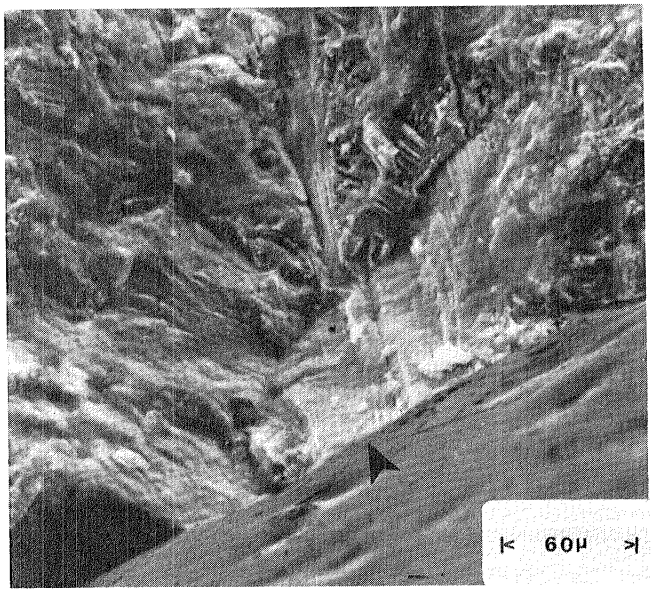

(a)

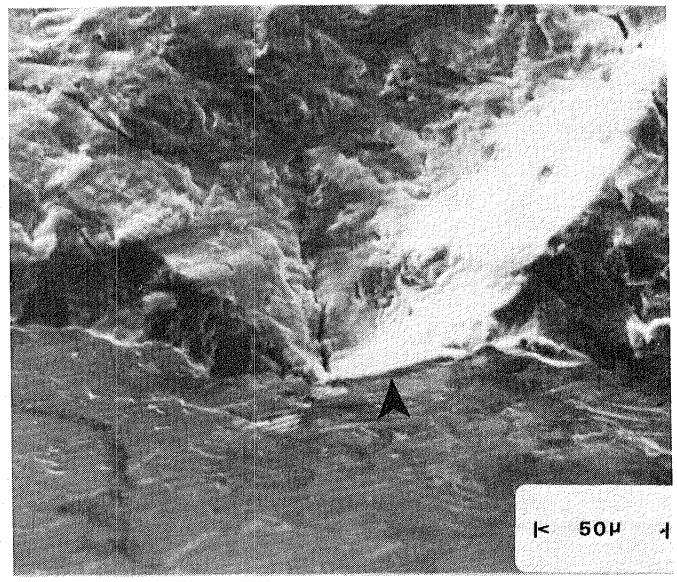

(b)

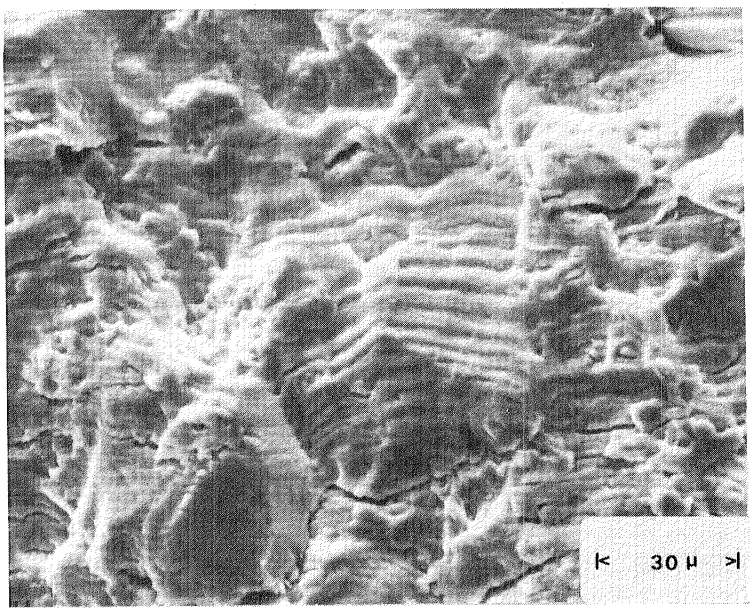

(c)

crack growth direction

Figure 31 Initiation sites of fine grained large γ' specimens at a) Low strain($\Delta\varepsilon_p$=0.06%) and b) High strain($\Delta\varepsilon_p$=1.00%). Cracking initiated at slip bands(arrows). c) Propagation by a striated mechanism in a high strain($\Delta\varepsilon_p$=1.00%) specimen.

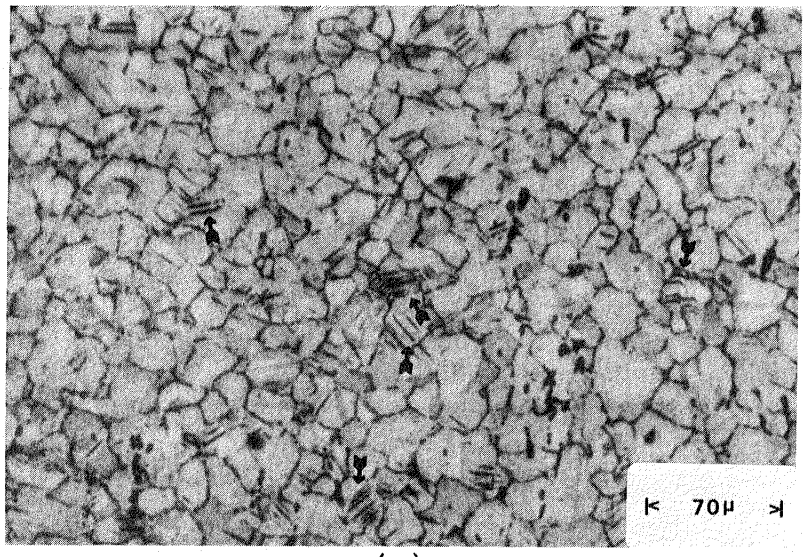

(a)

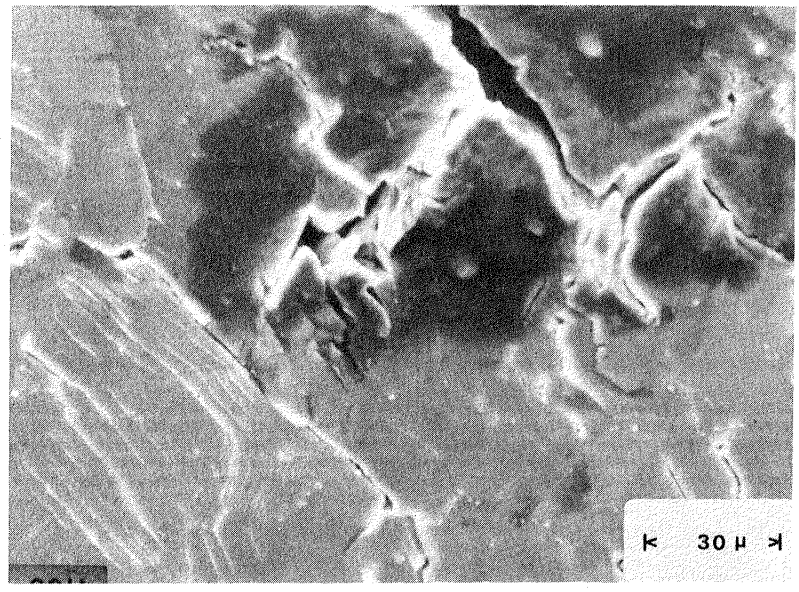

(b)

Figure 32 Optical micrograph(a) of fine grained large γ' specimen($\Delta\varepsilon_p$=0.06%) indicating a few slip bands(arrows). Gauge surface(b) of a high strain ($\Delta\varepsilon_p$=1.00%) specimen indicating slip band cracking. Slip bands appear wavier than in the coarse grained material.

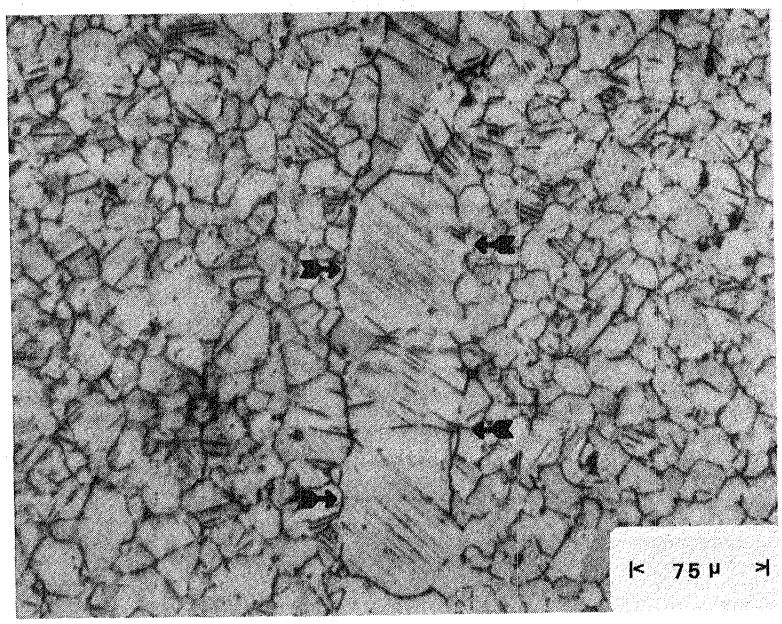

(a)

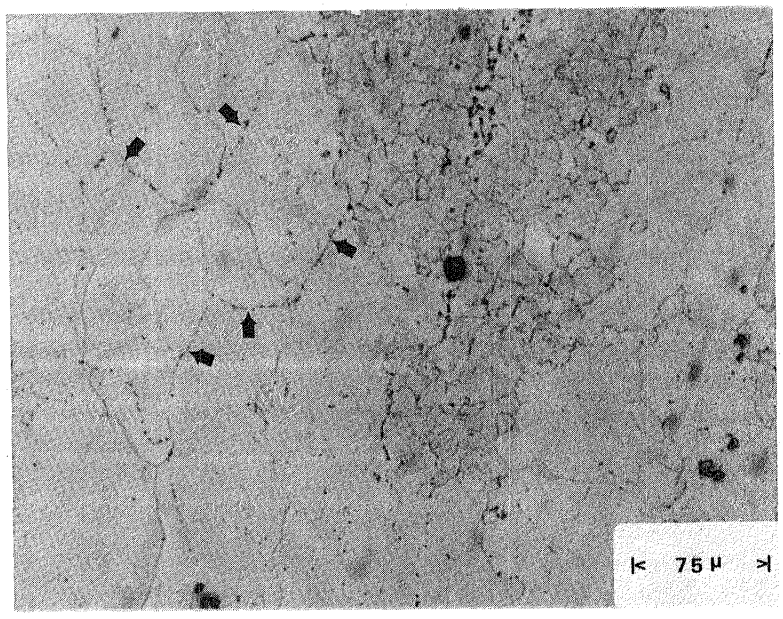

(b)

Figure 33 Fine grained large γ' specimen #12 (a) contains some areas of anomalous grain growth(arrows). This was typical of most of the fine grained specimens, but did not appear to affect the properties. Fine grained large γ' specimen #10 (b) contained areas of large equiaxed grains. Carbide networks from prior grain boundaries(arrows) were also evident. This specimen exhibited fatigue properties close to those of the coarse grained specimens.

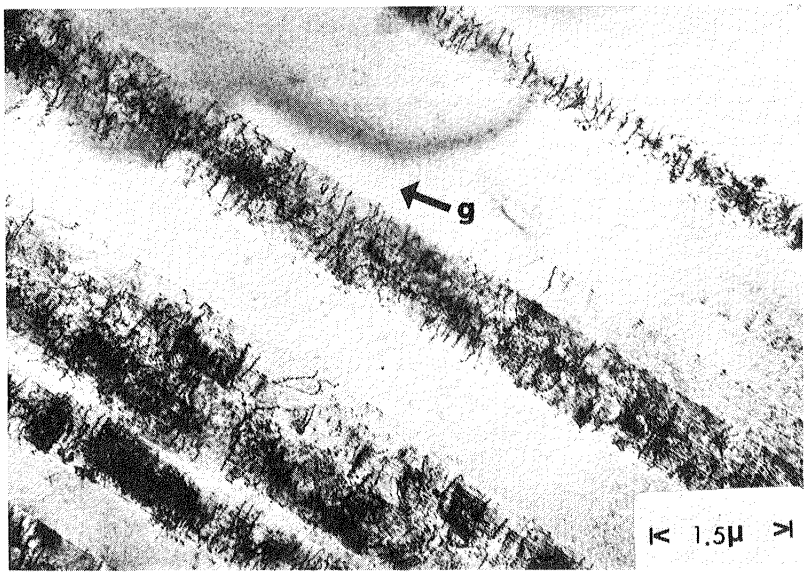

(a)

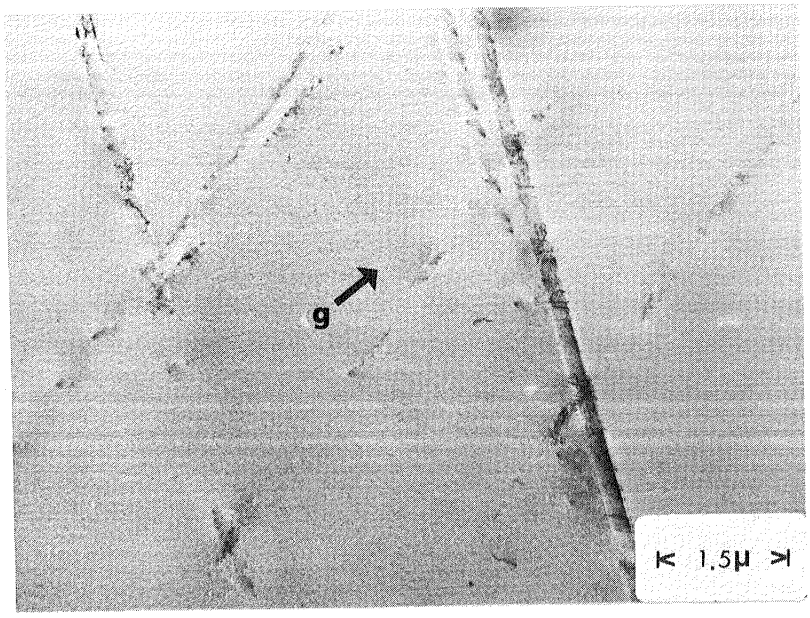

(b)

S.F.=0.42

Figure 34 Slip bands operating under {111} reflections for spec. 4 $\Delta\varepsilon_p$ =0.30%(a) and spec. 5 $\Delta\varepsilon_p$ =0.06% (b). Bands are at an angle to the electron beam. These were coarse grained small γ' specimens.

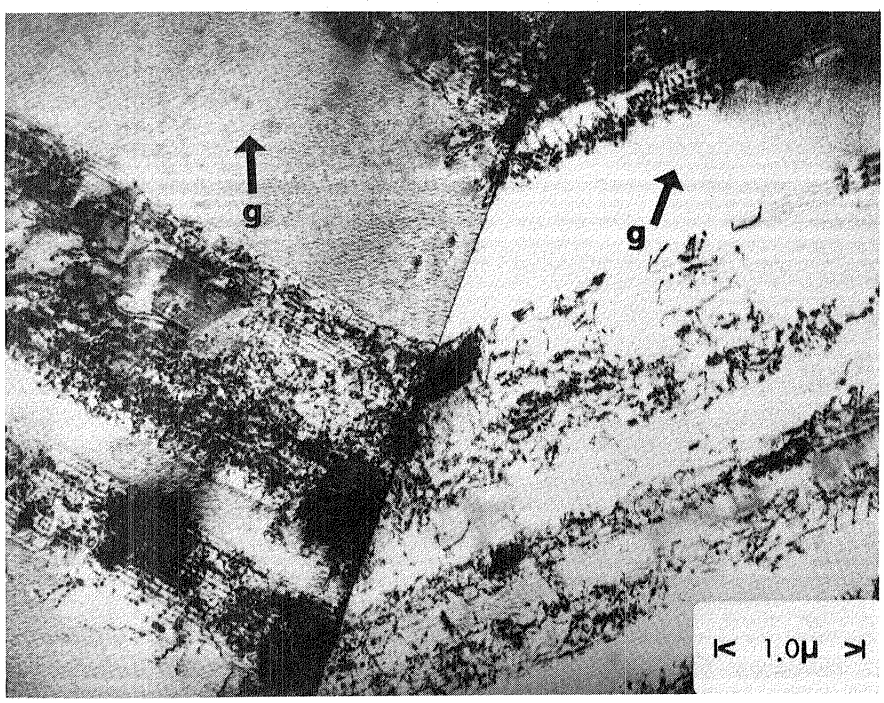

Figure 35 Slip transfer across a grain boundary for coarse grained small γ' spec. 4. g= {200} for both grains.

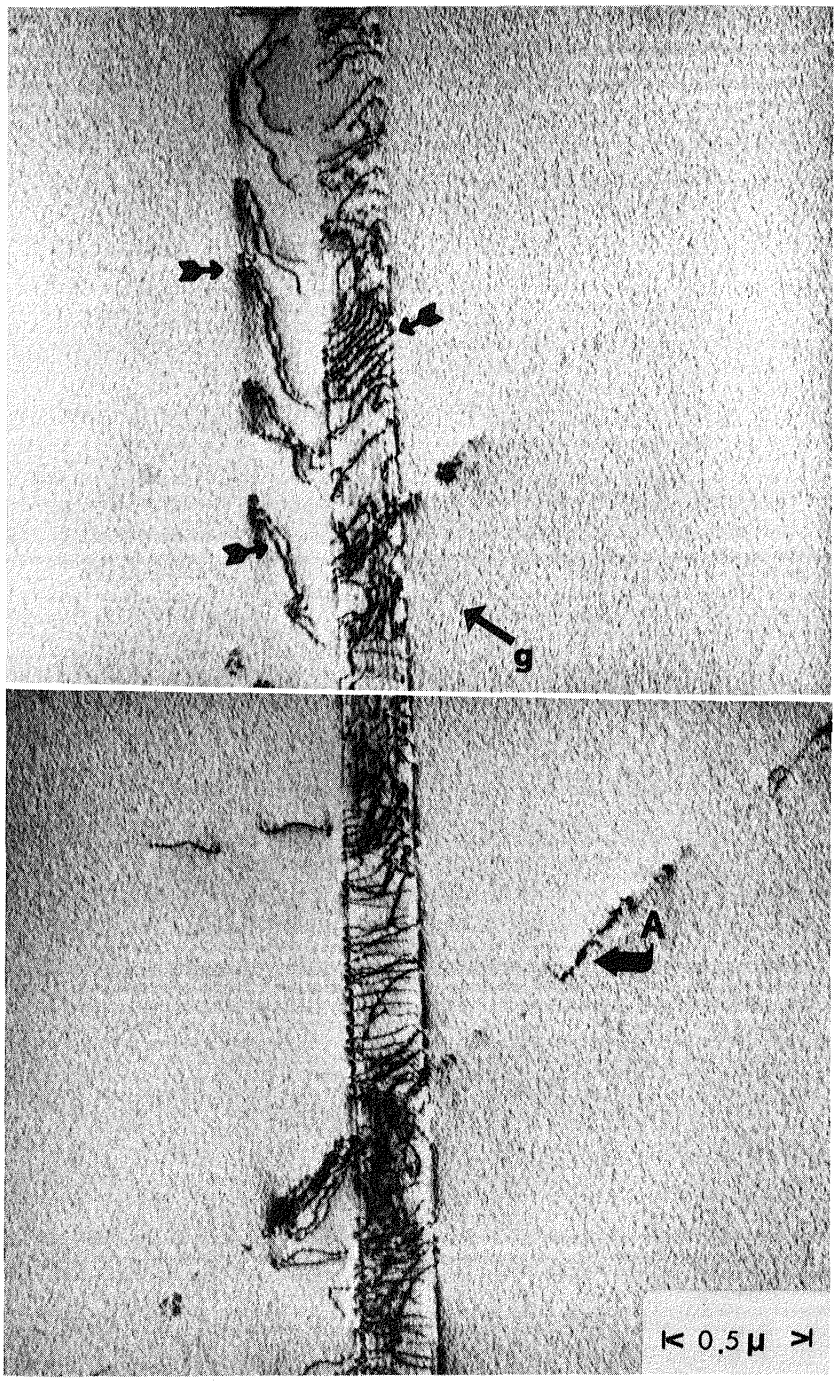

Figure 36 Coarse grained small γ' spec. 5($\Delta\varepsilon_p$=0.06%). {200} reflection revealed the individual dislocations within the bands. Arrows indicate dislocation pairs. 'A' planes were another slip system which was oriented closer to the edge on condition.

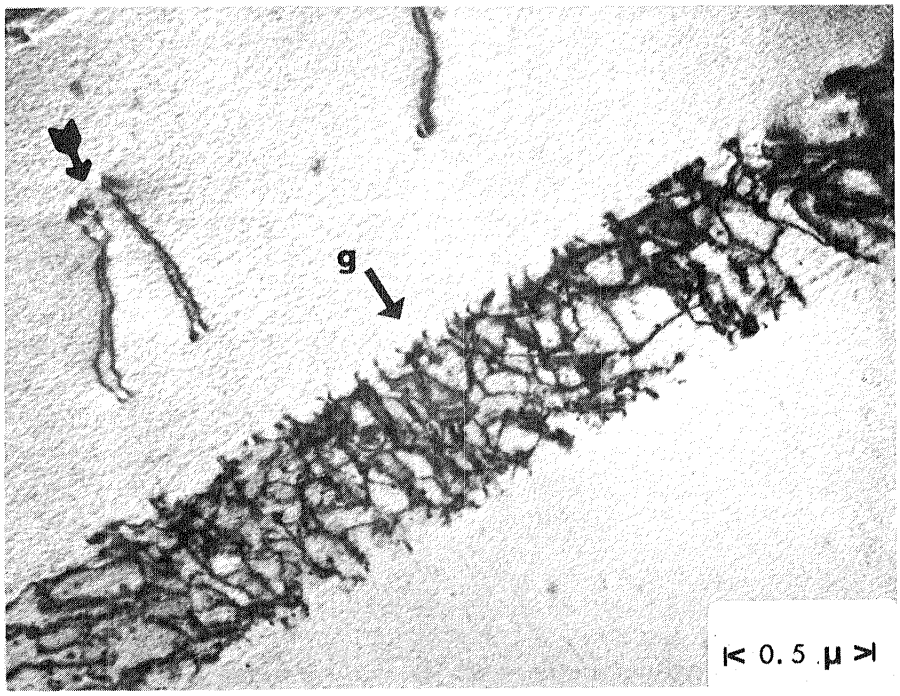

Figure 37 Coarse grained small γ' spec. 4($\Delta\varepsilon_p$=0.30%). {200} reflection shows a near cellular arrangement of dislocations within a slip band. Note the dislocation pairs(arrow) above the band.

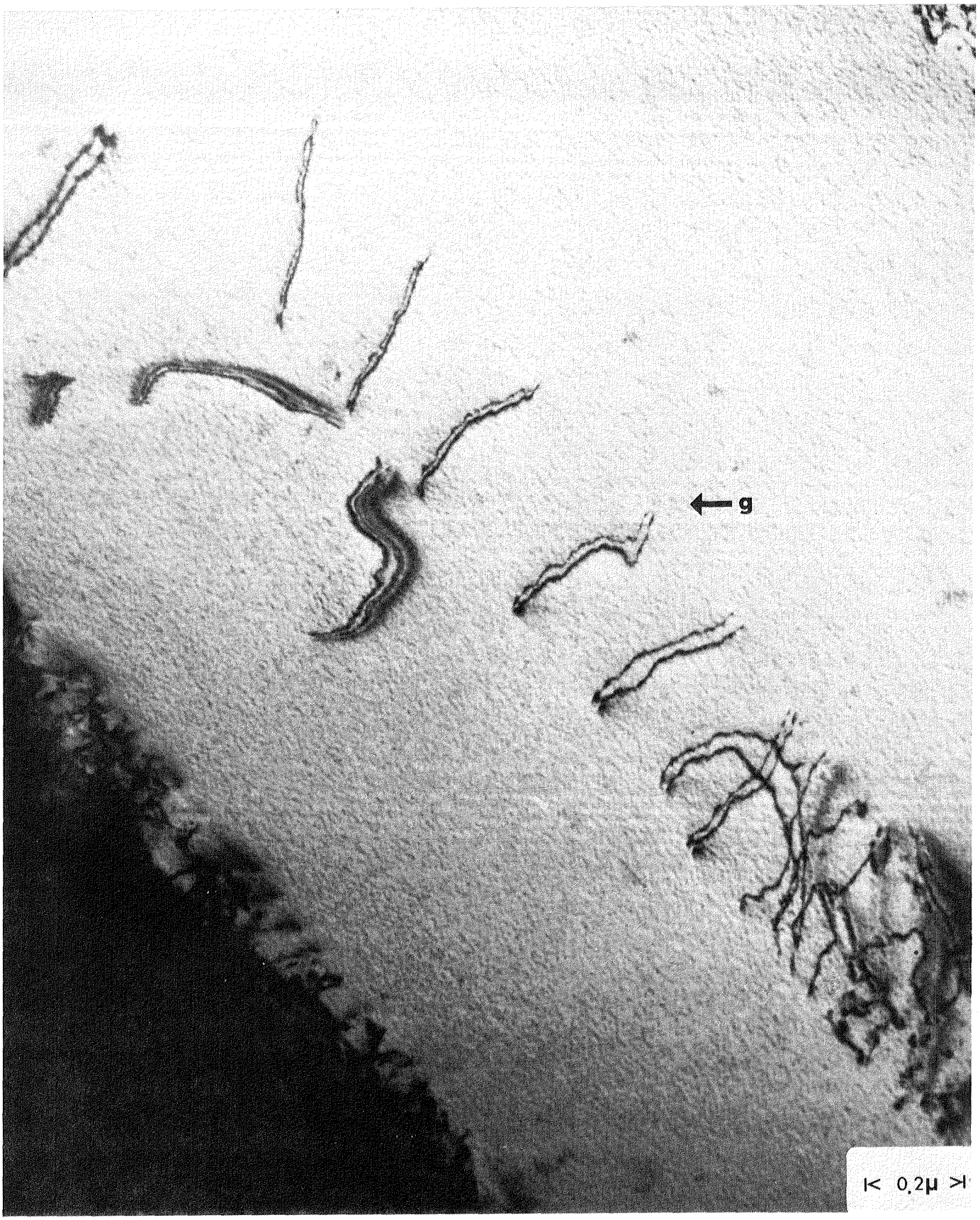

Figure 38 Coarse grained small γ' spec. 4($\Delta\varepsilon_p$=0.30%). { 200 } reflection revealed dislocation pairs in a slip band.

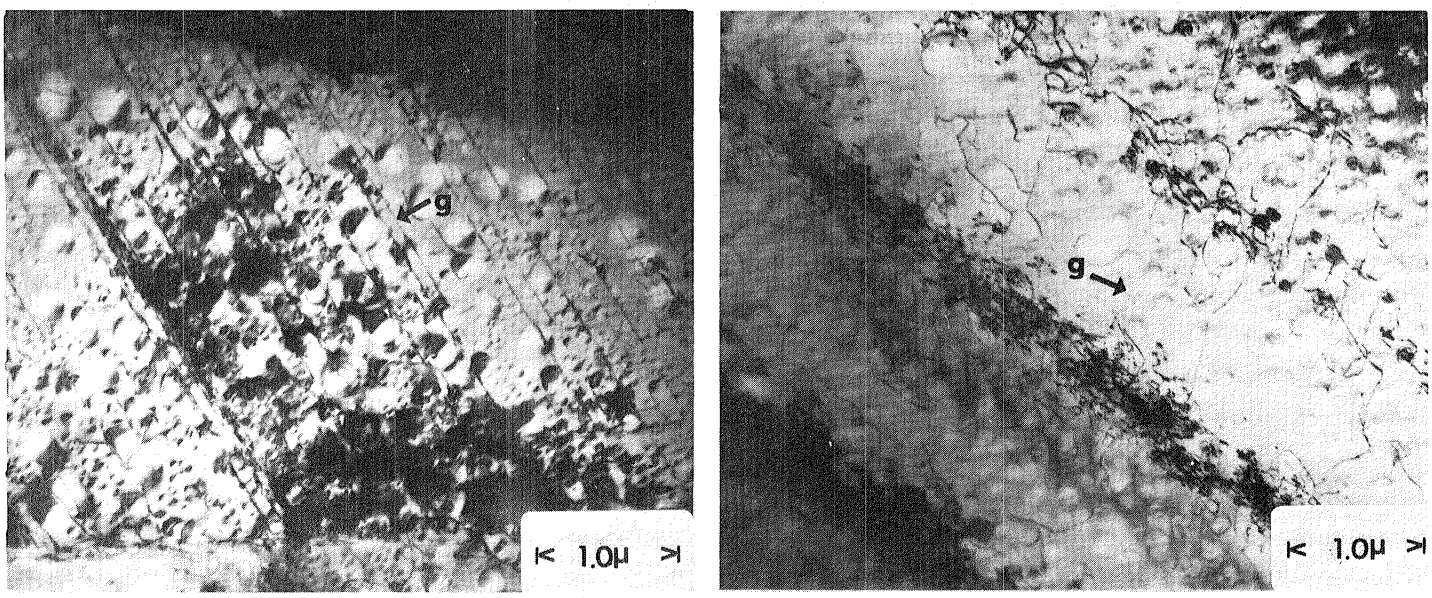

S.F.=0.43 (a) (b)

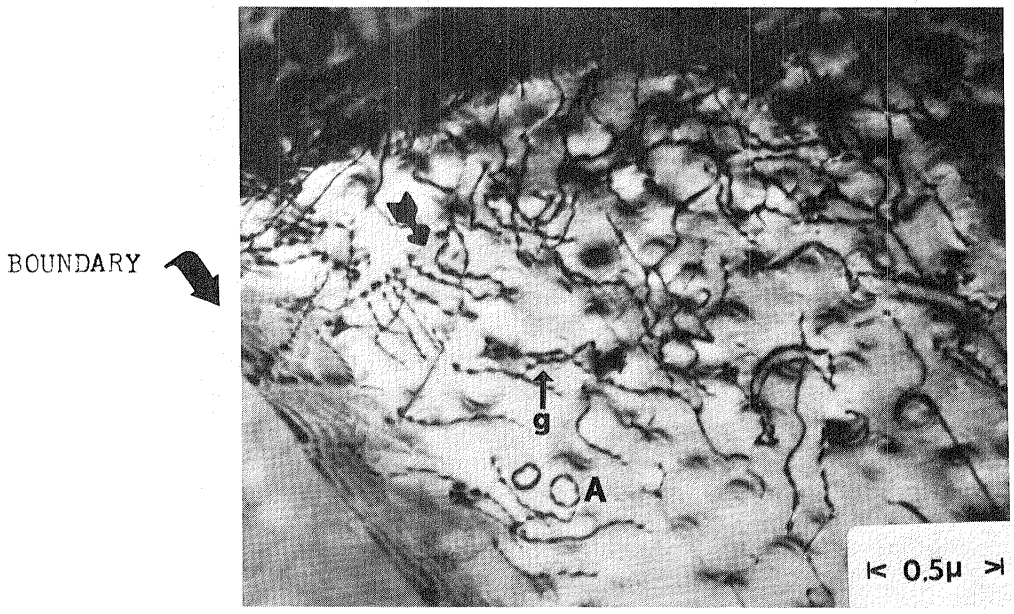

(c)

Figure 39 Fine grained large γ' spec. 12($\Delta\varepsilon_p$=0.06%). Edge on view of slip bands(a) using a (111) reflection. Another grain(g={111}) showing slip bands at an angle to the beam(b). c) Arrow indicates the bowing mechanism and 'A' indicates looping(g={200}).

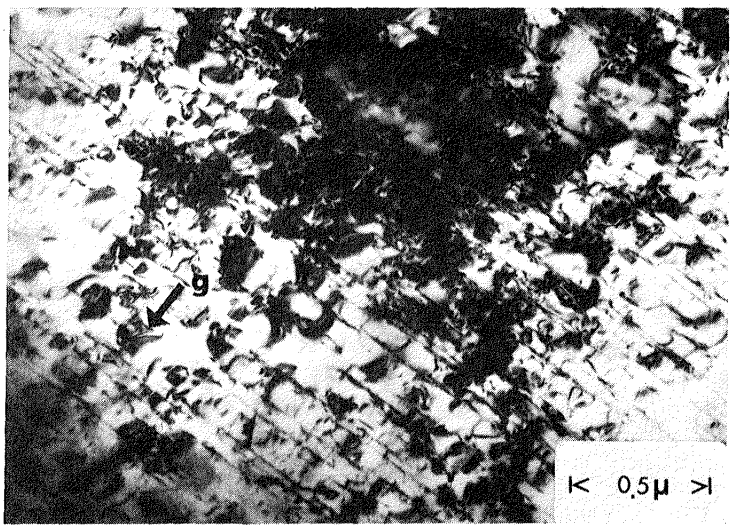

(a)

S.F.=0.44

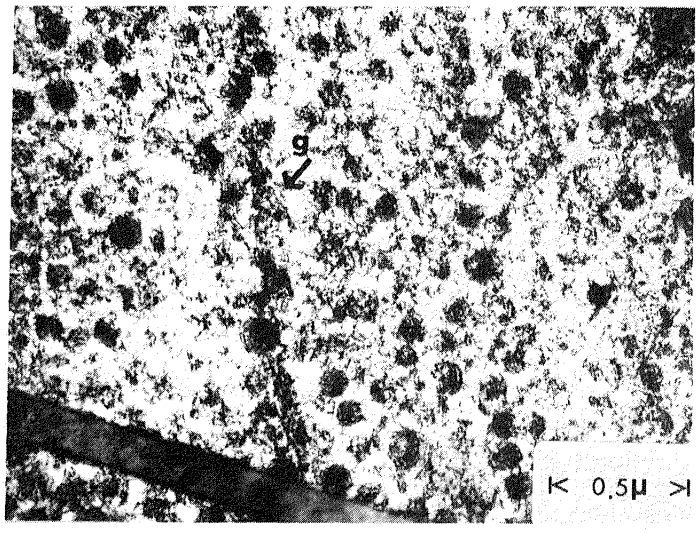

(b)

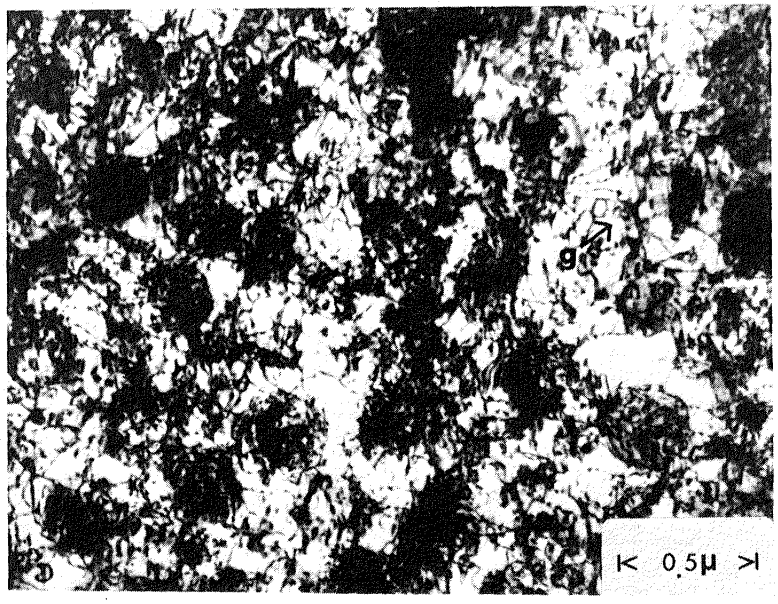

(c)

Figure 40 Dislocation structure in fine grained small γ' specimen($\Delta\varepsilon_p$ =1.00%). Edge-on view(a) of slip planes(g= {111}). Looping mechanism (b) using a {200} reflection. Extensive dislocation build-up around γ' particles(c) caused some of them to appear black(g={200}).

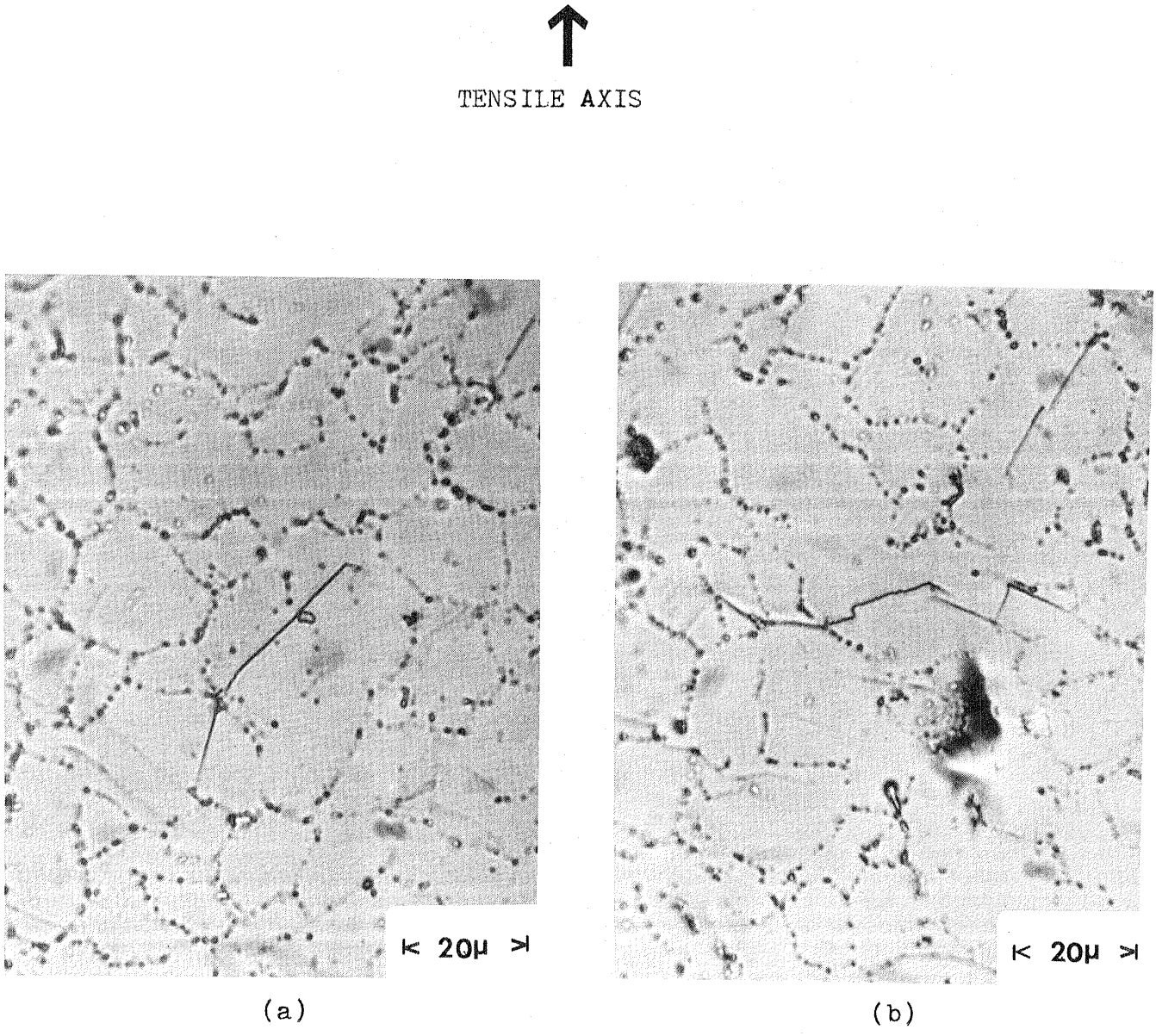

Figure 41 Slip bands in fine grained large γ' specimen N_i 1 ($\Delta\varepsilon_p = 0.12\%$). a) At 6000 cycles. b) At 9000 cycles.

TENSILE AXIS

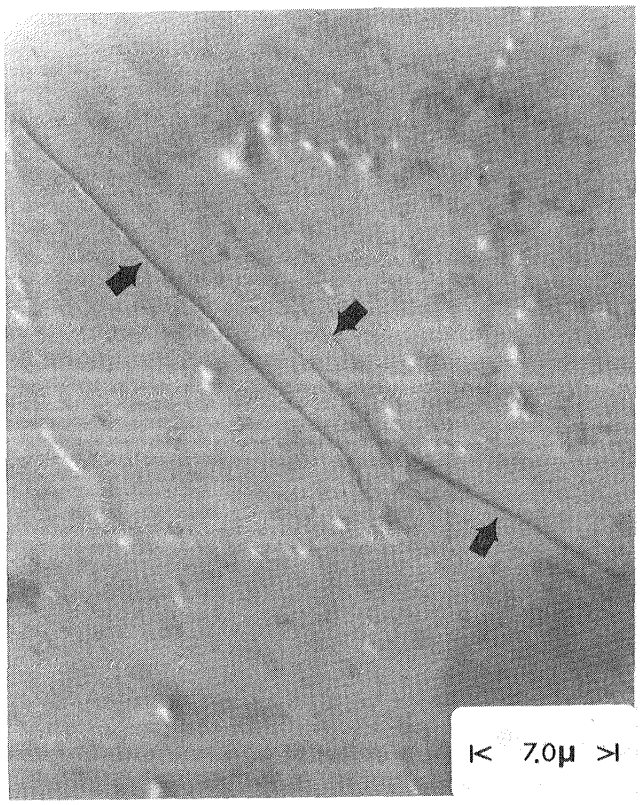

Figure 42 Fine grained large γ' specimen($\Delta\varepsilon_p$ =0.12%) stopped at 6000 cycles. SEM indicated slip bands(arrows) on the gauge surface but no cracking.

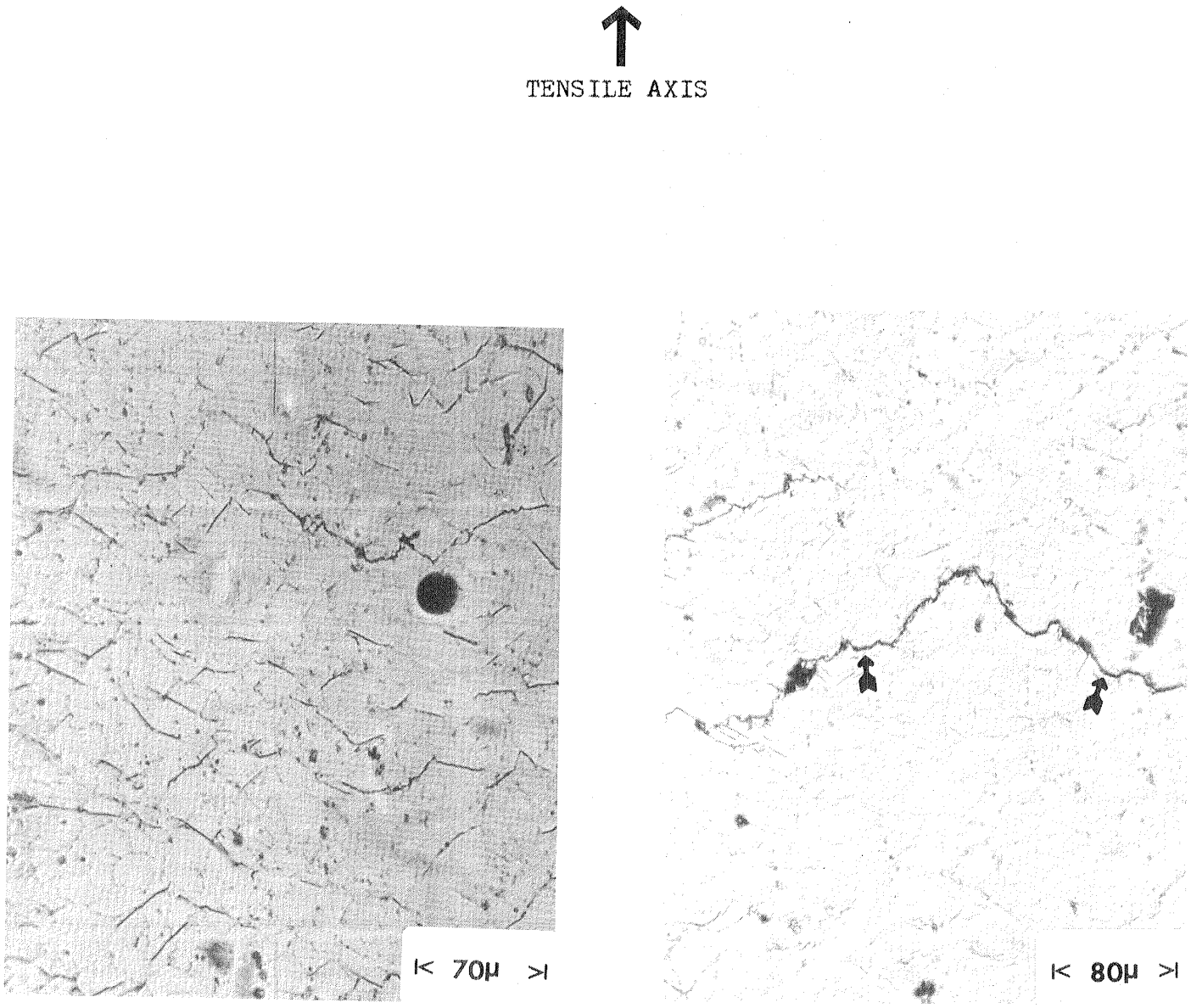

Figure 43 Fine grained large γ'. a) Specimen N_i 1 ($\Delta\varepsilon_p$ =0.12%) shows slip band link-up and cracking at 72% of the life(49000 cycles). b) Specimen N_i 4($\Delta\varepsilon_p$ =1.00%) shows a 450μ crack(arrows) at 80%(2650 cycles) of the life.

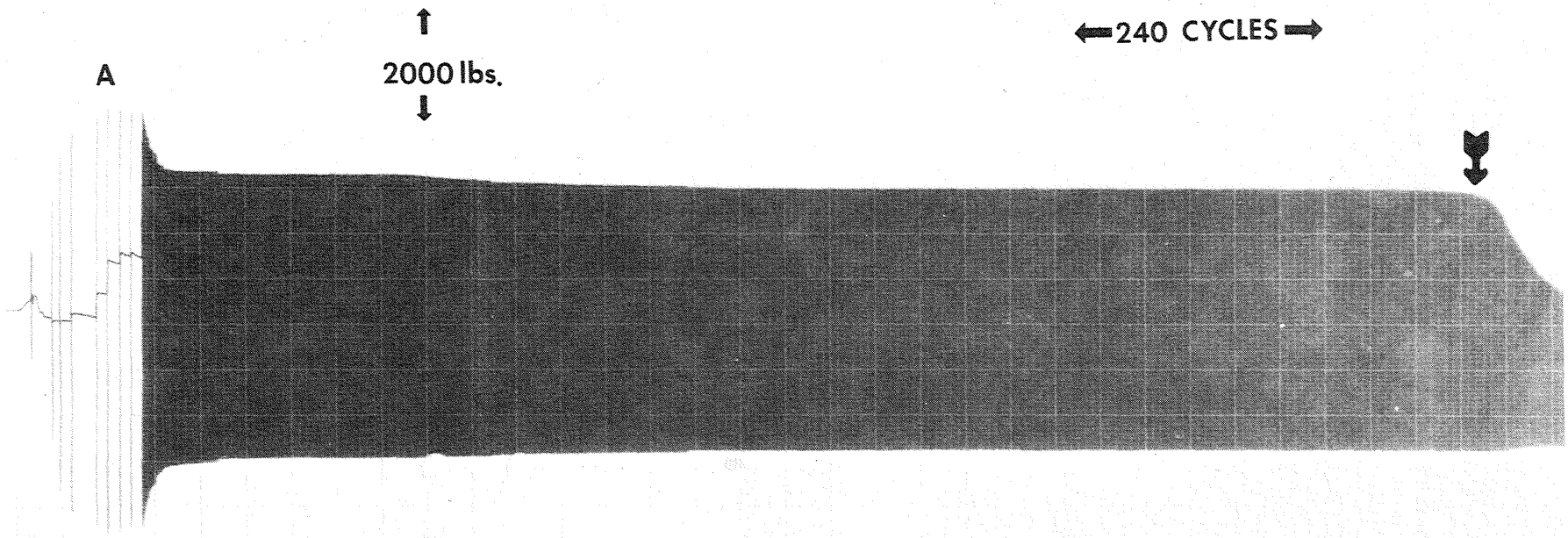

Figure 44 Typical load vs. cycle plot from the strip chart recorder. Area 'A' shows beginning cycles where testing was stopped after each cycle to measure the strain. Arrow indicates the final load drop.

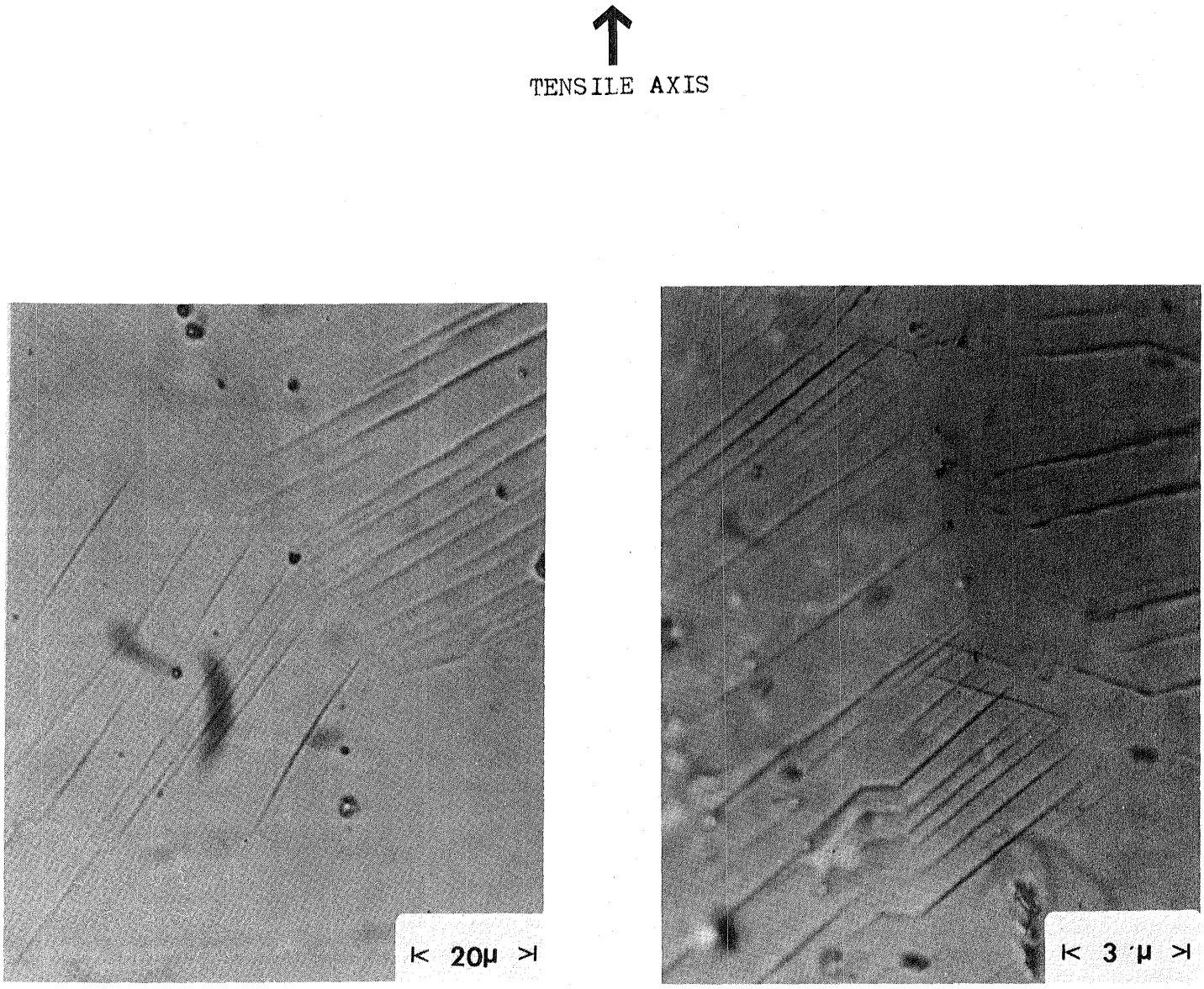

(a) (b)

Figure 45 Slip bands in coarse grained small γ' specimen Ni 2($\Delta\varepsilon_p$= o.15%) at a) 18 cycles(σ max) and b) 1000 cycles.

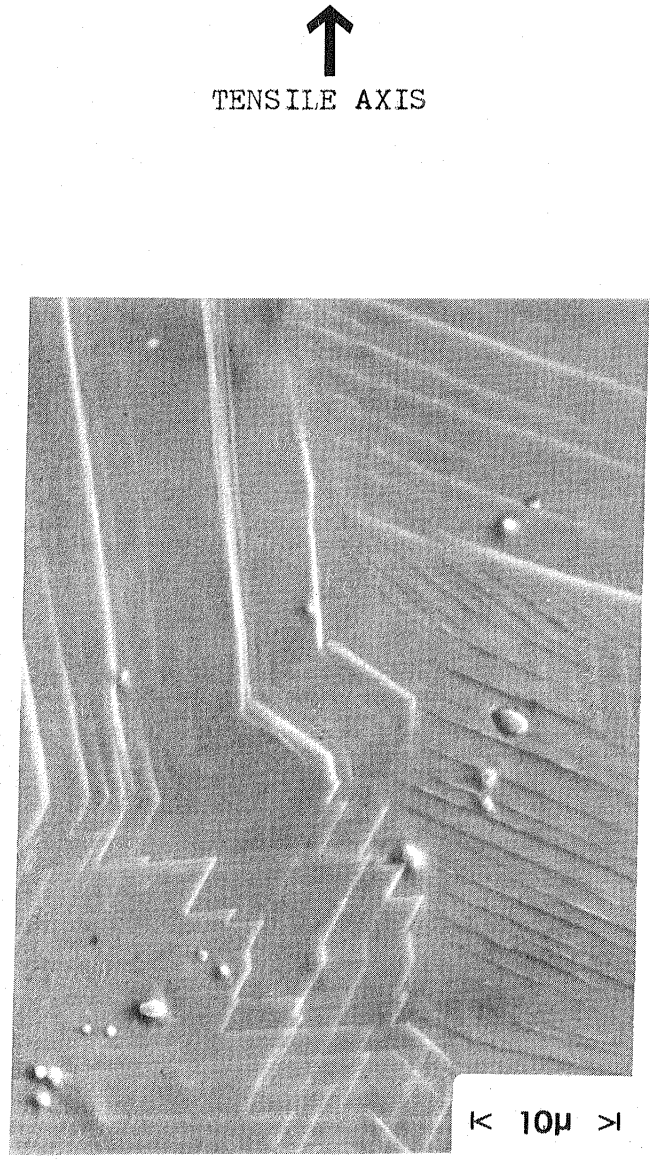

Figure 46 Coarse grained small γ' specimen($\Delta\varepsilon_p$=0.15%) stopped at 1000 cycles. SEM indicated slip bands on the gauge surface but no cracking.

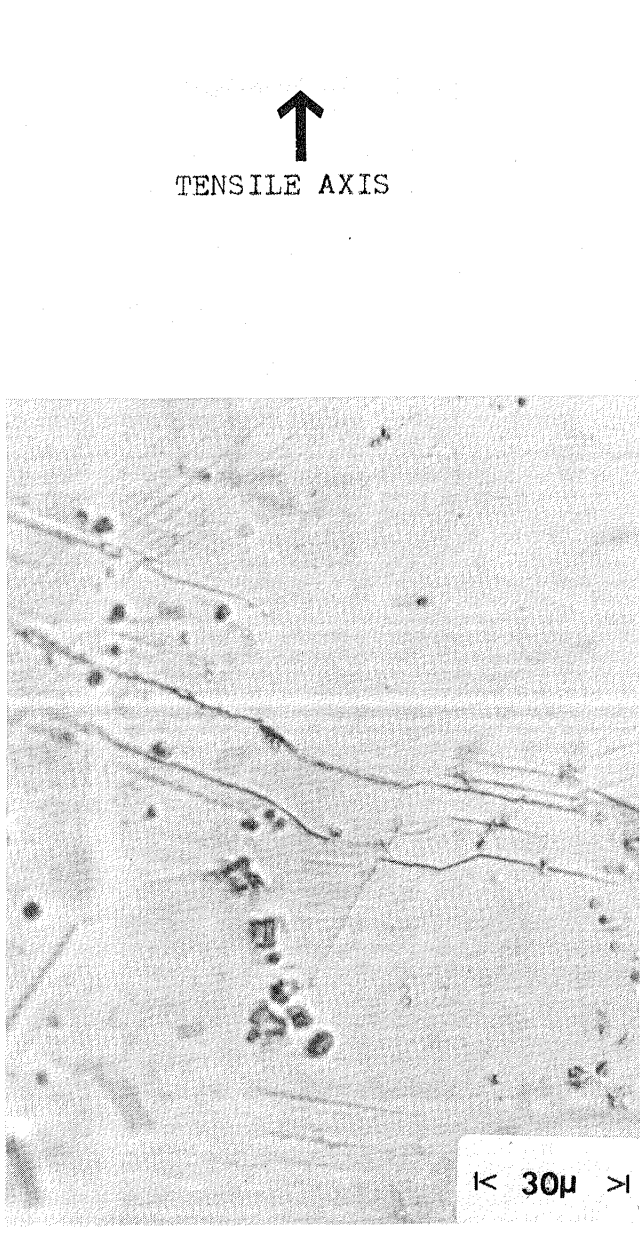

Figure 47 Coarse grained small γ' specimen N_i 2 ($\Delta\varepsilon_p = 0.15\%$). Slip band cracking was evident at 12000 cycles.

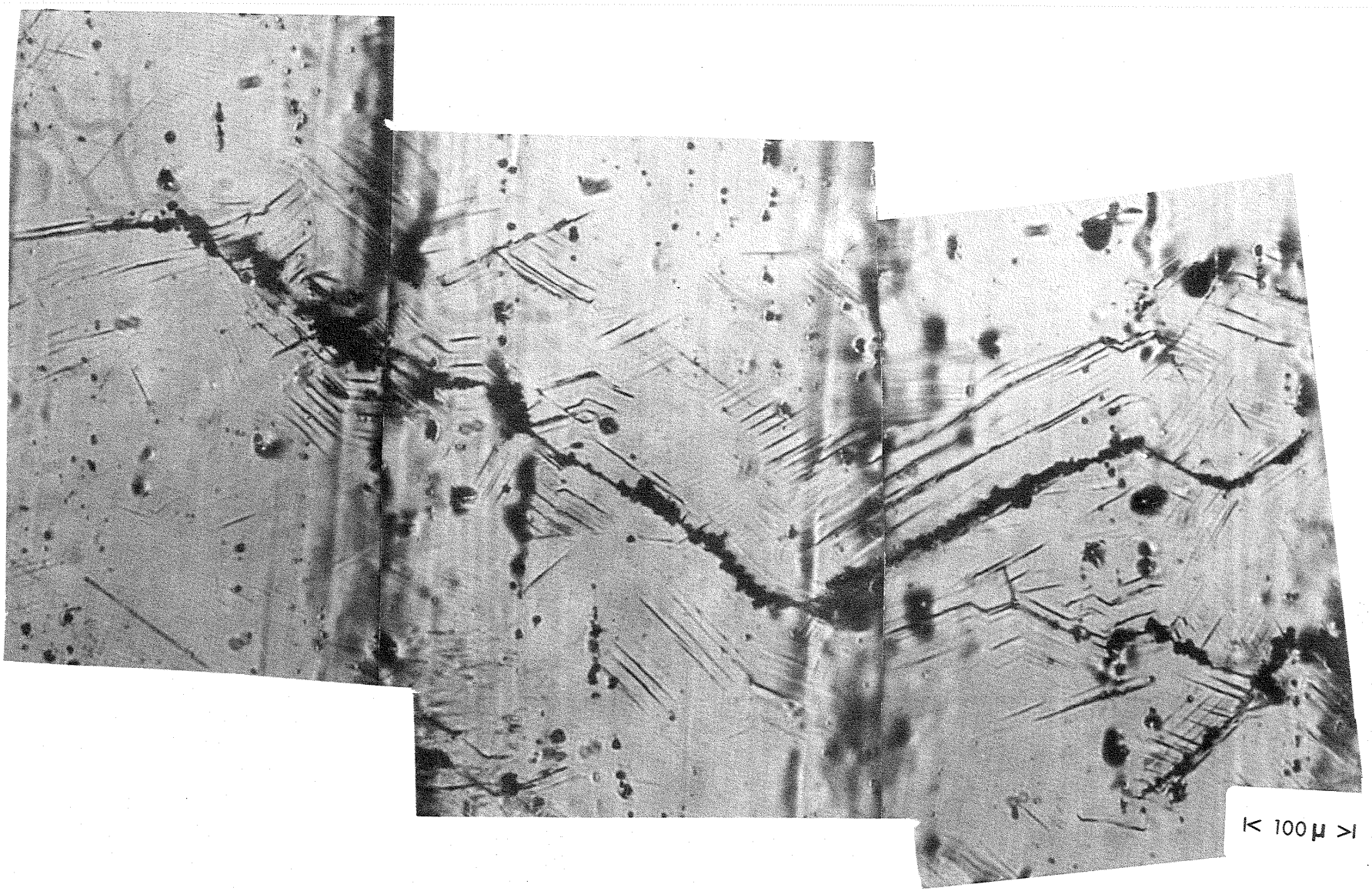

Figure 48 Coarse grained small γ' specimen N. 2($\Delta\varepsilon_p$=0.15%) showed cracking at cycle 27940(2/3 of the life). Crack length was ~ 1100μ.

TENSILE AXIS

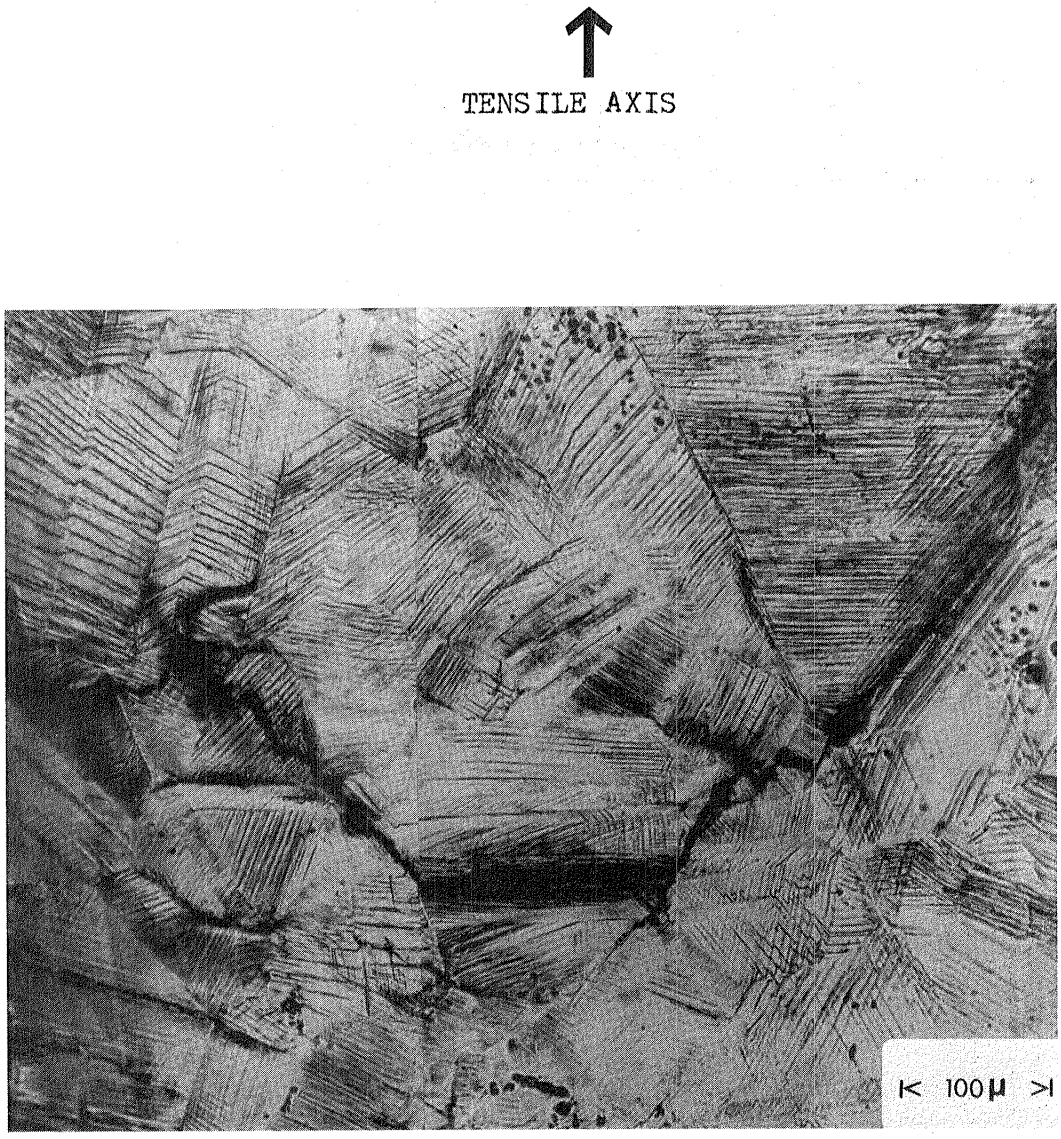

Figure 49 Slip band cracking in the coarse grained small γ' specimen N_i 3($\Delta\varepsilon_p$ = 3.00%) after 640 cycles(90% of the total life). Crack length was ~500 μ.

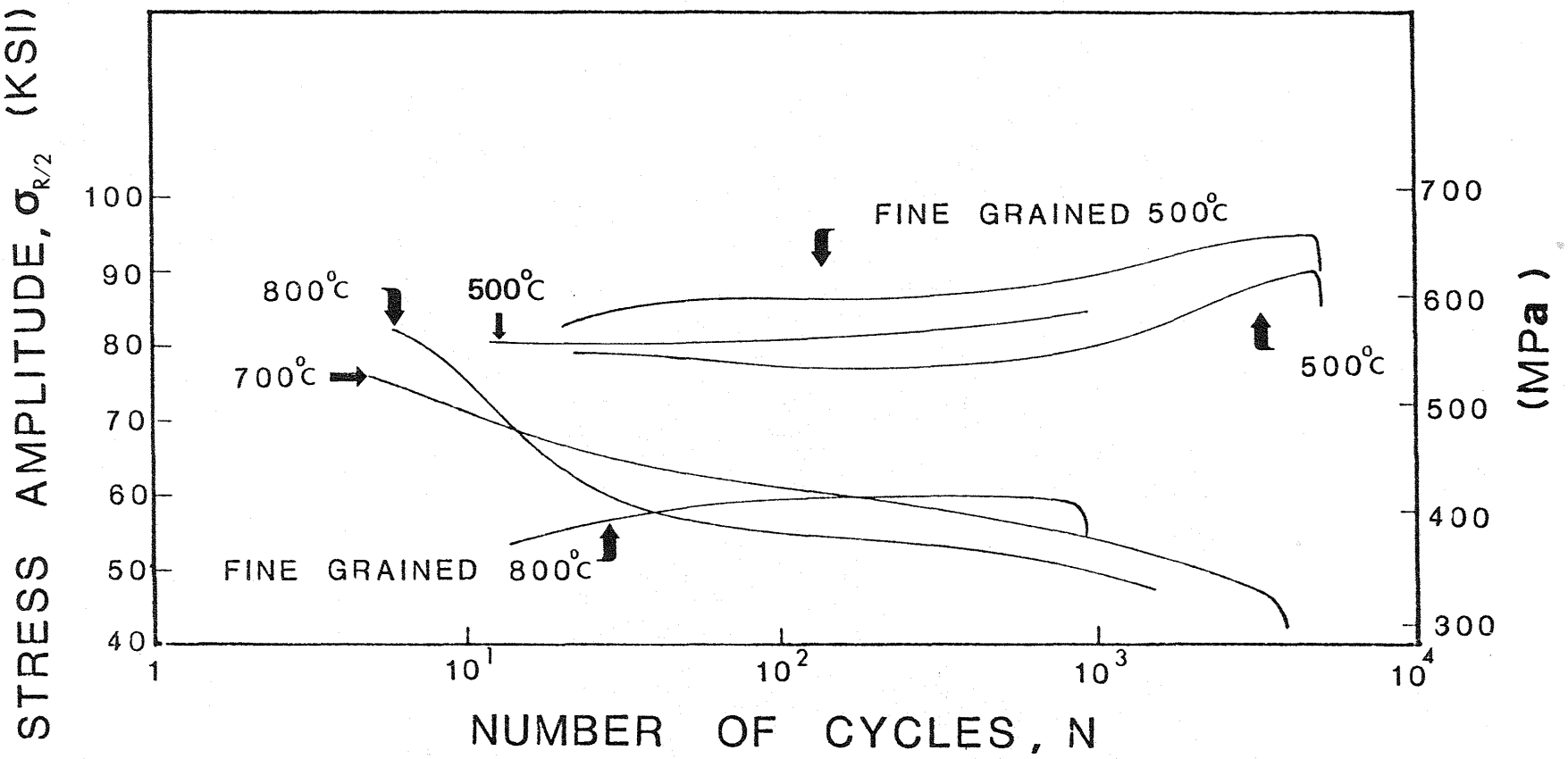

Figure 50 Cumulative glide plots for elevated temperature LCF tests ($\Delta\varepsilon_p$=0.30%). Notice continual hardening for tests at 500 C. Curves are for coarse grained small γ' specimens unless otherwise indicated.

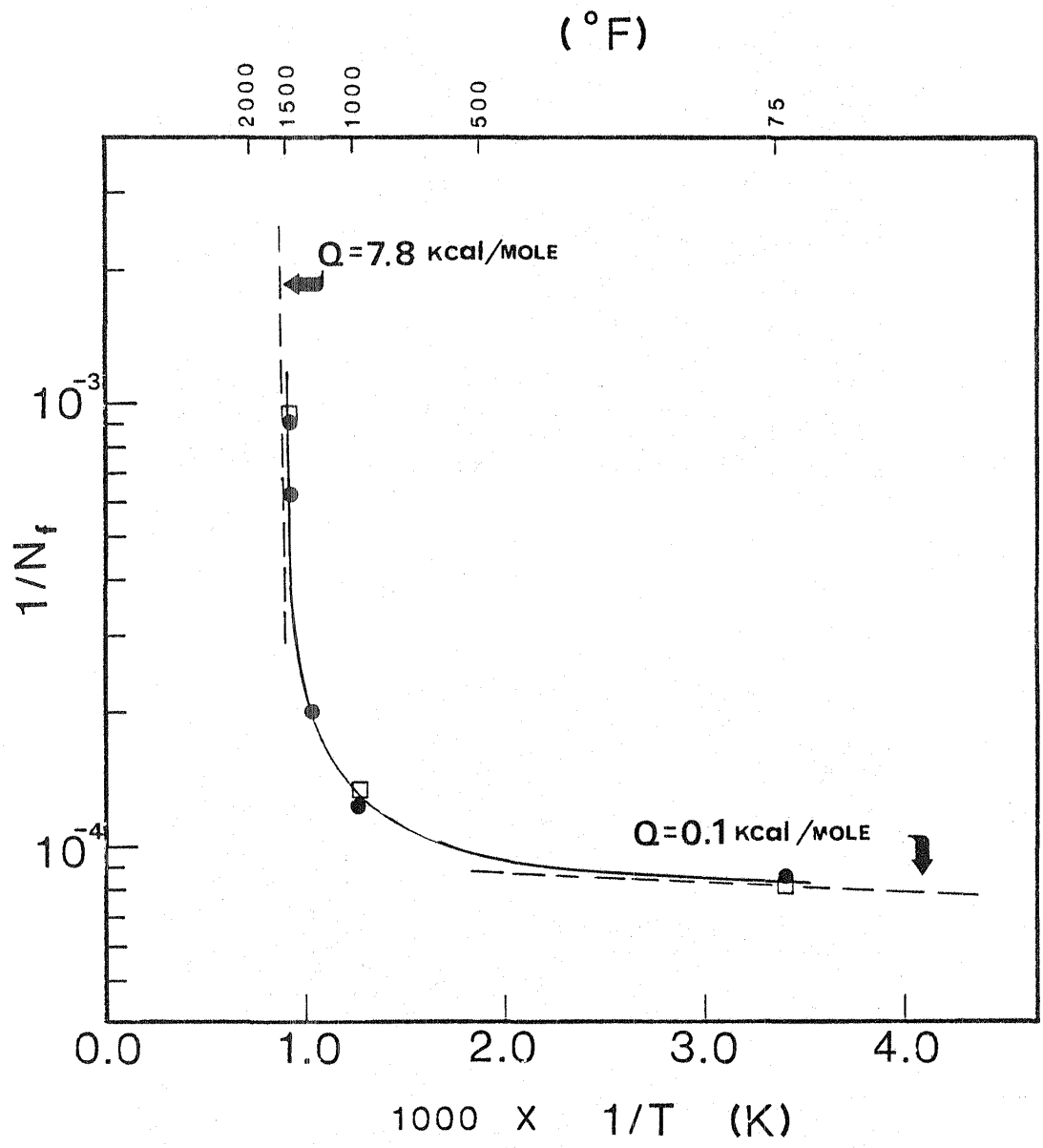

Figure 51 $1/N_f$ Vs. 1/T for LCF data. The slope of the curve is proportional to the experimental activation energy,Q. Q=7.8KCal/M corresponds to specimens exhibiting intergranular cracking. Dots are coarse grained small γ'specimens.

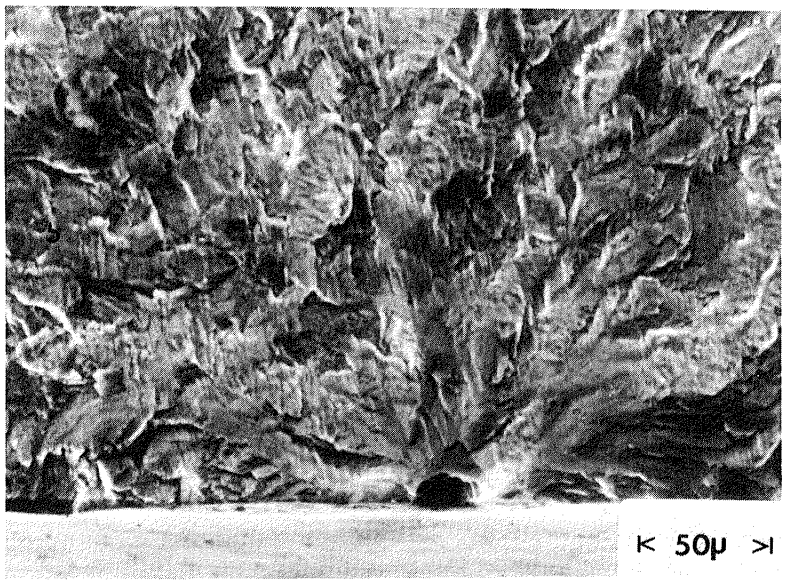

(a)

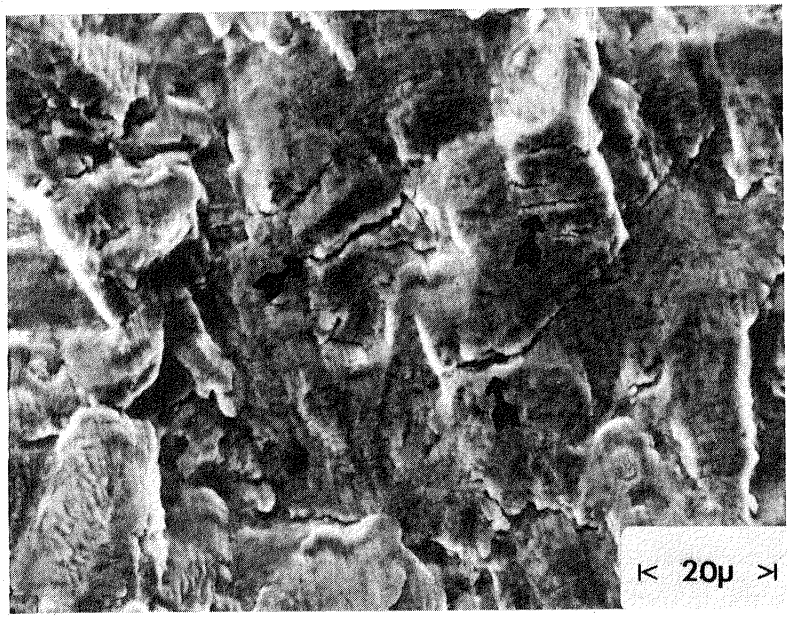

Crack growth direction

(b)

Figure 52 Fine grained large γ' specimen 21, tested at 500 C. a) Transgranular initiation. b) Propagation by a striated mechanism. Arrows indicate secondary cracking forming along the striations.

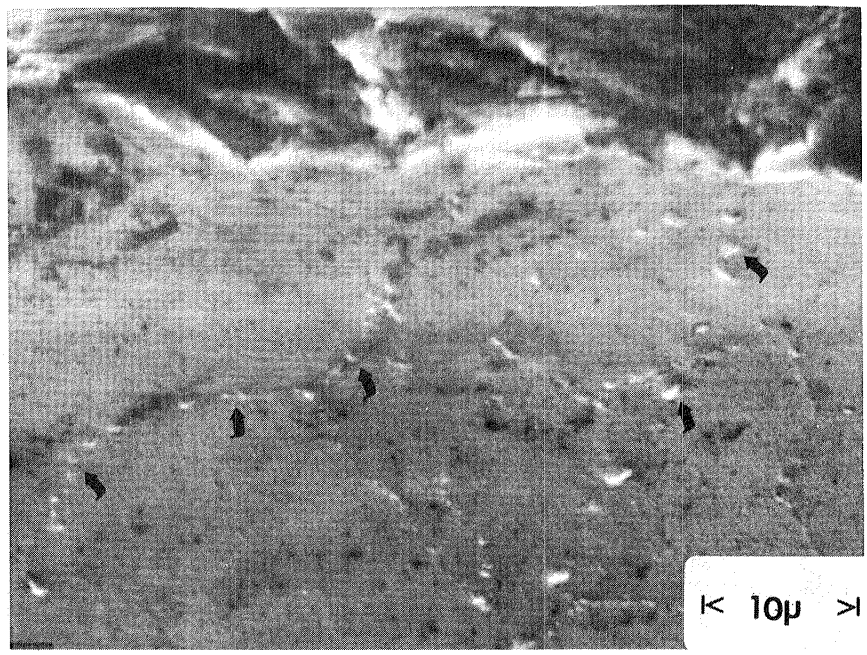

Figure 53 Gauge surface of fine grained large γ' specimen 21(500 C). Arrows indicate preferential oxidation around grain boundary carbides.

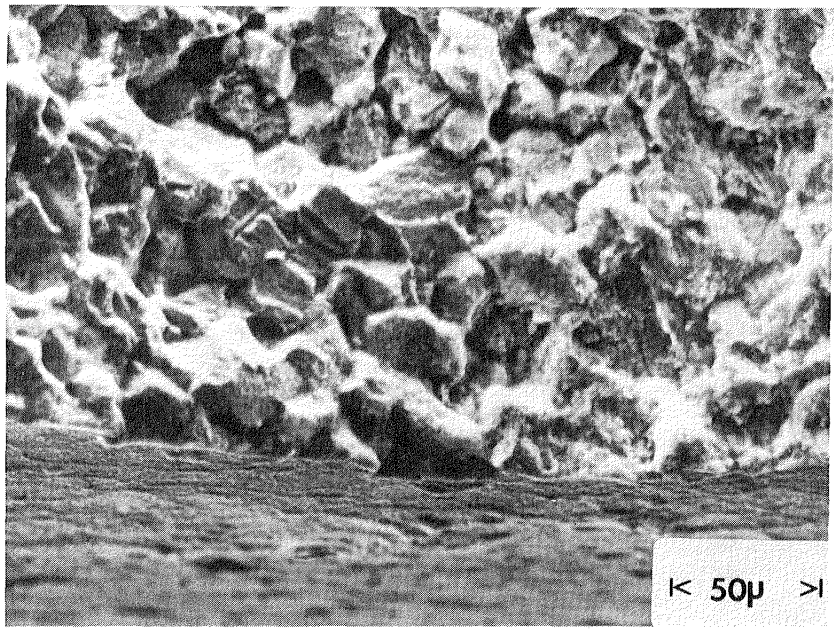

(a)

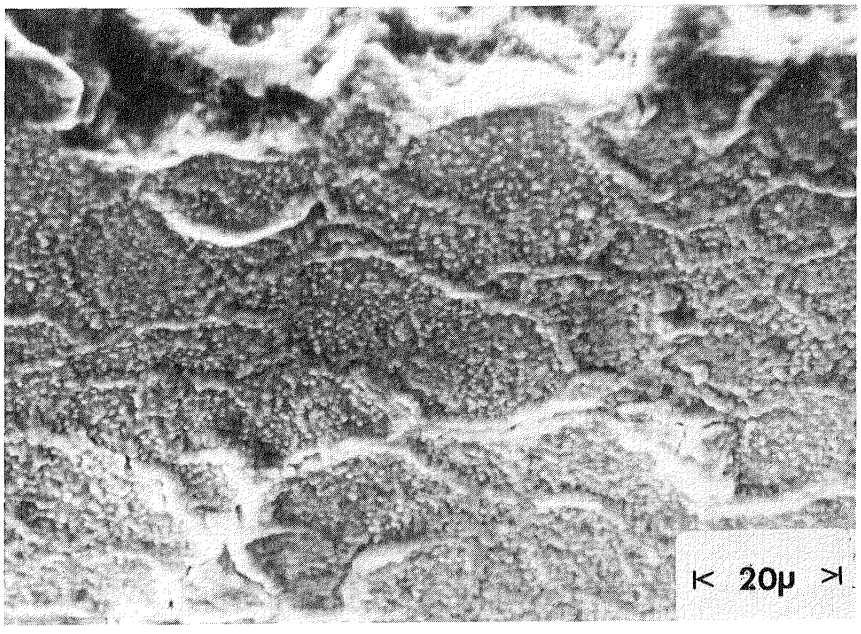

(b)

Figure 54 Fine grained large γ' specimen 22, tested at 800 C. a) Heavily oxidized fracture surface indicates intergranular initiation and propagation. b) Oxidized gauge surface of Spec. 22. Heavy grain boundary oxidation created raised areas(ridges) at the boundaries. The interiors of the grains are oxidized as indicated by the 'orange peel' type surface.

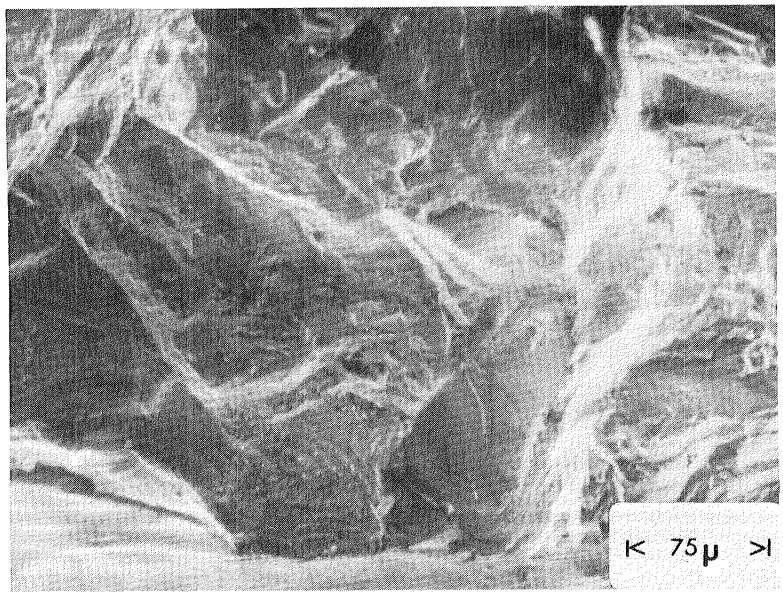

(a)

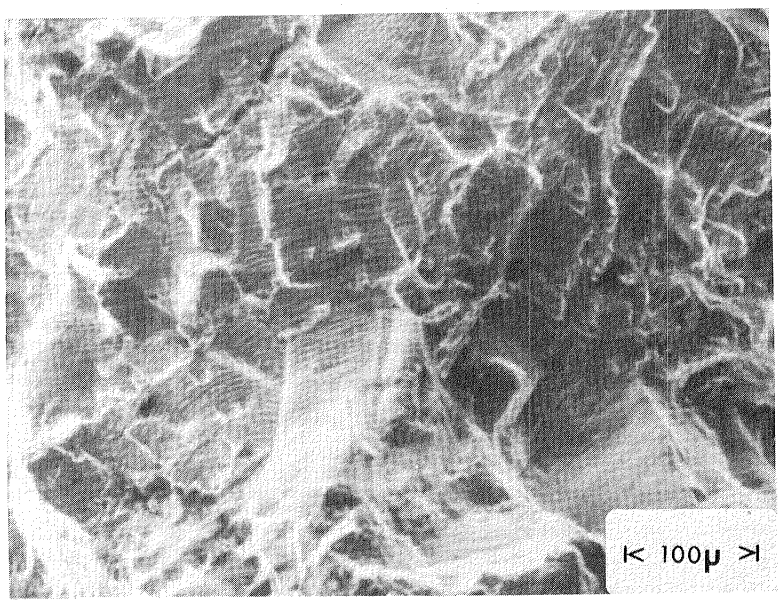

Crack growth direction

(b)

Figure 55 Coarse grained small γ' specimen 20, tested at 500 C. Transgranular initiation(a) is observed with some cleavage. Propagation occured by a well-defined striation forming mechanism(b). This is similar to what was observed by Lawless [71] and others for FCP room temperature tests.

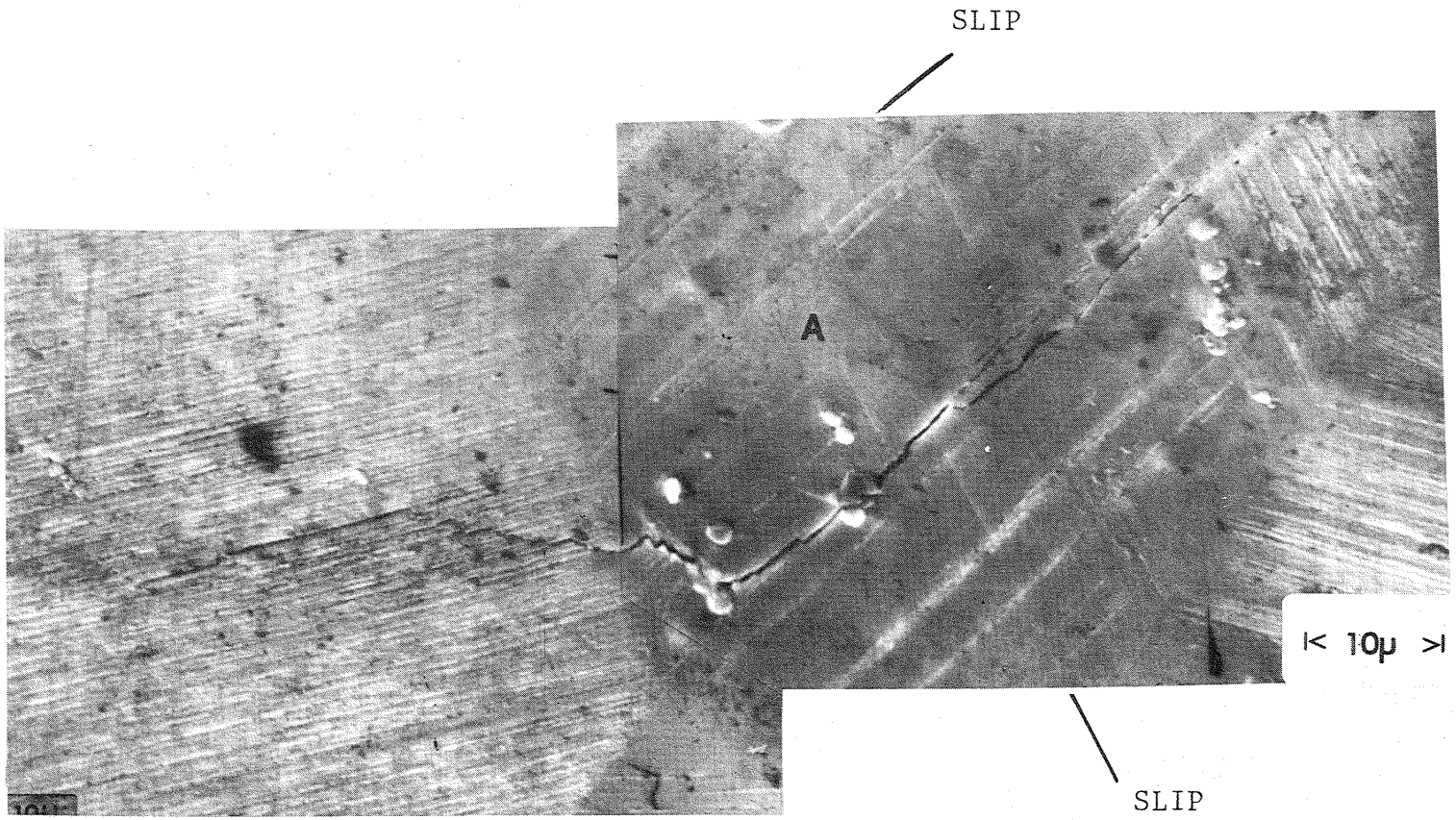

Figure 56 Gauge surface of coarse grained small γ' specimen 20, tested at 500 C. Heavy slip band activity and slip band cracking is observed. Grain 'A' shows that multiple slip systems were operative.

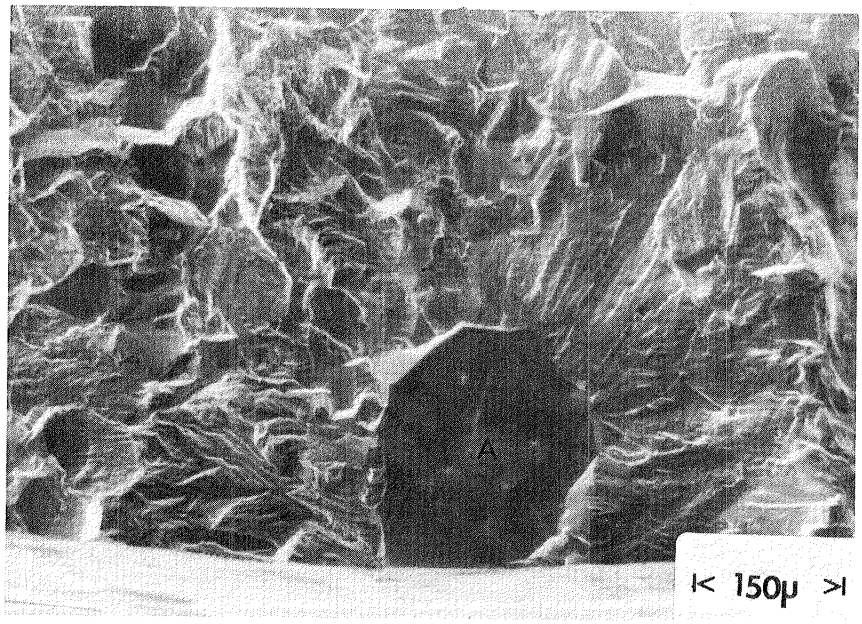

(a)

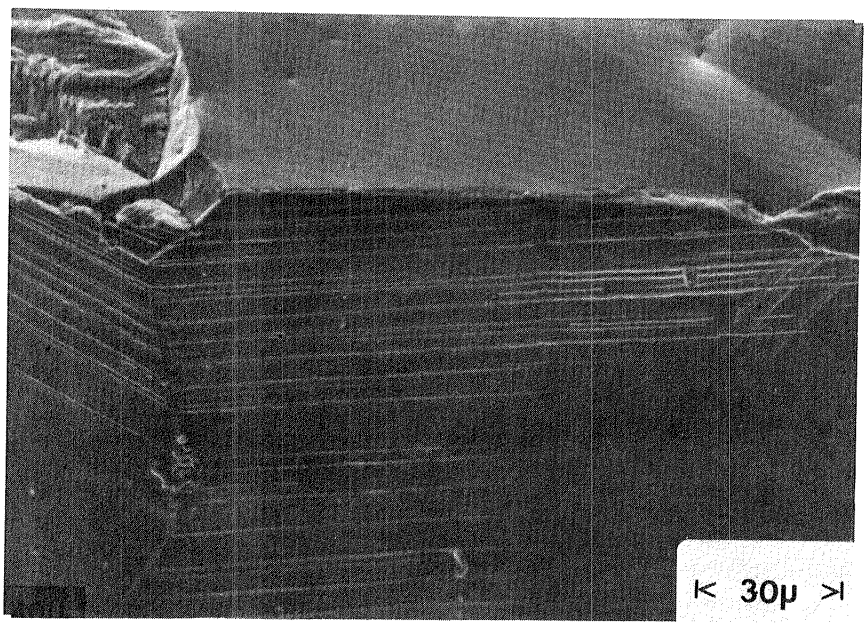

(b)

Figure 57 Transgranular initiation in coarse grained small γ' specimen 24, tested at 700 C. a) Area 'A' is a facet with cleavage fractures radiating from it. b) Gauge surface under the facet indicating oxidized slip bands and a grain boundary.

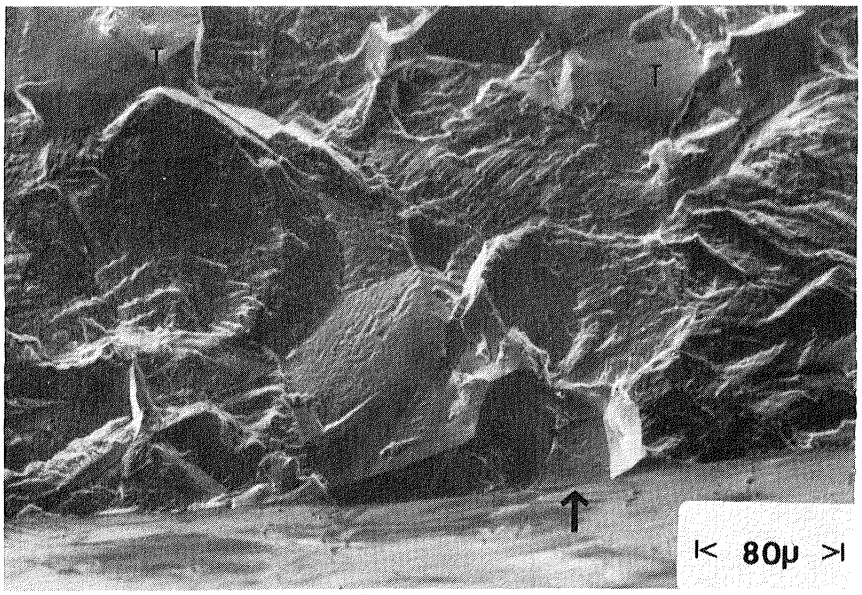

(a)

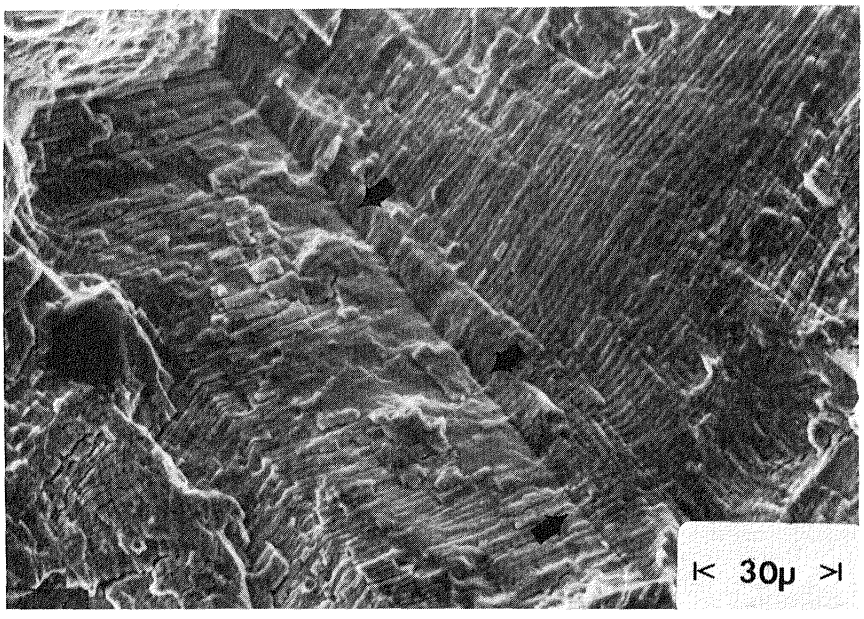

(b)

Figure 58 Coarse grained small γ' specimen 24(700 C). a) Intergranular initiation(arrows) and areas of intergranular and facet propagation('T'). b) Striated propagation mechanism. Note the twin boundary(arrows).

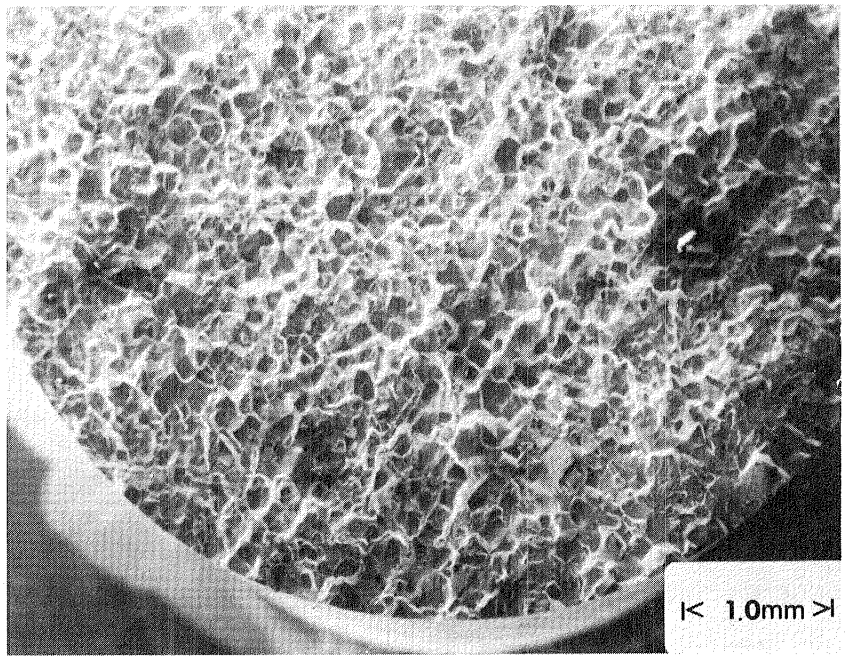

(a)

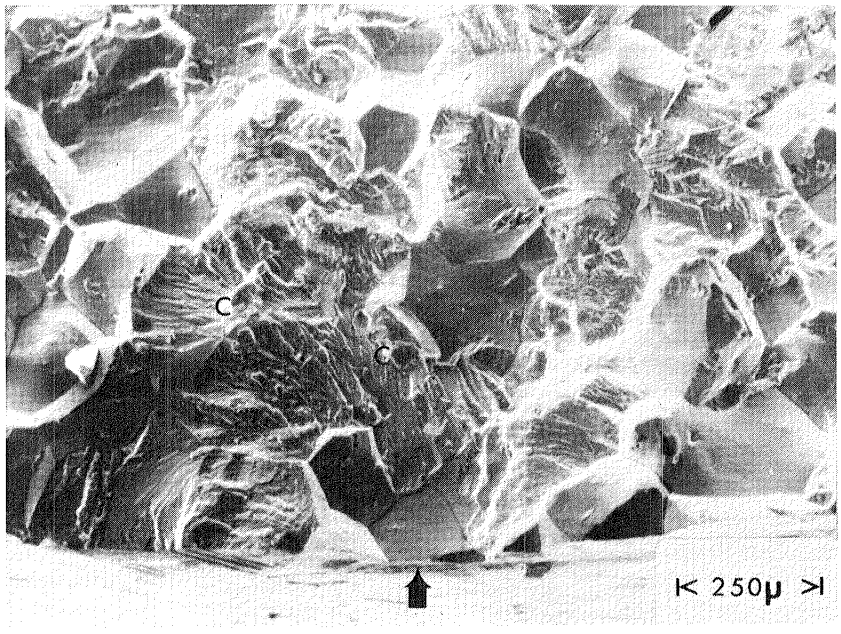

(b)

Figure 59 Fracture surface(a) of coarse grained small γ' specimen 23, tested at 800 C. b) Intergranular initiation(arrow) of spec. 23. Transgranular cleavage is also observed('C').

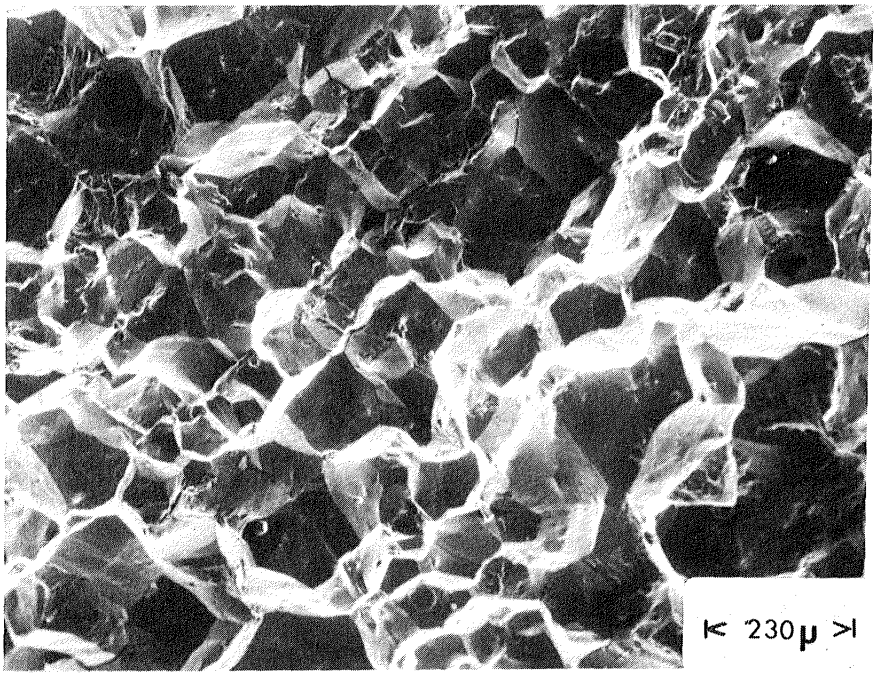

Figure 60 Intergranular propagation of specimen 23 (coarse grained small γ').

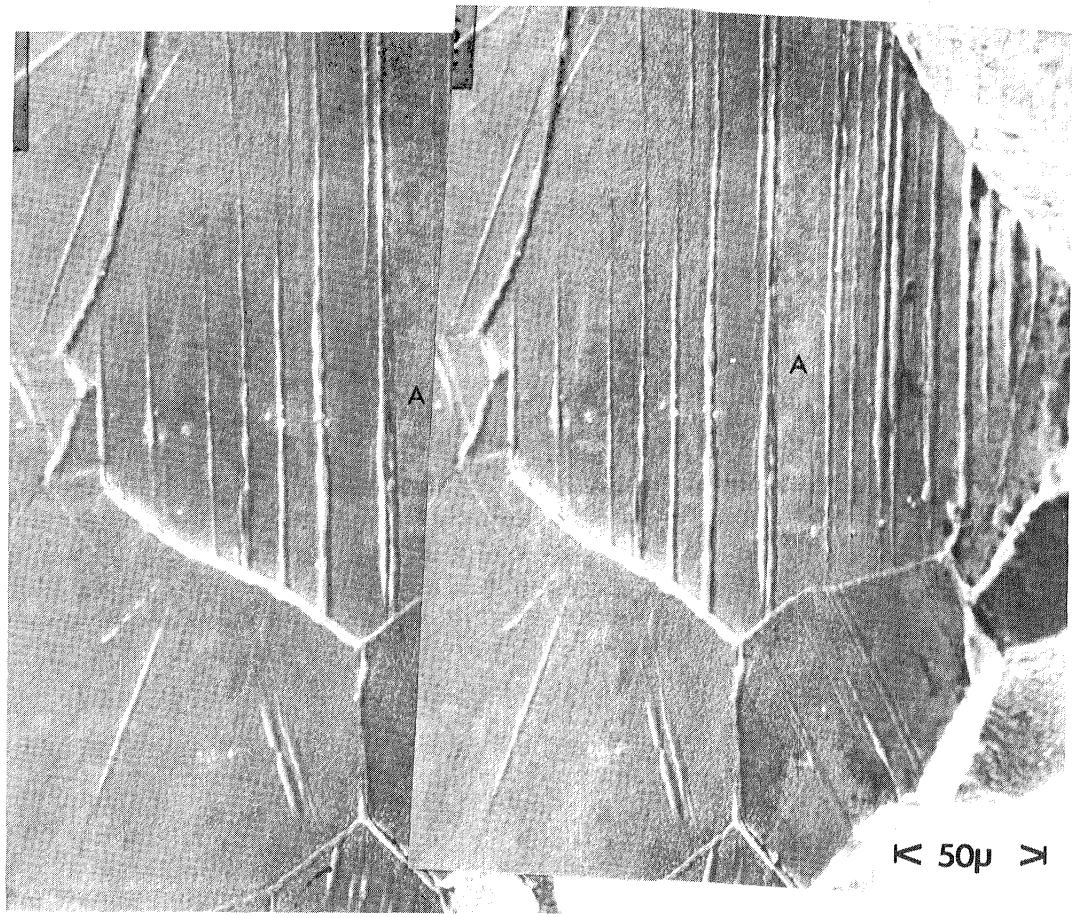

Figure 61 Stereo-pair of coarse grained small γ' specimen 23(800 C). Oxidized slip bands and grain boundaries formed ridges. Grain 'A' is offset to a lower level due to the high stresses at the fracture surface.

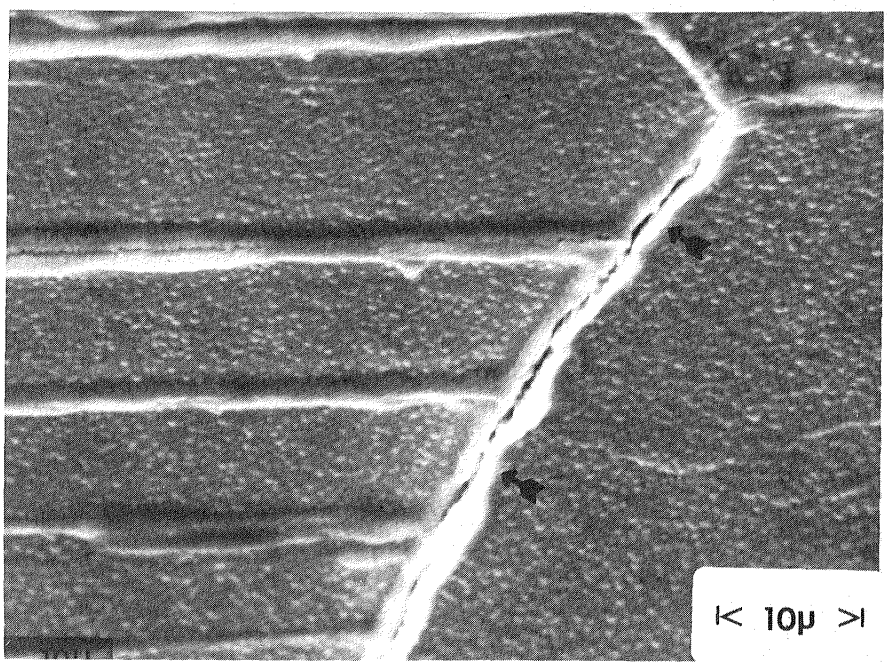

Figure 62 Gauge surface of coarse grained small γ' specimen 23(800 C). Slip bands intersecting an oxidized grain boundary induced cracking(arrows).

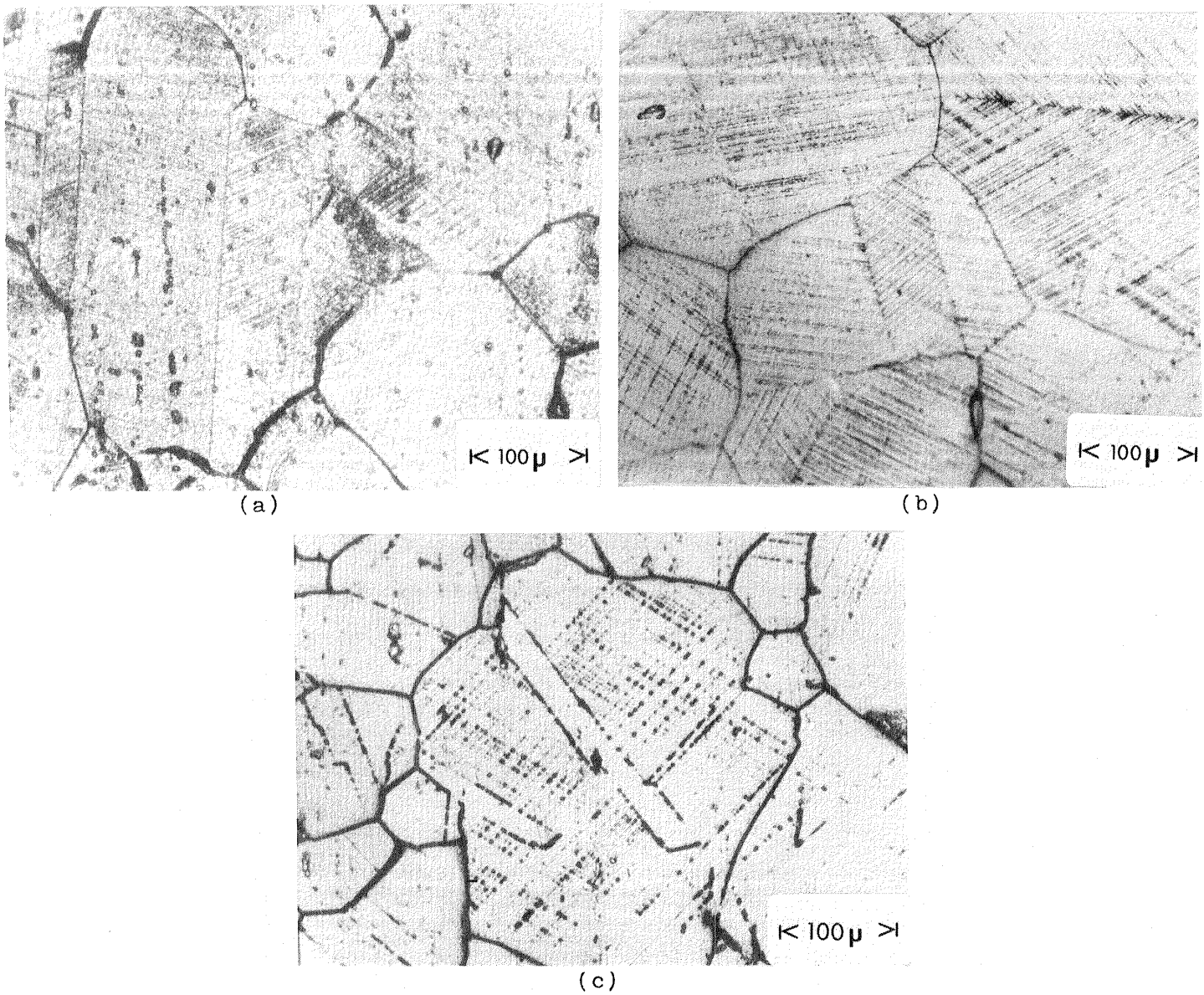

(a) (b) (c)

Figure 63 Optical micrographs showing slip band activity for coarse grained small γ′ specimens tested at a) 500 C b) 700 C and c) 800 C. Slip bands are not as clear as in the room temperature specimens(Fig.29).

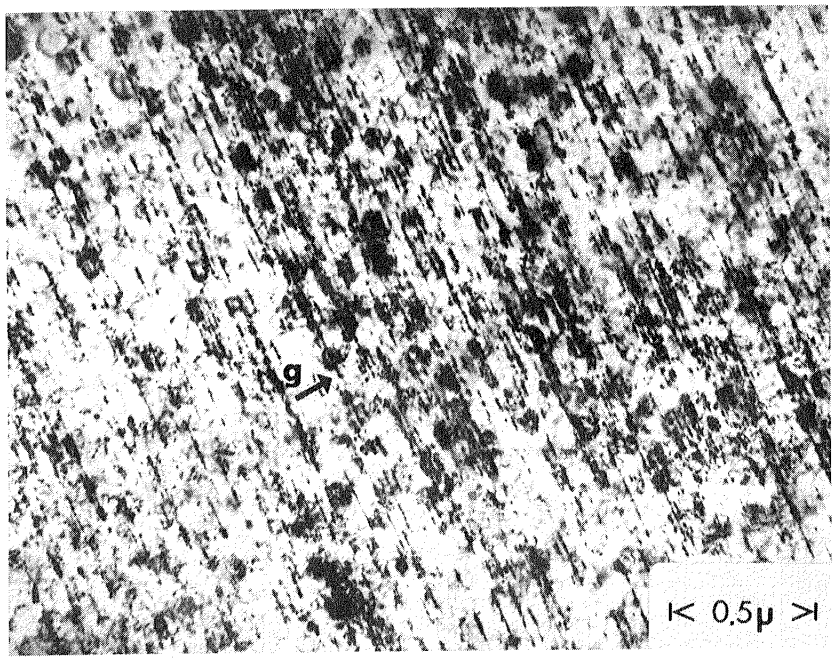

S.F.=0.32

(a)

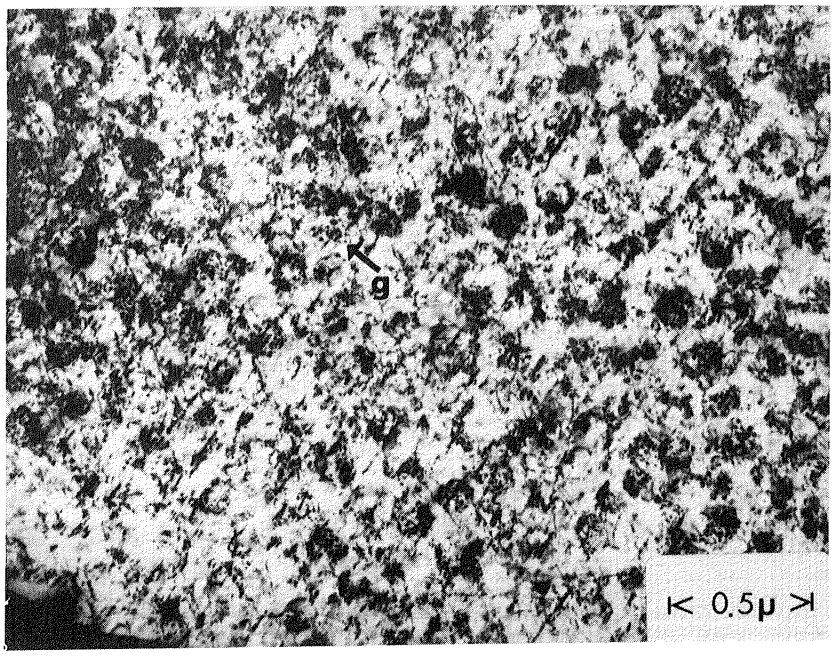

S.F.=0.35

(b)

Figure 64 Fine grained large γ' specimen 21(500 C). Dense deformation structure is observed. This grain has at least two slip systems in operation, one of each in the edge-on condition(a and b, g= { 111 }).

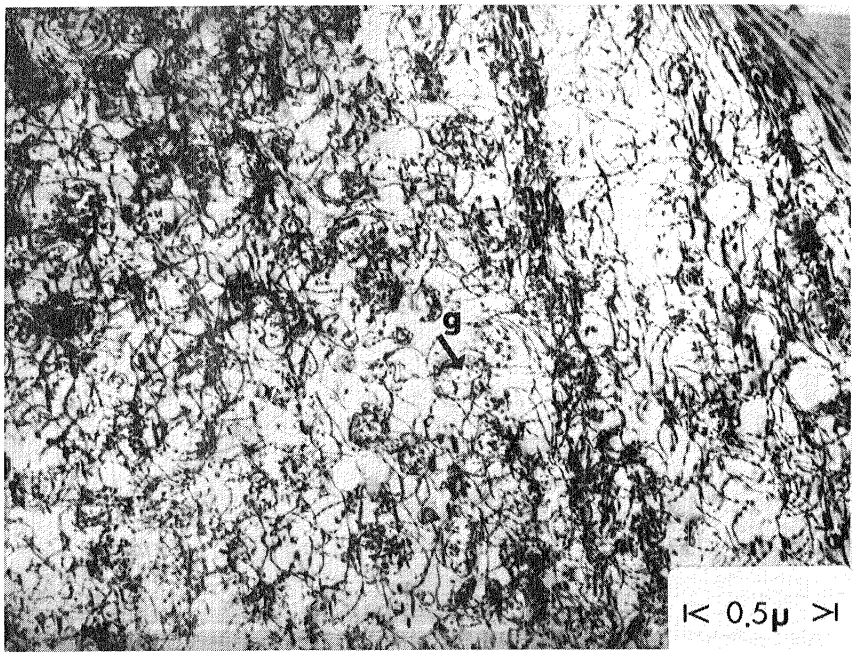

(a)

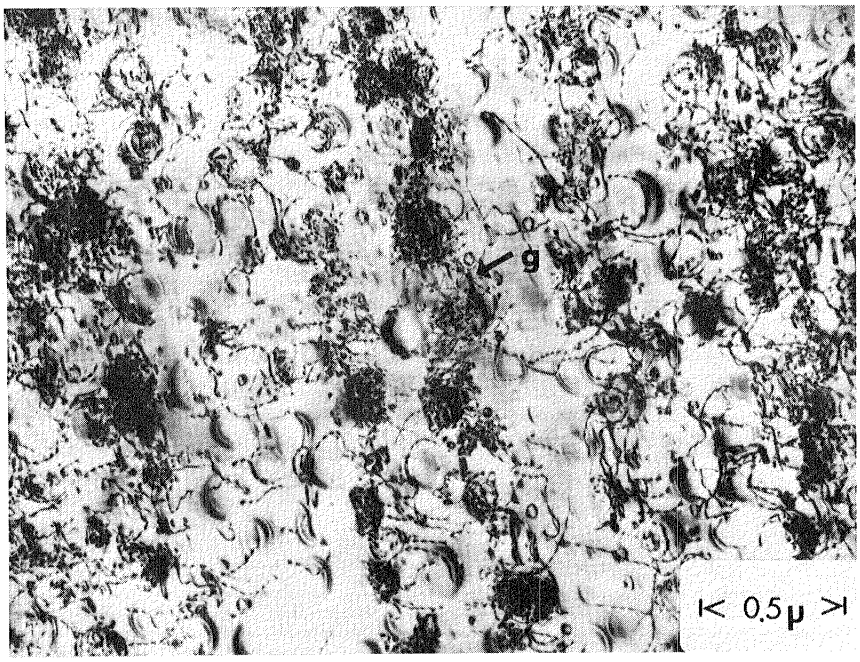

(b)

Figure 65 Fine grained large γ' specimen 21(500 C). Looping and bowing mechanisms for a) {111} reflection and b){ 200 }reflection.

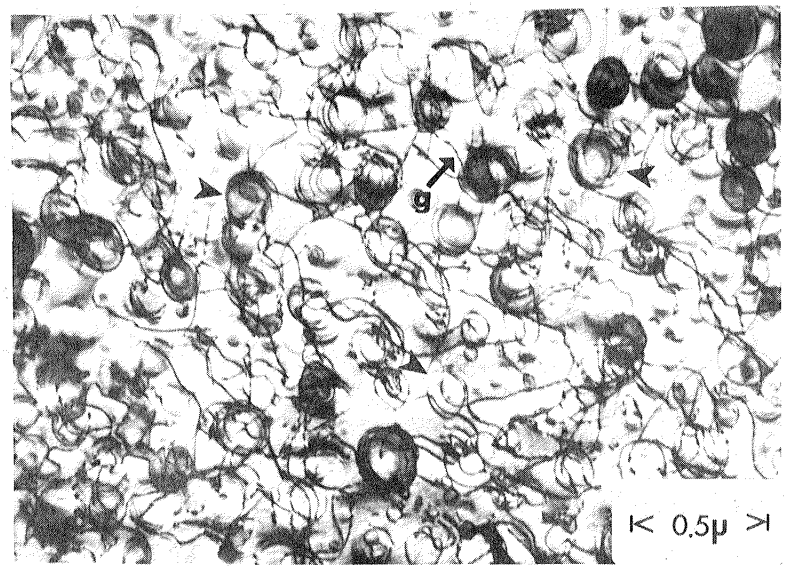

(a)

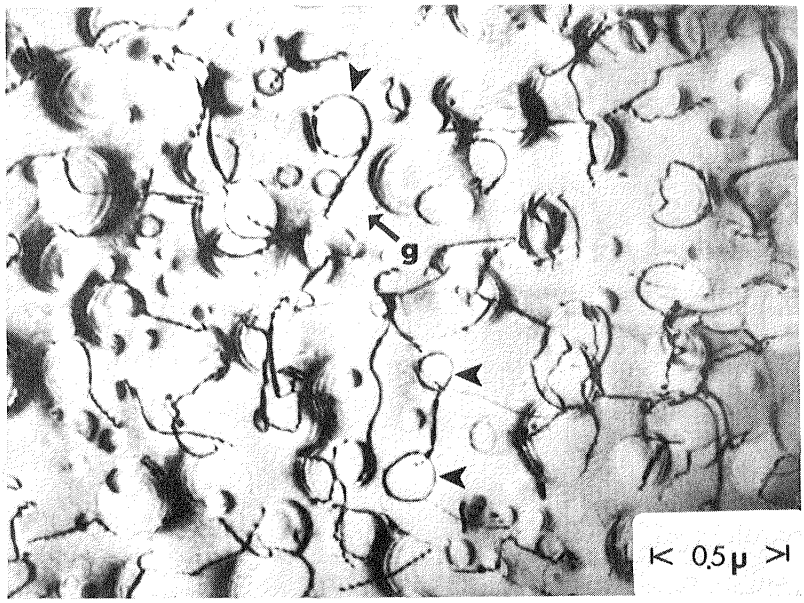

(b)

Figure 66 Deformation structures of the fine grained large specimen 22(800 C). No slip bands were observed. Arrows indicate some residual dislocation loops left around the precipitates in two different grains(g= {111}).

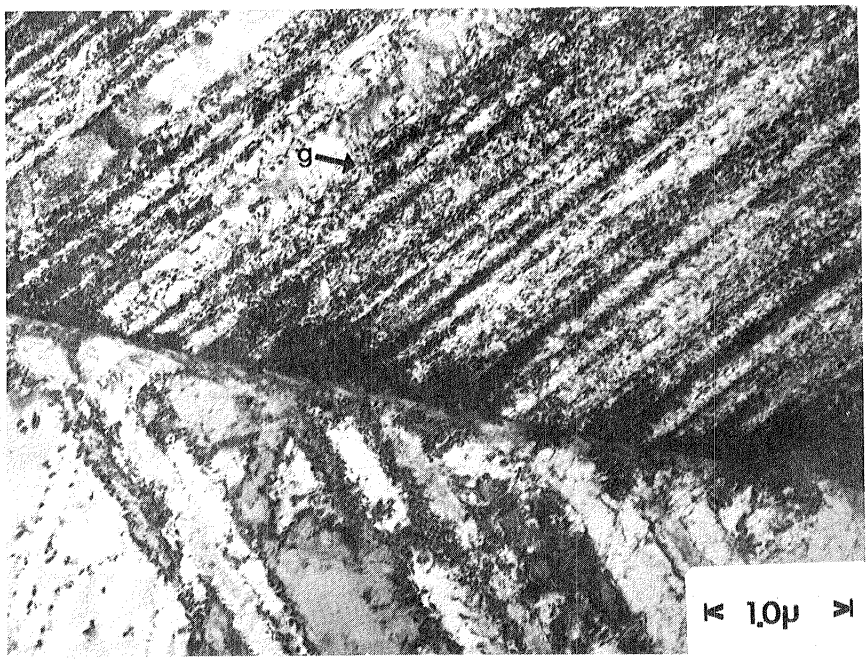

(a)

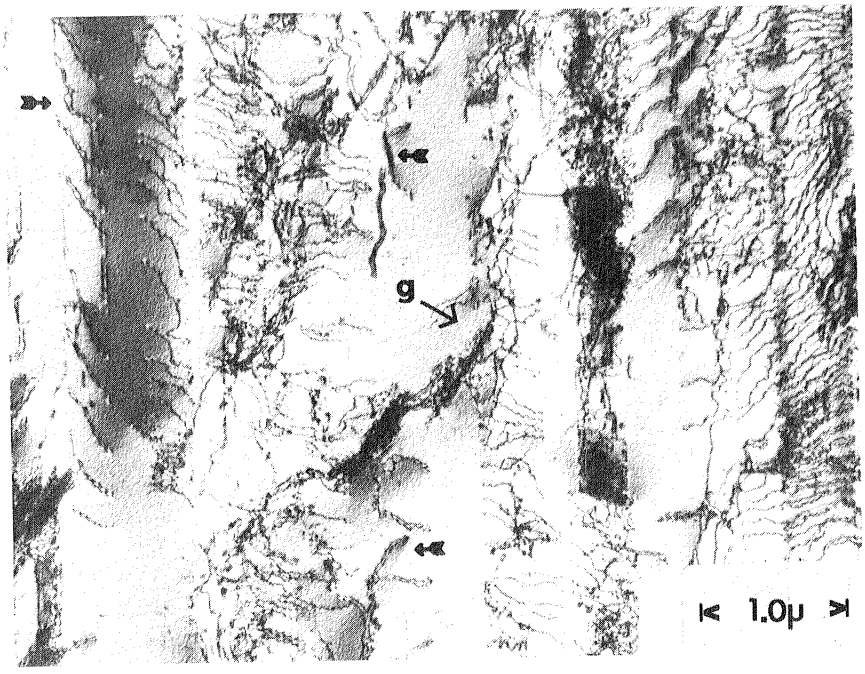

(b)

Figure 67 Slip bands in coarse grained small γ' specimen 20 tested at 500 C. Note the high density of bands(a) g= {111}. b) Dislocation structure within the slip bands. Arrows indicate dislocation pairs g={200}

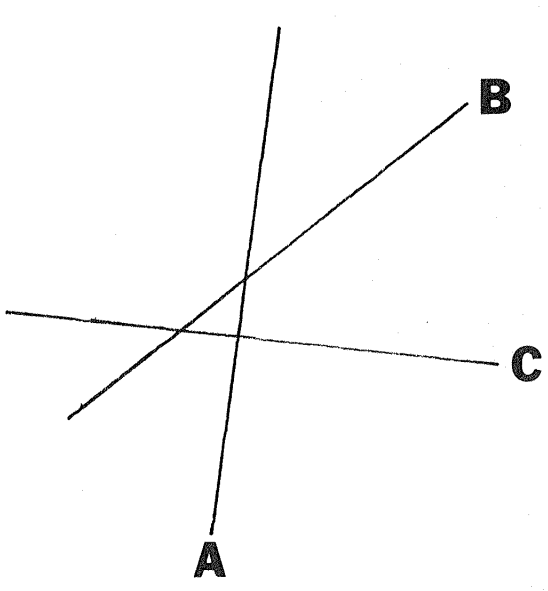

(a)

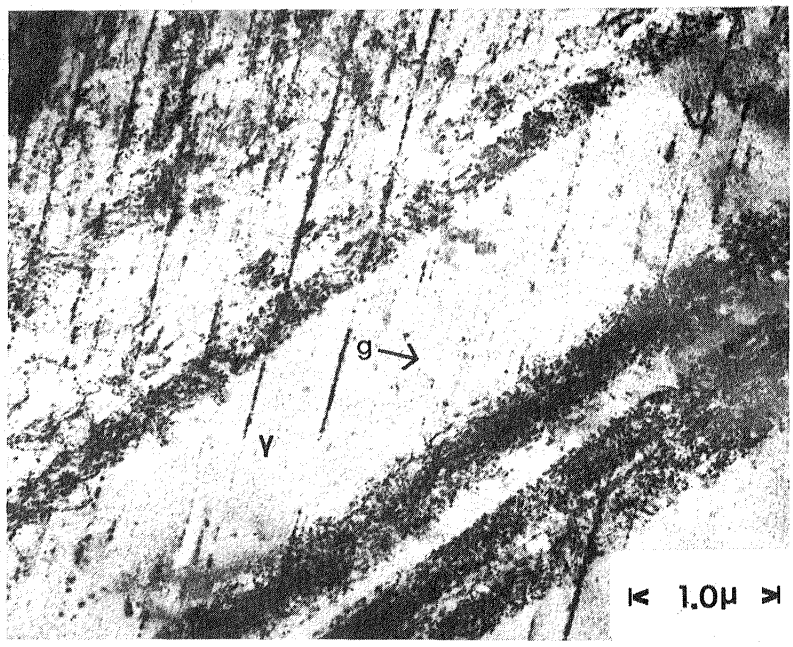

(b)

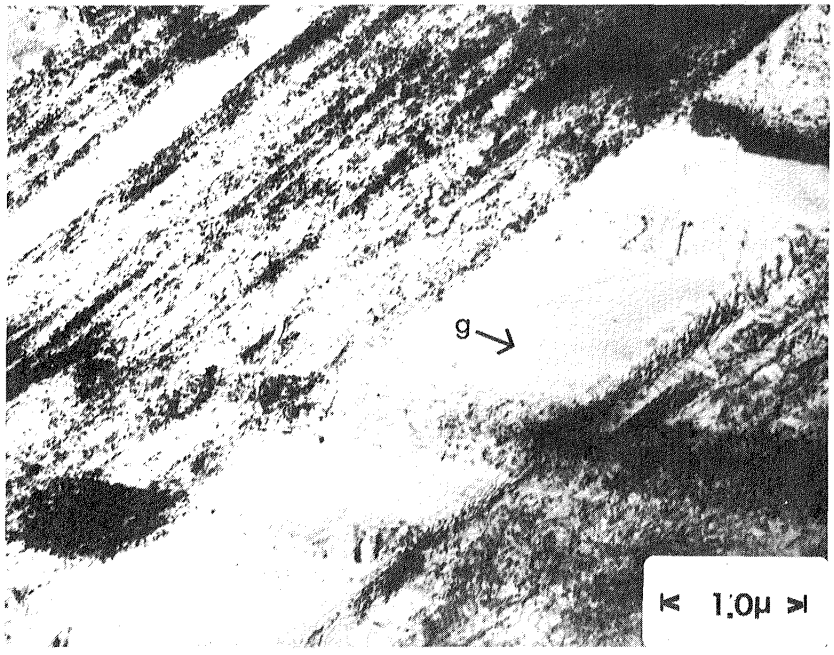

(c)

Figure 68 Slip bands in coarse grained small γ' specimen 20(500 C). a) Schematic of three slip systems within the grain. Plane 'A' was edge on(b) and has a Schmid factor of 0.41. Plane 'B' and 'C' has a Schmid factor of 0.50 and 0.44 respectively.

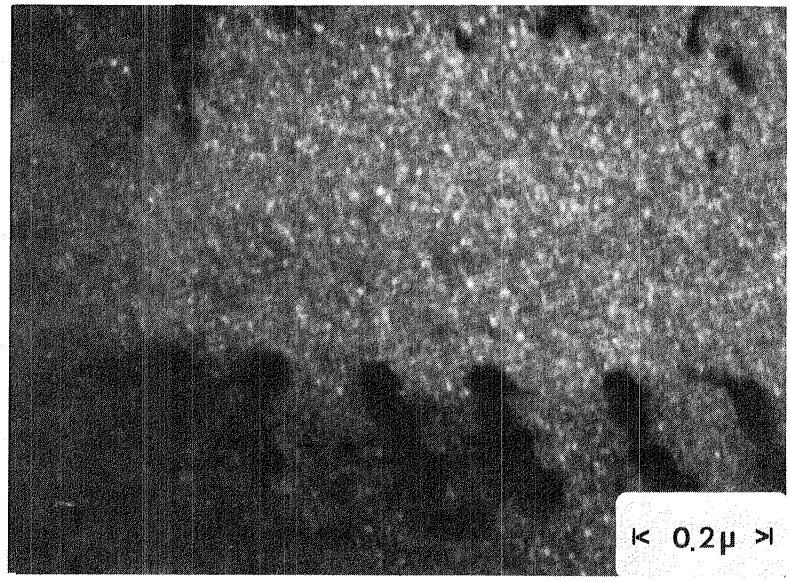

(a)

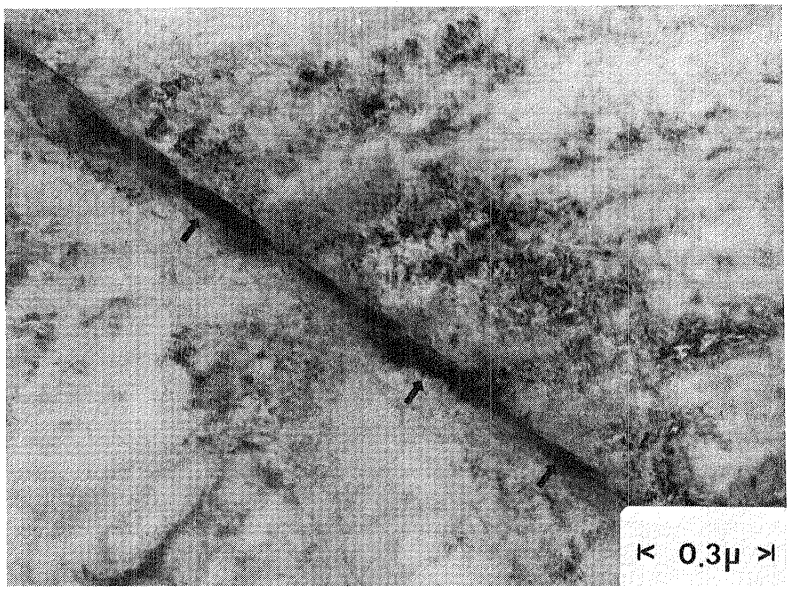

(b)

Figure 69 Coarse grain small γ' specimen 20(500 C). a) Dark field({300} reflection) indicates γ' coarsening to 90-120Å diameters. b) Grain boundary showing carbide precipitation(arrows). Carbides have a plate-like form.

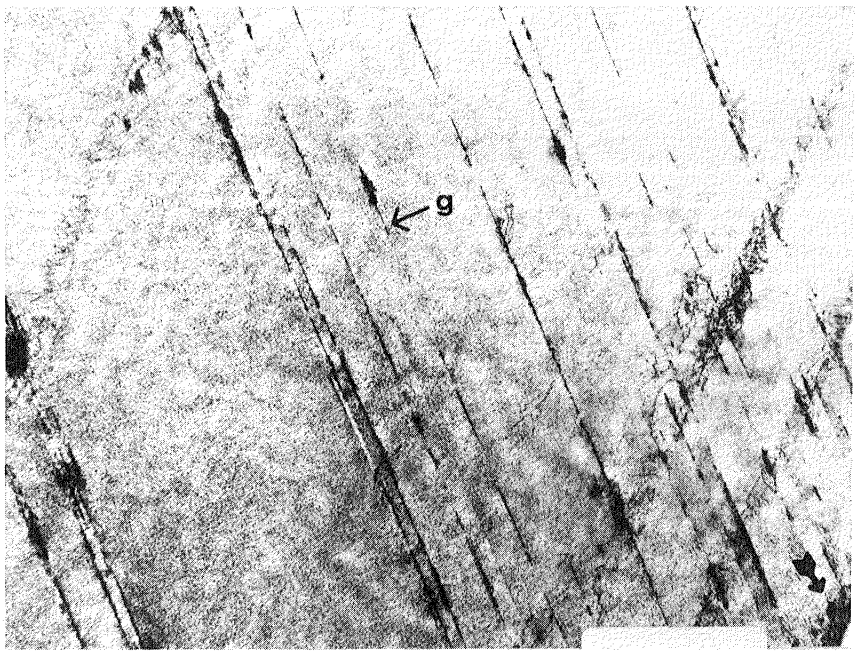

(a)

S.F.=0.35

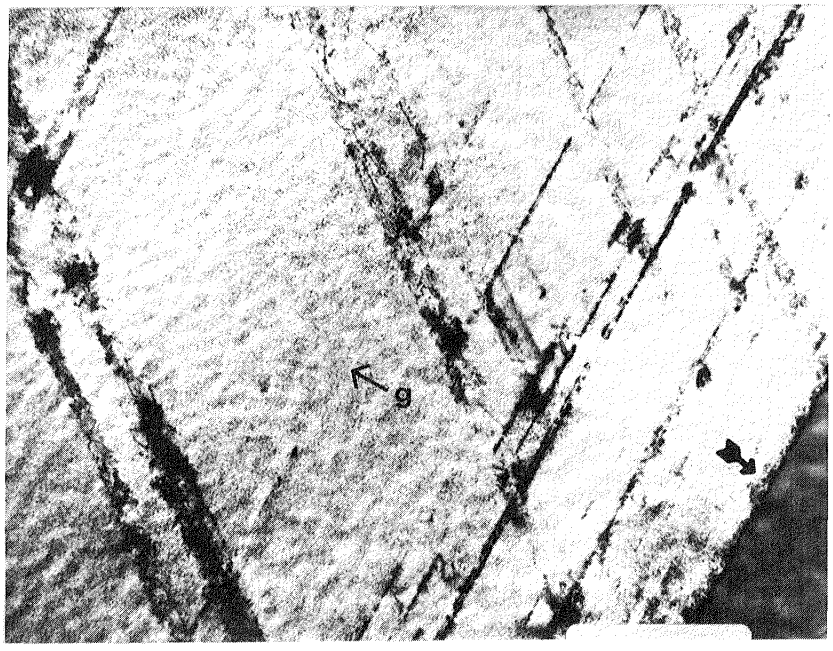

(b)

Figure 70 Coarse grained small γ' specimen 24 tested at 700 C. Multiple slip systems indicate bands a) edge on and b) near edge-on for the same grain. Arrows indicate a grain boundary. g= {111}.

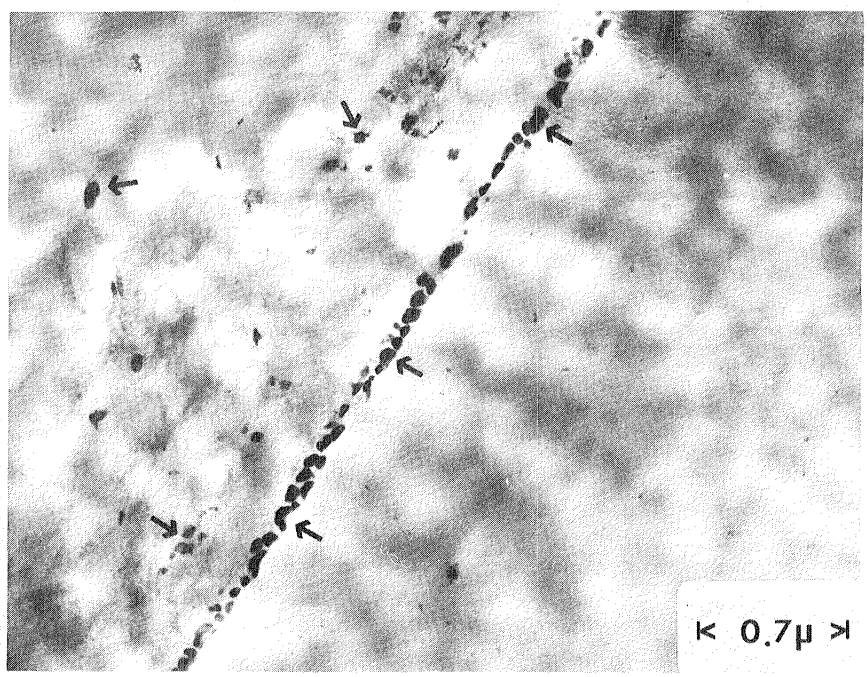

Figure 71 Coarse grained small γ' specimen 24(700 C). Arrows indicate carbide filled grain boundary as well as carbides in the grain interior. The grain boundary was indicated in the previous figure. A diffraction pattern of the carbides is given in the following figure.

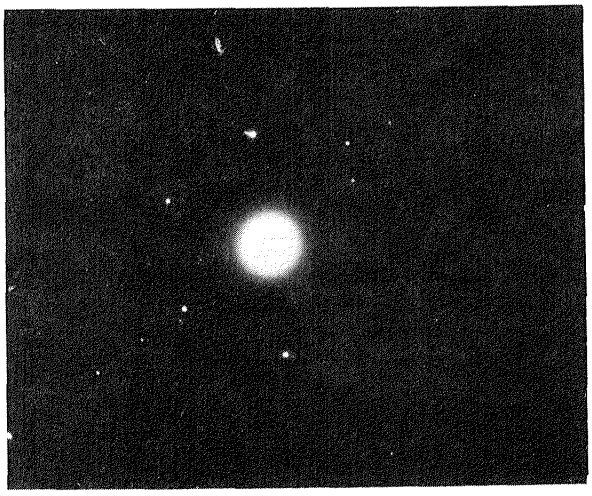

(a)

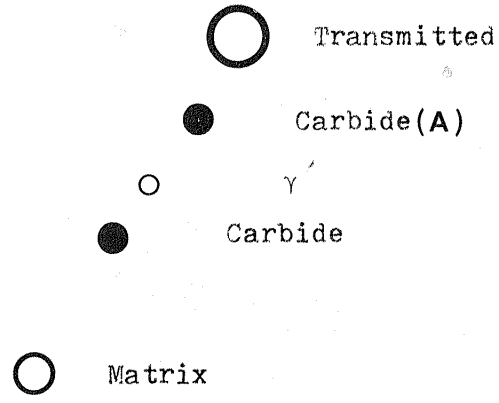

(b)

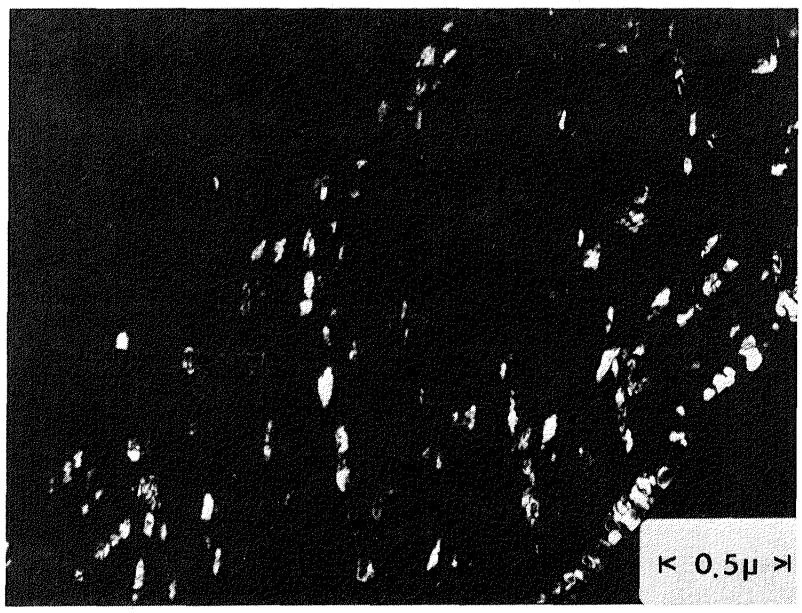

(c)

Figure 72 Coarse grained small γ' specimen 24(700 C). a) Diffraction pattern taken at the grain boundary. Explanation of the spots is given in (b). c) Dark field using carbide reflection 'A'. Arrow indicates the grain boundary. The other carbides are oriented in a manner similar to the slip bands in Fig.70 . Figures 70 thru 72 were taken in the same area.

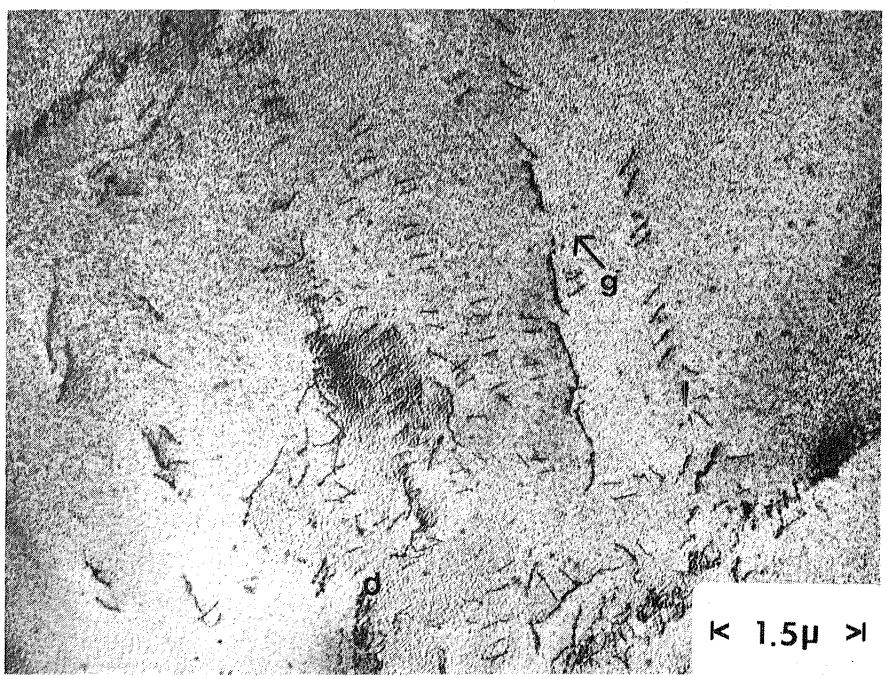

S.F.=0.50

Figure 73 Coarse grained small γ' specimen 23, tested at 800 C. Ill-defined slip bands with loosely packed dislocation structures are observed. The strain contrast from the precipitates appear to be greater than observed in room temperature specimens(Fig. 34) indicating particle coarsening. $g=\{022\}$

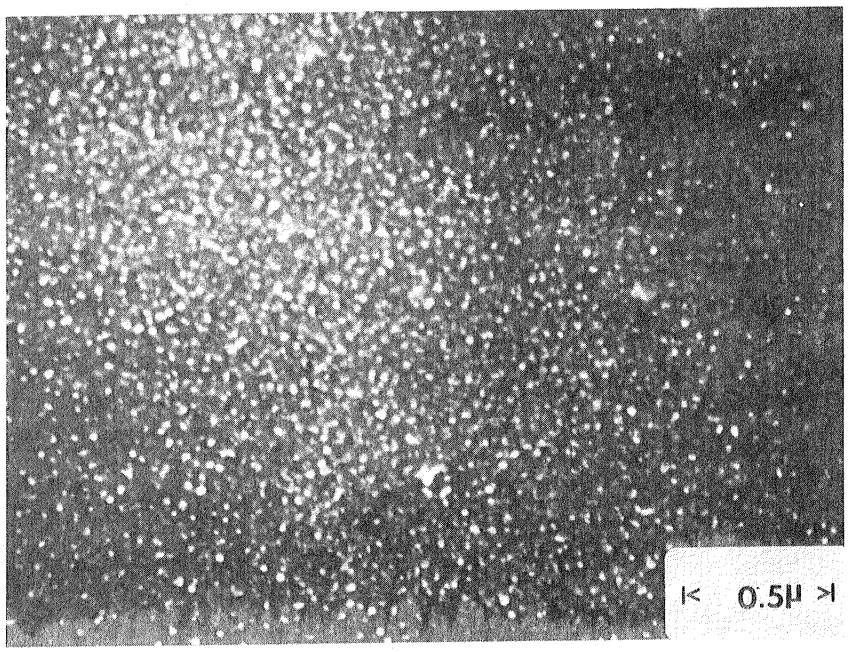

(a)

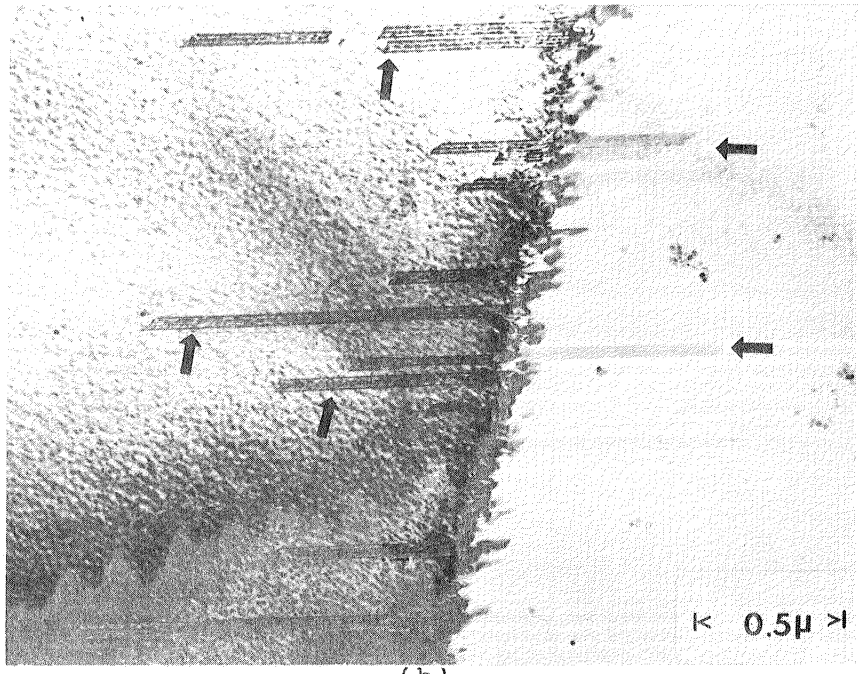

(b)

Figure 74 Coarse grained small γ' specimen 23(800 C). a) Dark field({110 }reflection) of γ' precipitation γ'diameters were ~190Å. b) Carbide precipitation at a twin boundary. Arrows indicate stacking faults.

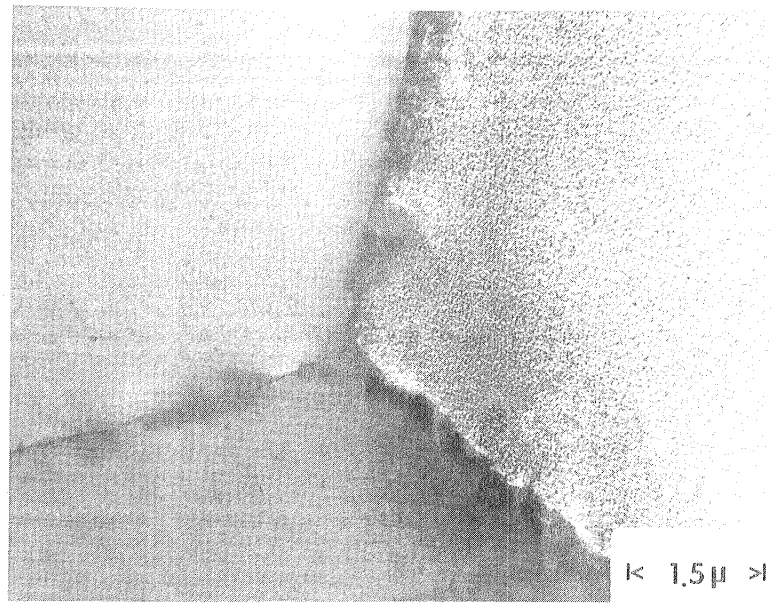

(a)

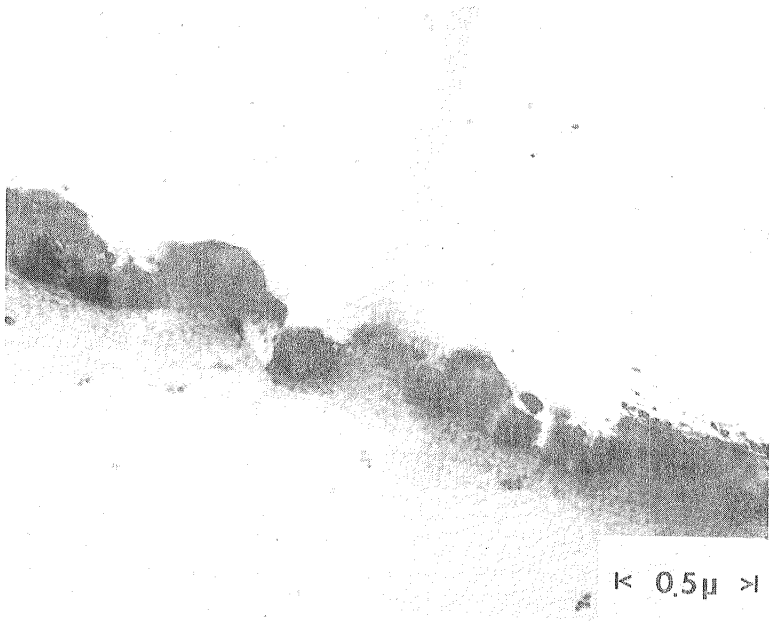

(b)

Figure 75 Coarse grained small γ' specimen 23(800 C). Grain boundary triple point filled with carbides(a). Higher magnification(b) indicates an almost continuous distribution of carbides.

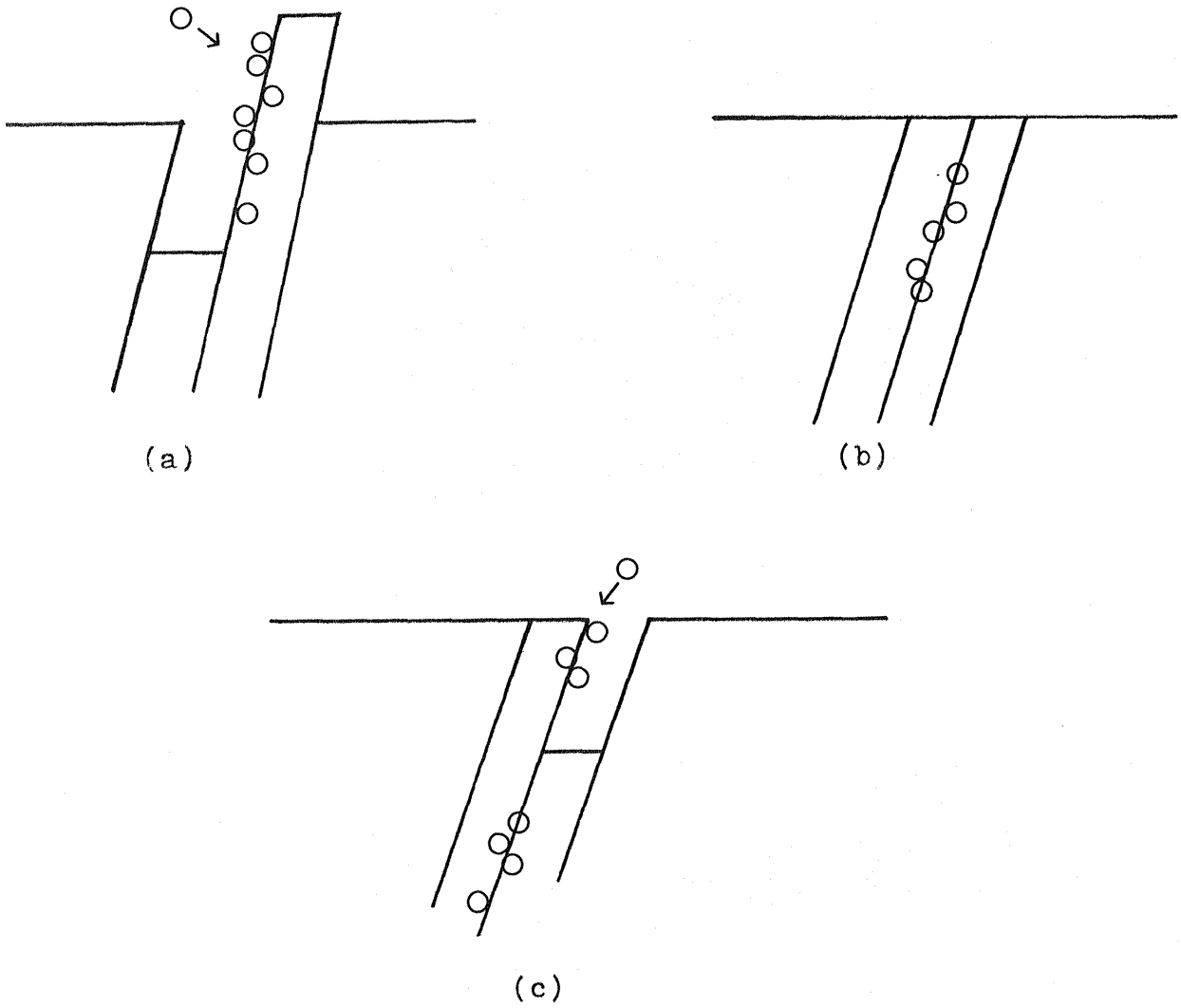

Figure 76 Schematic of Fujita's model for Slip assisted oxygen diffusion. A) is the tension going part of the cycle. Oxygen atoms form a surface layer on slip extrusion. B) is the compression going part of the cycle. Oxygen atoms are pulled into the grain. Further cycling(C) moves oxygen atoms deeper into the grain.

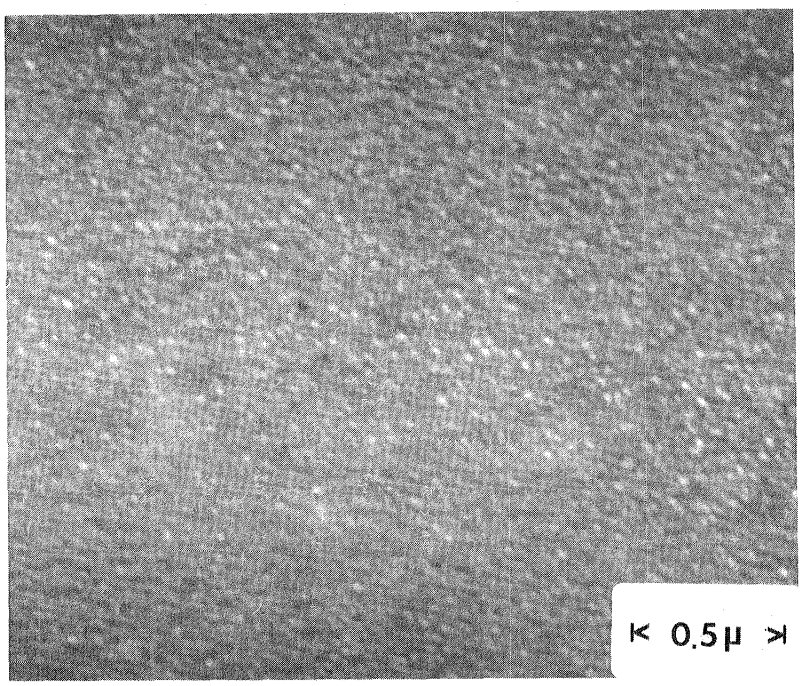

Figure 77 Coarse grained small γ' initial structure heat treated at 800 C for 1.25 hrs. to simulate 800 C testing times. γ' grew to ~100Å diameters compared to the 190Å for the tested specimen (Fig. 74a). g= {300}.

1. Report No.	2. Government Accession No.	3. Recipient's Catalog No.
NASA CR-165497		

4. Title and Subtitle	5. Report Date
MICROSTRUCTURAL EFFECTS ON THE ROOM AND ELEVATED TEMPERATURE LOW CYCLE FATIGUE BEHAVIOR OF WASPALOY	May 1982
	6. Performing Organization Code
7. Author(s)	8. Performing Organization Report No.
Bradley A. Lerch	None
	10. Work Unit No.
9. Performing Organization Name and Address	
University of Cincinnati Dept. of Metallurgical Engineering Cincinnati, Ohio	11. Contract or Grant No. NSG 3-263
	13. Type of Report and Period Covered
12. Sponsoring Agency Name and Address	Contractor Report
National Aeronautics and Space Administration Washington, D. C. 20546	14. Sponsoring Agency Code 505-33-22

15. Supplementary Notes

Final report. Project Manager, Robert Oldrieve, Structures and Mechanical Technologies Division, NASA Lewis Research Center, Cleveland, Ohio 44135. Report was submitted as a thesis in partial fulfillment of the requirements for the degree Master of Science to the University of Cincinnati, Cincinnati, Ohio.

16. Abstract

The fatigue properties of Waspaloy at both room and elevated temperatures were studied. Two microstructures were employed. One containing coarse grains and small γ' and the other fine grains and large γ'. Damage mechanisms were examined and related to the mechanical properties. Solid longitudinal specimens were tested in air at a frequency of 0.33 or 0.50Hz. Cycles were fully reversed (i.e. $A=\infty$, stress and strain) and a constant longitudinal plastic strain range was maintained. Elevated temperatures were achieved by an RF induction heater. The coarse grained small γ' specimens exhibited planar slip on $\{111\}$ planes and precipitate shearing at all temperatures. This structure caused the stress response to rise to a maximum and then decrease to failure. Cracks initiated by a Stage I mechanism and propagated by a striation forming mechanism. At 700 and 800°C, cleavage and intergranular cracking were observed. Testing at 500, 700 and 800°C caused precipitation of grain boundary carbides. At 700°C, carbides were also observed to precipitate on slip bands. The fine grained large γ' specimens exhibited planar slip on $\{111\}$ planes. Dislocations looped the large γ' precipitates. This structure led to stress saturation and propagation was observed. Increasing test temperatures resulted in increasing specimen oxidation for both heat treatments. Slip band and grain boundary oxidation were observed. At 800°C, oxidized grain boundaries were cracked by intersecting slip bands which resulted in intergranular failure. The fine grained specimens had crack initiation later in the fatigue life but, with more rapid crack propagation, the total fatigue life for equivalent LCF test conditions were the same for both fine and coarse grain specimens.

17. Key Words (Suggested by Author(s))	18. Distribution Statement
Fatigue Metallurgy Superalloys Microstructure	Unclassified - unlimited STAR Category 39

19. Security Classif. (of this report)	20. Security Classif. (of this page)	21. No. of Pages	22. Price*
Unclassified	Unclassified	193	

* For sale by the National Technical Information Service, Springfield, Virginia 22161

☆USGPO: 1982 — 559-091/3233

End of Document